Special Topic

Alpha particle physics experiments in the Tokamak Fusion Test Reactor

S.J. Zweben, R.V. Budny, D.S. Darrow, S.S. Medley, R. Nazikian,
B.C. Stratton, E.J. Synakowski, G. Taylor for the TFTR Group

Princeton Plasma Physics Laboratory,
Princeton University, Princeton,
New Jersey, United States of America

Abstract. Alpha particle physics experiments were done on TFTR during its DT run from 1993 to 1997. These experiments utilized several new alpha particle diagnostics and hundreds of DT discharges to characterize the alpha particle confinement and wave–particle interactions. In general, the results from the alpha particle diagnostics agreed with the classical single particle confinement model in MHD quiescent discharges. The alpha loss due to toroidal field ripple was identified in some cases, and the low radial diffusivity inferred for high energy alphas was consistent with orbit averaging over small scale turbulence. Finally, the observed alpha particle interactions with sawteeth, toroidal Alfvén eigenmodes and ICRF waves were approximately consistent with theoretical modelling. What was learned is reviewed and what remains to be understood is identified.

Contents: 1. Introduction: 1.1. Motivation for alpha particle experiments on TFTR, 1.2. Alpha particle confinement models, 1.3. Alpha particle diagnostics for TFTR, 1.4. Overview of TFTR DT experiments. **2. Alpha loss measurements:** 2.1. Scintillator detectors, 2.2. Alpha collector probe, 2.3. Summary of alpha loss results, 2.4. Theoretical interpretations, 2.5. Directions of future research. **3. Pellet charge exchange diagnostic measurements:** 3.1. PCX measurement technique and instrumentation, 3.2. PCX measurements in MHD quiescent plasmas, 3.3. PCX measurements in the presence of MHD activity, 3.4. Summary of PCX measurements and directions for future work. **4. Alpha charge exchange recombination spectroscopy:** 4.1. α-CHERS measurement technique and instrumentation, 4.2. Confined alpha slowing down and transport, 4.3. Observation of non-thermal alpha redistribution due to sawteeth, 4.4. Summary and directions for future work. **5. Alpha particle heating and alpha ash buildup:** 5.1. Alpha particle heating, 5.2. Alpha ash buildup and transport. **6. Alpha particle driven toroidal Alfvén eigenmodes in TFTR:** 6.1. Initial attempts to study alpha driven instabilities, 6.2. Theoretical developments concerning TAE instability, 6.3. Experimental observations of alpha driven TAEs in TFTR DT plasmas, 6.4. Radial structure of alpha particle driven TAEs. **7. RF–alpha interactions:** 7.1. Historical background and previous work, 7.2. ICRF induced loss of alpha particles, 7.3. ICE emission from DT plasmas, 7.4. Search for alpha channelling in DT plasmas, 7.5. Open issues and future work needed. **8. Summary and conclusions:** 8.1. Alpha particle behaviour in MHD quiescent discharges, 8.2. Effects of MHD and RF waves on alpha behaviour, 8.3. Alpha particle driven instabilities, 8.4. Alpha particle diagnostics, 8.5. Alpha particle modelling, 8.6. Implications for future experiments. **Acknowledgements. References.**

1. Introduction

The DT experiments on TFTR were the first opportunity to observe the behaviour of a substantial population of alpha particles in a tokamak. A large number of alpha particle measurements and physics experiments were performed during the DT run from 1993 to 1997, based on many years of diagnostic development and hundreds of DT discharges.

This special topic focuses specifically on the physics of the high energy (superthermal) alpha particle population created in these TFTR DT experiments. A prior review can be consulted on the behaviour of other types of fast ions in tokamak experiments [1], and an extensive bibliography of reports and papers on alpha particle physics and fusion product measurements has also been compiled recently [2].

Section 1 is an overview which describes the motivations and background to these experiments. Subsections in Section 1 review the basic physics of the alpha confinement models, give a brief summary of the alpha diagnostics considered and used, and summarize the general experimental conditions obtained during the TFTR DT run.

Sections 2 to 4 give detailed discussions of the three main alpha diagnostics used in TFTR along with their principal results; namely, the lost alpha scintillators (Section 2), the pellet charge exchange (Section 3) and the α-CHERS measurements (Section 4). The results are presented in the context of the alpha diagnostic capabilities and limitations, which strongly determined the available data in each case.

Sections 5 to 7 discuss alpha physics issues which were somewhat less dependent upon direct measurements of the fast alphas. Section 5 discusses the alpha heating and ash buildup experiments, Section 6 discusses the experiments on alpha driven toroidal Alfvén eigenmodes (TAEs) and Section 7 discusses the RF–alpha-particle interaction experiments.

Finally, Section 8 gives a summary of all these results organized according to physics topic, for example alpha confinement with and without MHD. There are also subsections on alpha diagnostic and modelling needs and implications for future DT experiments.

1.1. Motivation for alpha particle experiments on TFTR

The obvious motivation for the alpha particle experiments on TFTR was to make an initial assessment of the prospects for sustained alpha particle heating of an ignited or burning tokamak plasma. Ignition in a DT tokamak requires that a substantial fraction of the 3.5 MeV alpha particles created in the fusion reaction

$$D + T \rightarrow n\,(14.1\text{ MeV}) + \alpha\,(3.5\text{ MeV}) \tag{1}$$
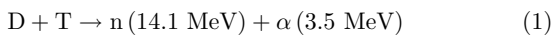
should remain confined sufficiently long to thermalize within the plasma. Given the classical thermalization rate due to Coulomb collisions, this normally requires at least several hundred milliseconds in a reactor relevant tokamak, which corresponds to a large number of alpha particle transits around the machine.

The main goal of the TFTR alpha experiments was therefore to determine whether these

Table 1. Alpha particle parameters in TFTR, JET and ITER

Parameter	TFTR	JET [191]	ITER [28]
P_{fus} (MW)	10.6	16.1	1500
$P_\alpha(0)$ (MW/m^3)	0.3	0.1	0.3
τ_α (s)	0.4	0.7	1.0
ρ_α/a	0.05	0.07	0.015
$n_\alpha(0)/n_e(0)$ (%)	0.3	0.4	0.3
$\beta_\alpha(0)$ (%)	0.3	0.62	0.7
$\langle\beta_\alpha\rangle$	0.04	0.11	0.2
$R\nabla\beta_\alpha$	0.02	0.03	0.06
$V_\alpha/V_A(0)$	1.7	1.6	1.9

superthermal alphas were confined as expected, and also whether their presence had any new effect on the plasma, for example, by the creation of an alpha driven instability. TFTR reached only a maximum of Q (fusion power output/auxiliary power input) ≈ 0.25, so the direct effect of alpha heating was small, as discussed in Section 5.

The initial motivations for the alpha particle experiments in TFTR were described before the start of the DT run [3, 4]. A result of those calculations was that some of the alpha particle parameters expected in TFTR were similar to those expected in ignited plasmas, for example ITER. For example, the central alpha heating power in TFTR is similar to that for ITER (≈ 0.3 MW/m^3), and the central alpha beta value is about a factor of 2 lower in TFTR than ITER (0.3% versus 0.7%). A comparison of these and other alpha parameters in the TFTR DT experiments with those in JET and those expected for ITER is shown in Table 1.

The central alpha parameters in TFTR (and JET) are fairly near to those expected for ITER because the alpha particle density in DT plasmas depends only on the local plasma parameters, and not directly on the fusion power gain Q (which depends on the plasma energy confinement time). The local alpha particle pressure can be estimated as follows [4]: for thermonuclear DT plasmas with $T_i \approx T_e \approx 10-30$ keV and $Z = 1$, the local alpha production rate is $S_\alpha \propto n^2 T_i^2$ (for 5 keV $< T_i <$ 20 keV), and the local alpha thermalization time is $\tau_\alpha \propto T_e^{1.5}/n$, so the local alpha density is $n_\alpha = S_\alpha \tau_\alpha \propto n T_i^2 T_e^{1.5}$. Since the average alpha particle energy in a classical slowing down spectrum is $\langle E_\alpha \rangle \approx 1.3$ MeV (nearly independent of plasma parameters), the relative

alpha beta value with respect to the plasma beta is thus

$$\beta_\alpha/\beta \propto T^{5/2}. \tag{2}$$

Since the plasma temperatures are similar in TFTR ($T_i \approx 30$ keV, $T_e \approx 10$ keV) and, for example, ITER ($T_i \approx T_e \approx 20$ keV), the alpha beta value relative to the plasma beta turns out to be fairly similar in the centre of both machines, i.e. $\beta_\alpha/\beta \approx 10\%$. Note that the calculations of the TFTR and JET alpha parameters in Table 1 take into account the exact alpha source dependence on temperature (including nonthermal sources), the details of the collisional alpha thermalization processes and the first orbit losses.

Thus one motivation for the TFTR alpha particle experiments was to examine the 'collective' particle behaviour of a reactor relevant population of alpha particles. This same motivation had previously led to a series of fast ion experiments in D plasmas which aimed to simulate the behaviour of alpha particles in DT plasmas [1]. These D experiments revealed a strong fast ion driven instability called the TAE, which occurred above a critical fast ion beta when the fast ion speed was comparable to or larger than the Alfvén speed. Since the ratio of the alpha speed to the Alfvén speed was above 1 for both TFTR and reactor level tokamaks (Table 1), a specific focus of the TFTR alpha experiments was to look for the alpha driven TAE (Section 6).

A less compelling, but still important, motivation for the TFTR alpha experiments was to check the 'single particle' confinement and loss of alphas. Such experiments do not necessarily require a large population of alphas since these single particle effects are due to the interactions with the intrinsic magnetic fields or waves in the background plasma, for example toroidal field ripple loss, ICRF waves or plasma driven MHD activity. In fact, a substantial body of information had already been obtained about single particle confinement of alpha-like energetic ions, for example from the 'burnup' of the 1 MeV tritons created in DD reactions [1, 5]. However, the ≈ 100 times larger alpha populations in DT plasmas allowed a direct measurement of the local alpha particle density and local alpha heating inside the plasma, which was valuable for testing the single particle confinement models (Sections 3–5).

1.2. Alpha particle confinement models

Alpha particle orbits in a tokamak resemble thermal ion orbits, except that the shifts of their drift surfaces from magnetic flux surfaces are about 10 times larger than those for thermal ions due to their ≈ 100 times higher energy at birth. This causes some of the alphas to be lost to the chamber wall on their first poloidal transit of the tokamak. This 'first orbit loss' was understood and calculated well before the construction of TFTR [6, 7], and observed using DD fusion products in lower current tokamaks [1].

Examples of 3.5 MeV alpha particle orbits calculated using the exact equations of motion for a typical TFTR case are shown in Fig. 1(a) [8]. These orbits are all started at the same point, but each has a different pitch angle with respect to the toroidal magnetic field B. The finite gyroradius of $\rho_\alpha \approx 5$ cm for birth energy alphas can be seen for these orbits for a typical toroidal field of $B = 5$ T. At low pitch angles the alpha orbits are passing and confined on their first orbit, while at high pitch angles the alpha orbits are trapped but still confined on their first orbit. However, in a narrow range of pitch angles near the passing–trapped boundary the alphas are trapped and lost on their first orbit. At $I = 2.5$ MA in this case the range of pitch angles for this 'first orbit loss' is relatively small, but at lower current the first orbit loss region increases due to the increase in banana width. A map of the first orbit loss region for an $I = 1.4$ MA case is shown in Fig. 1(b), where the birth major radius (along the outer midplane) and pitch angle are varied systematically.

Monte Carlo calculations were done before the start of TFTR to estimate the first orbit loss fraction as a function of plasma current, assuming an alpha source and plasma current profile [6]. Those results showed that this global loss fraction is just a few per cent at $I = 2.5$ MA, but could be substantial ($\approx 30\%$) at a lower plasma current of $I = 1$ MA, since then the alpha banana width is comparable to the plasma minor radius and most of the trapped alphas are lost to the wall. Similar results were obtained from calculations based on actual TFTR plasma conditions, as summarized in Table 2. In the simplest alpha confinement model described above, all the alphas which were confined after their first orbit would remain confined forever, at least in the absence of collisions or deviations from axisymmetry in the magnetic structure. However, it is obvious that classical Coulomb collisions will gradually thermalize the alphas as they heat the plasma [1]. The effect of the collisions with electrons is to produce a friction which results in a velocity e-folding time of

$$\tau_{\alpha e}(\text{s}) \approx 0.4\,(T_e/10\text{ keV})^{3/2}/(n_e/10^{20}\text{ m}^{-3}). \tag{3}$$
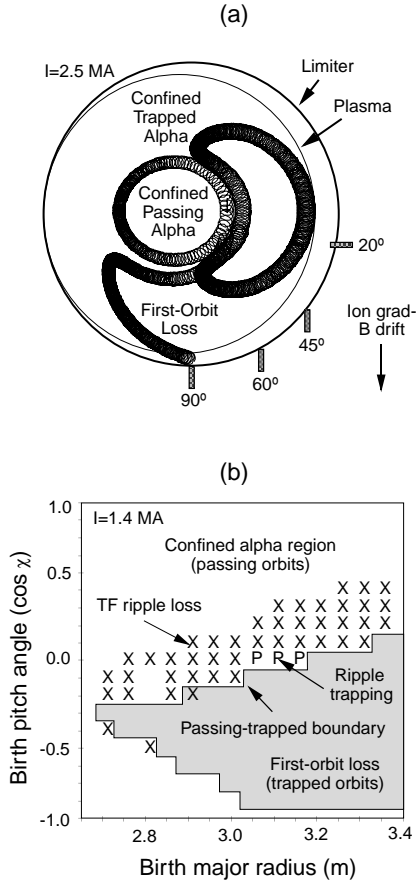
(a)

(b)

Figure 1. Projections onto a poloidal plane of typical 3.5 MeV alpha particle orbits in TFTR are shown for a standard plasma with $I = 2.5$ MA, $B = 5$ T and $R = 2.52$ m. Each of these orbits starts from the same minor radius ($r/a \approx 0.3$), but has a different pitch angle with respect to the toroidal field. The alpha gyroradius is ≈5 cm (shown), and the direction of the ion ∇B drift is downward. Panel (a) shows the four alpha loss scintillator detector locations and panel (b) shows a map of the first orbit loss region for an $I = 1.4$ MA, $R = 2.52$ m case, also showing the TF ripple loss region.

This e-folding time on electrons is typically $\tau_{\alpha e} \approx 0.4$ s at the plasma centre of high performance TFTR shots in which $T_e(0) \approx 10$ keV and $n_e(0) \approx 10^{20}$ m^{-3}, corresponding to a few hundred thousand toroidal transits of the machine. The time required for alphas to reach thermal energy, including ion drag, is [1]:

$$\tau_\alpha = (\tau_{\alpha 0}/3) \ln\left[1 + (E_{\alpha 0}/E_{crit})^{3/2}\right] \tag{4}$$

where $E_{\alpha 0}$ is the alpha birth energy and E_{crit} is the alpha energy below which ion drag dominates the

Table 2. Classical alpha confinement calculations for TFTR

	$I = 1.0$ MA	$I = 2.0$ MA
First orbit loss [8]	≈10–15%	≈3–5%
TF ripple loss [15]	≈5–10%	≈10–20%

thermalization process (typically $E_{crit} \approx 35T_e$ for alphas). For an idealized plasma without alpha loss, these collisions produce the well known slowing down distribution [1]

$$f_\alpha(V_\alpha) = S_\alpha \tau_\alpha (V_\alpha^3 + V_{crit}^3)^{-1} \tag{5}$$

where $E_\alpha = \frac{1}{2} m_\alpha V_\alpha^2$ and $E_{crit} = \frac{1}{2} m_\alpha V_{crit}^2$. The average alpha energy for this ideal steady-state distribution function is $\langle E_\alpha \rangle \approx 1.3$ MeV, and is roughly independent of plasma temperature near 10 keV. The effect of collisional thermalization on alpha orbits is mainly to move their drift surfaces closer to the magnetic flux surfaces, which tends to improve their confinement and does not cause much additional alpha loss. However, collisions also cause pitch angle scattering of the alphas, which changes their magnetic moment and can cause some additional alpha loss, mainly by converting passing alphas to trapped alphas whose orbits intersect the wall. The extent of this effect depends upon the ratio of the pitch angle scattering time to the slowing down time, which for high energy alphas is [9]:

$$\tau_{\alpha\perp}/\tau_{\alpha e} \approx 1/[50Z_{eff}(T_e/E_\alpha)^{3/2}]. \tag{6}$$

This ratio is typically large for alphas in TFTR, for example $\tau_{\alpha\perp}/\tau_{\alpha e} \approx 50$ at $T_e = 10$ keV, so to a first approximation alphas thermalize without significant pitch angle scattering or collisional loss, except for alpha orbits very near a loss boundary in velocity space. Numerical and analytical calculations for alphas in the axisymmetric TFTR case (without TF ripple) showed that alpha loss due to collisions in a typical TFTR case ($I = 1.6$ MA) was only ≈1%, which was mainly due to marginally passing alphas scattered across the passing–trapped boundary and out to the wall [10, 11]. This loss rate is small compared with first orbit and toroidal field (TF) ripple induced loss (Table 2).

The remaining causes of alpha deconfinement are generally related to various non-axisymmetries in the magnetic field structure, such as TF ripple or internal MHD activity. These effects are mainly due to

random spatial movements of the alpha particle guiding centre orbits, and not to changes in the magnetic moment, since these perturbation frequencies are generally much smaller than the ion cyclotron frequency. Even very small radial excursions can cause a significant radial diffusion; for example, a random radial step size of only 0.1 cm per toroidal transit, given a toroidal transit time of $\approx 2\pi R / V_\alpha \approx 1$ μs for 3.5 MeV alphas, would cause a radial diffusion coefficient of $D \approx 1$ m^2/s. Alpha diffusion at this rate would imply a significant loss of alpha energy before thermalization in TFTR (which was actually not observed).

The most predictable type of deviation from magnetic axisymmetry is due to the TF ripple associated with the finite number of TF coils. In TFTR with 20 TF coils, this produces a maximum TF ripple (i.e. peak to average $\delta B_{tor}/B_{tor}$ along a field line) of $\delta \approx 2\%$ at the outer limiter, but more typically $\delta \approx 0.1\%$ inside the plasma. This ripple can cause the radial location of the banana tips of trapped alpha orbits to become decorrelated above a TF ripple strength [12] of

$$\delta_{GWB} \approx (\varepsilon/N\pi q)^{3/2}(1/\rho q') \qquad (7)$$

where δ_{GWB} is the Goldston–White–Boozer (GWB) stochastic ripple loss threshold. Here $\varepsilon = r/R$ is the location of the alpha banana tip, N is the number of TF coils, ρ is the gyroradius of the orbit, and q and q' ($= dq/dr$) depend on the magnetic $q(r)$ profile at the banana tip. The poloidal projection of an alpha particle guiding centre orbit under the influence of stochastic TF ripple diffusion in TFTR is shown in Fig. 2, and a typical ripple loss region is shown in Fig. 1(b).

Although this stochastic criterion and its recent generalizations [13] describe the basic physics of TF ripple induced alpha transport, numerical calculations were necessary to evaluate the effect of TF ripple on alpha confinement in the TFTR experiments. Extensive Monte Carlo guiding centre code simulations have been done to evaluate the collisional ripple loss of alphas in TFTR [14, 15] using either generalizations of the GWB criterion or the ORBIT guiding centre code [16]. As summarized in Table 2, the calculated alpha ripple loss was typically ≈ 10–20% for normal plasma conditions on TFTR ($R = 2.5$ m, $I = 2.0$ MA), about half of which was 'collisionless' and half due to pitch angle scattering during alpha thermalization [14].

The alpha ripple loss tends to be larger for plasmas of large major radius ($R = 2.6$ m) which extend
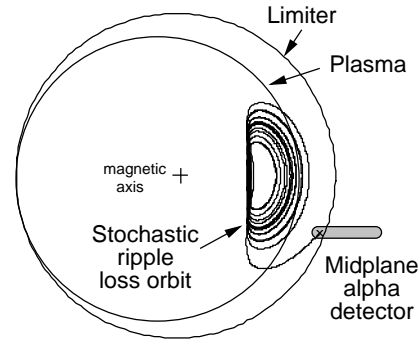

Figure 2. Projections onto a poloidal plane of the guiding centre of a typical 3.5 MeV alpha particle orbit undergoing collisionless stochastic TF ripple diffusion are shown for a TFTR plasma with $I = 1.4$ MA and $R = 2.52$ m. The banana tip of this orbit started in a high TF ripple region at large major radius and diffused vertically until the particle hit the limiter just below the outer midplane.

into the high ripple region, and particularly large for plasmas with high $q(0)$ for which the stochastic threshold is low [17]. At plasma currents above about $I \geq 1.6$ MA the calculated TF ripple loss is larger than the first orbit loss, and so is the dominant 'classical' alpha loss mechanism. At low plasma currents $I \leq 1$ MA most of the trapped alphas are lost on their first orbits, so the TF ripple loss of alphas is relatively small.

Most of the alpha particle physics above has been incorporated into the TRANSP transport code, which is the standard analysis code for TFTR experiments. Alpha particle density profiles, energy spectra, heating power, loss fractions, etc. are calculated versus time for most TFTR DT discharges using TRANSP [18, 19]. The alpha particle parameters for the highest fusion power discharge obtained on TFTR (10.7 MW) are shown in Table 1 (see also Table 5), and TRANSP results for the alpha particle parameters for this discharge are shown in Figs 3 and 4.

The TRANSP calculated central alpha heating rate as shown in Fig. 3(a) was up to $P_\alpha(0) \approx 0.3$ MW/m^3, peaking ≈ 0.2 s after the peak in fusion power due to the finite alpha thermalization. The maximum global alpha heating power was ≈ 1.2 MW at 3.7 s, i.e. about 3% of the global neutral beam heating power at that time. This alpha heating power was less than the ≈ 2 MW expected from a fifth of the total fusion power, since the calculated discharge was
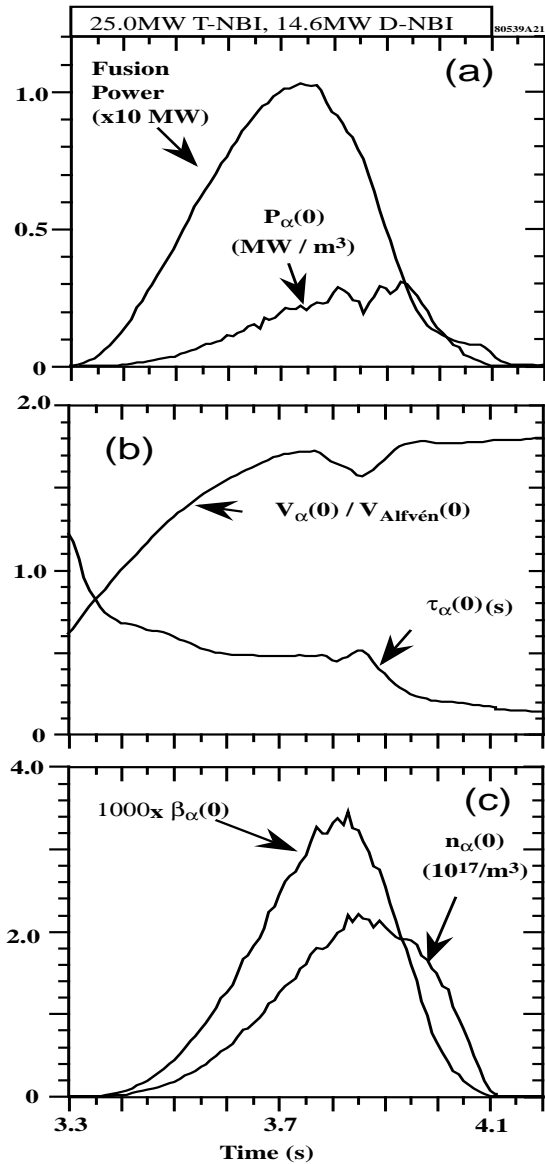
Figure 3. Time dependences of the alpha particle parameters calculated by TRANSP for the highest fusion power discharge in TFTR (discharge 80539). Panel (a) shows the total fusion power and the central alpha heating rate, panel (b) shows the central alpha birth speed normalized to the central Alfvén speed and the alpha particle thermalization time, and panel (c) shows the central alpha density and β. There was an MHD event at 3.8 s which caused a large influx of impurities, which in turn caused the fusion power and the central temperature to drop.
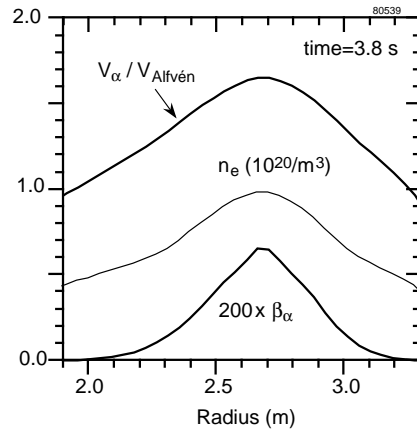

Figure 4. Radial dependences of the alpha particle β and the alpha birth speed relative to the Alfvén speed, as calculated by TRANSP at 3.8 s for the highest fusion power discharge in TFTR (No. 80539). The alpha pressure profile is more peaked than the electron density profile, and the alphas are super-Alfvénic over essentially all of their density profile.

not in equilibrium at this time and since the alpha loss fraction was 12.5% (10% of which was TF ripple loss).

The alpha particle thermalization time was $\tau_\alpha \approx 0.5$ s, as shown in Fig. 3(b), at least until the minor disruption just after the neutron peak (which caused a density increase and a reduction in the alpha thermalization time). The central alpha birth speed V_α was generally $\overset{\sim}{>}1.5$ times the central Alfvén speed V_A. The central alpha density n_α was a small fraction of the central electron density, as shown in Fig. 3(c), while the central alpha beta $\beta_\alpha(0)$ was over 0.3%, i.e. about 10% of the total central beta. The central alpha heating rate is somewhat delayed with respect to the central alpha density due to the decrease in alpha thermalization rate just after the minor disruption.

The TRANSP calculated radial profile of alpha beta is shown in Fig. 4 for the same discharge as in Fig. 3. The alpha beta profile was more peaked than the electron density profile, due to the highly peaked neutron source rate. The alpha speed is larger than the Alfvén speed over the region of the maximum gradient of the alpha pressure inside $r/a \approx 0.3$. The alpha distribution functions in pitch angle and energy were similar to those described previously for a 7.5 MW DT discharge [19].
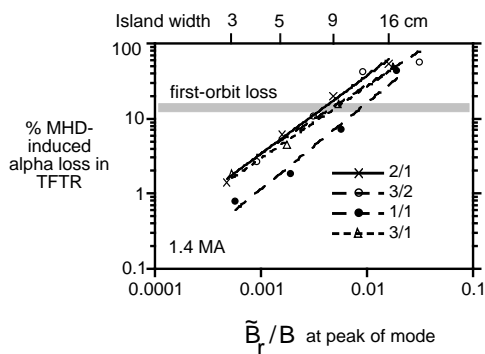
Figure 5. Calculated global alpha particle loss fraction versus the magnitude of the assumed stationary helical perturbations for an $I = 1.4$ MA, $R = 2.52$ m plasma in TFTR, as calculated by the ORBIT Monte Carlo code. For example, the MHD induced alpha loss is smaller than the calculated first orbit loss for $m(\text{poloidal})/n(\text{toroidal}) = 2/1$ magnetic island sizes below about 10 cm, which is normally the largest size of low-n MHD modes in TFTR. The island width is shown at the top for the $m/n = 2/1$ mode only.

Deconfinement of alpha particles can also be caused by MHD activity of various types, such as coherent low m/n (poloidal/toroidal mode number) tearing modes, high-n ballooning modes, sawteeth, disruptions or TAEs. Each of these involves some form of non-axisymmetric magnetic perturbation for which there is a threshold for stochastic diffusion analogous to that for TF ripple (Eq. (7)). However, for helical low-n modes this threshold depends inversely on the toroidal mode number [20], so for low-n, low frequency magnetic perturbations such as tearing modes ($n \approx 1$–3, $f \approx 1$ kHz), the calculated alpha loss due to stochastic diffusion is usually relatively small. An example of the calculated alpha losses for various stationary low-n helical magnetic perturbations in TFTR is shown in Fig. 5, based on simulations with the Monte Carlo ORBIT code (Section 2.1.4). The resulting global alpha loss for these cases is smaller than the first orbit loss except for very large island widths of ≥ 10 cm.

However, for MHD reconnection events such as sawteeth and disruptions, the magnetic perturbations are much more complex in space and transient in time (≈ 10 μs), so the alpha transport needs to be calculated using specialized and (generally) simplified models. The most important issue is probably the redistribution of alphas during sawtooth events, which could cause a broadening of the alpha heating

profile and an increase in TF ripple loss of trapped alphas. The simplest models assume a radial 'mixing' of alphas analogous to that of the Kadomtsev model for thermal plasma, while more detailed models also calculate the effect of the time dependent magnetic and induced electric fields on the alpha orbits. There is a discussion of these models as applied to the TFTR data in Sections 3 and 4.

For higher frequency MHD perturbations such as high-n kinetic ballooning models (KBMs) or TAEs ($f \approx 100$–300 kHz), there is the additional effect of transit resonance between the waves and the alpha particles. This can cause a change in the energy of the alpha particles and/or a convective radial transport, at least for some part of the alpha distribution. For example, TAEs are driven by the free energy in the alpha particle distribution through such a wave–particle transit or bounce resonance. Many models for this type of interaction have been investigated for fast ions in tokamaks [1], but only a few examples of alpha loss due to these high frequency MHD events in TFTR has been observed (Section 2.1.4).

The effect of small scale, high frequency plasma turbulence on alpha confinement has been calculated in several papers [20–23]. The main theoretical issue is to evaluate the effect of 'orbit averaging'; i.e. how alpha diffusion is affected by perturbations with size scales smaller than the alpha gyroradius and/or banana width. In general, the alpha transport is very much reduced when the radial size scale of the perturbation is smaller than the alpha gyroradius, for both electrostatic and magnetic fluctuations. This occurs in TFTR since the typical alpha gyroradius is 5 cm while the typical electrostatic turbulence radial size scale is most likely ≈ 1 cm [24]. This orbit averaging effect explains (at least qualitatively) why the alpha diffusion rate is ≤ 0.1 m^2/s, i.e. much smaller than thermal ion diffusion rate of ≈ 1 m^2/s [25].

Finally, there can be a coupling between the alpha particles and the RF waves in the ion cyclotron range of frequencies (ICRF). The fundamental interaction in this case is the alpha cyclotron resonance, which usually occurs in a narrow range of minor radii for alphas of given energy. This interaction can increase the energy or magnetic moment of alphas, causing some of them to be lost across the passing–trapped boundary. The alphas can also be cooled, at least in principle, by selective application of ICRF or mode converted ion Bernstein waves in combination with another wave [26]. Alphas can also emit ion cyclotron radiation, although with a negligible energy loss. These effects are discussed in Section 7.

Details of the TFTR experimental results on alpha confinement are described in Sections 2–5. Further general information on alpha confinement models can be obtained from other reviews [1, 3, 7, 27–30]. A summary of the TFTR results is given in Section 8, including a discussion of the various alpha modelling codes in Section 8.5.

1.3. Alpha particle diagnostics for TFTR

Energetic alpha particles are difficult to measure directly since their density inside the plasma is very small, $n_\alpha/n_e < 1\%$ (Table 1) and they normally do not emit atomic or nuclear radiation. However, a variety of alpha particle diagnostics were investigated in the 1980s for use in the TFTR and JET DT experiments, and several of these were used successfully to measure alpha particles during the TFTR DT experiments.

The main elements of alpha particle diagnostic coverage in TFTR were measurements of the alpha birth rate and profile using 14 MeV neutron detectors, of the confined fast alpha particle density and energy spectrum using charge exchange, and of the alpha loss using scintillation detectors at the wall. In addition, the thermalized alpha density (i.e. alpha 'ash') was measured using charge exchange recombination spectroscopy, the alpha heating was detected using the standard electron temperature diagnostic, and the alpha ion cyclotron emission was detected with special magnetic loops near the wall.

Table 3 summarizes the main alpha diagnostics used in the TFTR DT experiments, and Fig. 6 illustrates schematically their spatial and energy coverage. The global neutron source rate, i.e. the alpha source rate, was measured using fission detectors to an absolute accuracy of about ±15% and a relative (shot to shot) accuracy of ±5%, and the neutron profile was measured using a multichannel collimator array [31]. These neutron measurements were generally in good agreement with the calculated neutron profiles from TRANSP (generally within ±20%), which were based on the measured temperature and density profiles and a Monte Carlo calculation of the spatial and energy distribution of the thermalizing fast ions injected by the neutral beams.

The alpha loss was measured using a poloidal array of four scintillator detectors located at the bottom of the vessel in the ion ∇B drift direction. The confined alphas at the low energy end of the spectrum ($E \leq 0.7$ MeV) were measured using an α-CHERS diagnostic based on the visible light
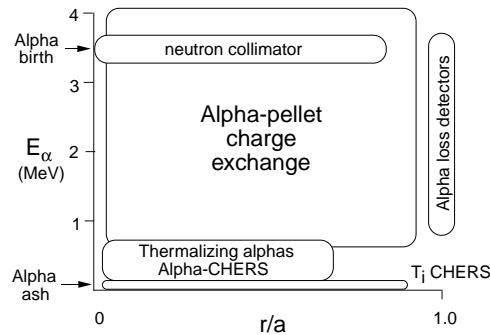

Figure 6. Schematic illustration of the alpha diagnostic coverage in TFTR. The alpha source profile is evaluated from the 14 MeV neutron profile, the confined alphas are measured by charge exchange diagnostics and the alpha loss is measured by scintillator detectors at the wall. Not all measurements can be made at the same time, and each diagnostic covers a different range of pitch angles.

emission from alphas having a single charge exchange with the neutral beam ions. The confined alphas at the high energy end of the spectrum were measured using a pellet charge exchange (PCX) diagnostic in which the alphas were doubly charged exchanged in an injected pellet cloud and detected outside the plasma.

It is important to note that each of these alpha diagnostics has a different range of coverage in pitch angle, which is not shown explicitly in Fig. 6. Specifically, the lost alpha detectors measure over a pitch angle typically 45–85° with respect to the co-current going toroidal direction, the PCX measures only a narrow range of pitch angle nearly perpendicular to the toroidal field and the α-CHERS measures mainly co-current passing alphas. Therefore, none of these alpha diagnostics measures the whole of the alpha distribution function in either energy or pitch angle. Details of these three diagnostics are covered in Sections 2–4.

Several other alpha particle diagnostics were tested on TFTR before and/or during the DT run, as summarized in Table 4. The most successful of these was the alpha collector probe, which measured alphas deposited into thin aluminium foils inside a removable probe at the vessel bottom, as described in Section 2.2. Alphas were also detected using their ion cyclotron emission, although the interpretation of these signals was difficult, as described in Section 7.3. A diamond detector was installed which was able to measure charge exchange loss of minority heated hydrogen tail ions, but not alphas in DT

Table 3. Main alpha particle diagnostics on TFTR

Measurement	General features	TFTR specifications
Alpha source rate [31] (14 MeV neutrons)	• Fission detectors for global neutron rate	• Global rate within ±15%
	• 10 channel ZnS detectors for neutron profiles	• Spatial resolution ≈10 cm, frequency response 20 kHz for neutron fluctuations
Alpha loss scintillators [55]	• P46 phosphor, optical coupling of images	• Four detectors, 20, 45, 60 and 90° below outer midplane
	• Pitch/energy resolution with 0.02 cm^2 apertures	• ≈1–4 MeV energy range
	• Only the 20° detector radially movable	• ≈100 kHz bandwidth for total loss, 60 Hz for images
Fast confined alphas (pellet charge exchange) [90]	• Double charge exchange on Li or B pellet cloud	• ≈0.5–4 MeV energy range
	• ≈10 cm spatial resolution	• Pitch angle perpendicular to toroidal field
	• 1–2 pellets/shot, normally ≈0.1–0.3 s after NBI ends	
Slow confined alphas (α-CHERS) [97]	• Single charge exchange on D NBI atoms	• ≤0.7 MeV energy range
	• Measures Doppler shifted He^+ light (468.6 nm)	• Five spatial channels within $r/a \approx 0.05$–0.6
		• ≈0.1 s time resolution
Alpha ash (CHERS) [110]	• Single charge exchange on D or T NBI, measures thermal He^+ (468.6 nm)	• ≤50 keV energy range
		• 17 spatial channels, 50 ms time resolution

plasmas [32]. The visible helium light emitted by doubly charge exchanged alphas inside the pellet cloud was measured, but the signal to background level was too low to detect alphas [33]. A system to detect fast ions via the scattering of microwaves was installed, but significant hardware and modelling difficulties were encountered [34]. A detector was installed for measuring nuclear gamma emission from resonant nuclear reactions [35], but the signal to background ratio was too low to observe alphas in DT.

Other ideas for alpha detection were developed or evaluated to a lesser extent on TFTR, as also listed in Table 4. An alpha loss detector based on a Faraday cup design was shown to have an acceptably low response to neutron/gamma radiation backgrounds just outside the vessel during DT discharges [36]. A gel based 'bubble chamber' for detecting alphas using the high energy neutrons created by 'knock-on' collisions between alphas and fuel ions [37] was exposed to DT discharges, but an unexpected below threshold response in the detectors did not allow clear observation of the knock-on neutrons. The information gained in these experiments indicates that redesigned detectors should allow knock-on tail measurements. An IRTV system to detect the alpha heating of the first wall limiters was designed for TFTR, similar to that used for beam ion loss

Table 4. Additional alpha diagnostics tested or evaluated on TFTR

	Advantages	Disadvantages
Alpha collector foils [74]	• Radiation resistant • Absolutely calibrated	• Needs ex vessel analysis • No intrinsic time resolution
Ion cyclotron emission [151]	• Simple magnetic loops	• Signals difficult to interpret
Diamond detectors [32]	• Good energy resolution	• Potential radiation damage
He^0 light emission [33]	• Potentially simpler than double charge exchange	• Requires impurity pellet to penetrate to region of interest
Microwave scattering [34]	• Potentially good spatial and energy resolution	• Needs high powered microwave source
Alpha nuclear reactions [35]	• Gamma radiation emitted from nuclei inside plasma	• Low signal/background
Faraday cup [36]	• Radiation resistant	• Small electrical signals
Alpha knock-on [37]	• Relatively simple detector for high energy neutrons	• Small signal in present experiments
Alpha heating of first wall [38]	• Large area coverage • Simplicity	• No pitch/energy resolution • Backgrounds from plasma
Foil neutralization [39]	• Possible removal of detector to outside of toroidal field	• Foil is fragile and can melt

in JT-60U [38], but was not implemented. Finally, a method for foil neutralization of alpha loss was developed [39], but never tried on TFTR.

Further information about other proposed alpha diagnostics can be found in various diagnostic reviews and conference proceedings [40–43]. References [42] and [43] contain papers and summaries from the two most recent IAEA Technical Committee Meetings on Alpha Particles in Fusion Research, which has been the main forum for international discussions of alpha particle physics since 1986.

1.4. Overview of TFTR DT experiments

There have been several reviews of the TFTR DT experiments [44–46] and machine operations [47, 48]. Only a very brief summary of the overall TFTR DT experimental environment is given here for orientation.

The first high powered DT discharges were carried out in December 1993, and the last were carried out in April 1997. There were a total of 300 DT discharges with a significant amount of alpha particle production, i.e. having at least one tritium neutral beam source. A total of $\approx$5 g of tritium was introduced into the TFTR vessel, and a total of $\approx$1.5 GJ of fusion power was produced. The maximum instantaneous DT fusion power was 10.7 MW (pulse 80539), and the maximum fusion energy yield per discharge was 7.6 MJ, or 2.7×10^{18} neutrons (pulse 104382).

The measured parameters for the DT discharge with the highest instantaneous fusion power are shown in Table 5. The results of the TRANSP analysis of the alpha particle parameters for this discharge were shown in Table 2, and the time and radial dependences of some of these alpha parameters were shown in Figs 3 and 4. The TRANSP analysis took into account the time dependence of the alpha source and thermalization process in computing the alpha densities, alpha beta values and alpha heating.

A list of the main experiments on alpha particle physics done during the DT run is given in Table 6. Several of these experiments were designed specifically to accommodate the needs of the alpha diagnostics, for example the α-CHERS diagnostic measured

Table 5.   TFTR plasma with highest alpha source rate (discharge 80539

Plasma current: $I = 2.7$ MA
Toroidal field: $B = 5.6$ T
Major radius: $R = 2.52$ m
Minor radius: $a = 0.87$ m
Peak DT neutron rate: $S_{DT} = 3.8 \times 10^{18}$ n/s
Peak fusion power: $P_{FUS} = 10.7$ MW
Neutral beam power: $P_{NBI} = 39.6$ MW
Stored energy: $W = 6.9$ MJ
Electron density: $n_e(0) = 1.0 \times 10^{20}$ m^{-3}
Electron temperature: $T_e(0) = 13$ keV
Ion temperature: $T_i(0) = 36$ keV
Confinement time: $\tau_E = 0.18$ s
$\langle Z_{eff} \rangle = 2.4$
$\beta_n = 1.8$ (Troyon normalized)

Table 6.   Main alpha particle experiments in TFTR

Section 2:
  Alpha particle loss versus plasma current [8]
  Search for collisional non-prompt alpha loss [59]
  Effects of $q(r)$ on Alpha Ripple Loss [63]

Section 3:
  Pellet charge exchange classical measurements [89]
  Pellet charge exchange sawtooth measurements [91]

Section 4:
  α-CHERS slowing down measurements [98]
  α-CHERS measurements with sawteeth [102]

Section 5:
  Alpha particle heating [109]
  Alpha particle ash buildup [110]

Section 6:
  Search for TAEs at lowered ion temperature
    and beta [129]
  Alpha particle effect on TAEs from ICRH
    minority tails [130]
  Search for beta induced Alfvén eigenmodes [131]
  Search for TAEs with high $q(0)$ [132]
  Core localized alpha driven TAEs [139]

Section 7:
  ICE emission measurements [151]
  ICRH–fusion product interactions [148]
  Fast ion channelling with IBW [173]

alphas only during D-only beams after the main DT heating pulse. Most of these experiments required several run days over several weeks or months. There was generally excellent reliability and reproducibility of the machine, diagnostics and heating systems during the three years of the DT run.

2.   Alpha loss measurements

The goal of the alpha loss measurements in TFTR was to check whether the alpha particle flux to the vessel wall was consistent with the classical model for alpha particle confinement (Section 1.2), and, if not, to understand the physical causes of any discrepancies. The ultimate goal of these experiments was to evaluate whether the alpha particle loss in a tokamak reactor would significantly reduce the alpha heating power or damage the first wall.

The alpha loss detectors in TFTR were based on earlier charged fusion product detectors developed by Strachan and his students. Solid state detectors were used to measure the escaping DD and D–^{3}He charged fusion products in PLT, PBX and TFTR [1, 49]. The loss of 3.7 MeV alphas from the D–^{3}He reaction was also measured in PLT by using a CR-39 plastic track detector [50]. However, semiconductor detectors could not be used for TFTR DT alpha detection due to their relatively low neutron damage threshold of $\approx 10^{12}$ neutron/cm^2, which was the expected neutron fluence per shot at $Q \approx 1$, and plastic CR-39 track detectors could not be used in TFTR due to their low melting point and the difficulty of removing the detectors for analysis. Since the maximum possible alpha energy loss was relatively small (≈ 2 MW over 0.5 s), the average wall temperature did not change significantly due to alpha heating, and no localized alpha heating or wall damage was observed during the DT run.

Sections 2.1 and 2.2 discuss results from the two lost alpha diagnostics used on TFTR, namely, the scintillator detectors and alpha collector probe, respectively. Section 2.3 summarizes the experimental conclusions from these results, Section 2.4 describes the status of the theoretical interpretation of these results and Section 2.5 reviews the needs and challenges for future alpha loss measurements in tokamaks.

2.1.   Scintillator detectors

The idea of using a thin scintillator (i.e. phosphor screen) to measure alpha loss in DT tokamaks

was proposed by several groups in the early 1980s [51–53]. The main advantages and practical limitations of these detectors for a DT tokamak diagnostic are discussed in Refs [54, 55].

2.1.1. Scintillator detector design on TFTR

The design of the scintillator detectors used for the TFTR DT experiments is shown schematically in Fig. 7. The detector element is a 1 in × 1 in scintillator screen inside a light-tight box located inside the TFTR vacuum vessel, but well outside the plasma edge. A combination of a pinhole and slit is used to disperse the alphas in pitch angle and gyroradius, thus allowing a measurement of their magnetic moment and energy distributions. The 2-D image of the visible light flux produced by the alpha impacts on the screen is transferred to cameras and phototubes in the shielded basement using quartz lenses and coherent fibre optic bundles.

The design illustrated in Fig. 7 could be used for both DD fusion products (3 MeV protons and 1 MeV tritons) and DT alphas since the gyroradius of the DT alphas is only ≈10% larger than that of the DD fusion products. There were four alpha loss detectors in TFTR at poloidal angles 20, 45, 60 and 90° below the outer midplane in the ion ∇B drift direction, as shown in Fig. 1. Only the detector at 20° was radially movable for the DT run; the other three detectors were fixed such that their pinhole apertures
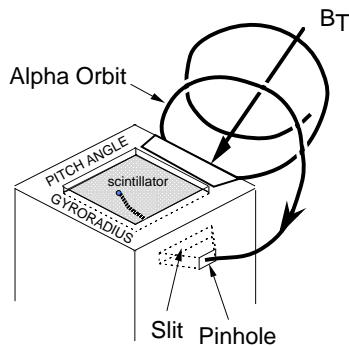

Figure 7. Schematic drawing of the lost alpha scintillator detector design. The internal design of the four detectors is similar (90, 60, 45 and 20° below the outer midplane in the ion ∇B drift direction), but only the midplane (20°) detector was radially movable. The lost alpha collector probe, based on measuring the He deposited in thin foils, was also radially movable and located near the 90° scintillator detector.

were ≈1 cm radially behind the geometrical shadow of the poloidal ring limiters, which were about 100° toroidally from the alpha detectors. Essentially all of the calculated first orbit alpha loss could enter the apertures ≈1 cm behind the limiter shadow, since these orbits have a relatively large radial velocity component near the wall. However, the alpha orbits very nearly perpendicular to the magnetic field were blocked by the detector itself; thus these detectors could not measure any alphas which were trapped inside the local TF ripple well (this type of loss was calculated to be a small fraction of the total TF ripple loss).

The diagnostic modifications made in going from DD to DT operation are described in Ref. [55], and the absolute calibration of the P46 scintillators used for DT is described in Refs [55, 56]. The absolute calibration had an uncertainty nearly a factor of two; therefore, a relative in situ calibration was also made by normalizing the measured alpha loss to that observed at the lowest possible plasma current, where the alpha loss was dominated by the relatively well understood first-orbit loss process.

2.1.2. First orbit alpha loss

The simplest mechanism of alpha loss is first orbit loss, which occurs when the alpha trajectory hits the wall before completing its first poloidal transit. The theory for first orbit alpha loss was well known before TFTR [6–8], and it was expected that the alpha loss due to this process would be large at low plasma currents (i.e. >50% globally at $I < 0.5$ MA) and small at high plasma currents (i.e. <5% globally at $I > 2.5$ MA).

The plasma current variation of the alpha loss measured 90° below the outer midplane agreed well with the expected first orbit loss calculated using the Lorentz orbit code [57], as illustrated in Fig. 8. The vertical axis is the neutron-normalized alpha particle loss integrated over pitch angle and gyroradius, and the modelling results (hatched region) were calculated by integrating the alpha source profile over the alpha trajectories calculated backwards in time from the detector into the plasma using the measured plasma current and alpha (i.e. neutron) source profiles. The data was normalized to the model at $I = 0.6$ MA, where the first orbit loss was dominant, and all data up to $I = 2.7$ MA fit the expected first orbit loss model within the error bars. In addition, the absolute alpha loss flux also agreed with the a priori calculations within their joint uncertainty
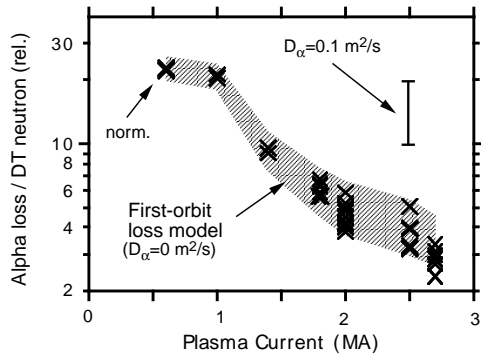
Figure 8. Alpha loss measured at the scintillator detector located 90° below the outer midplane versus plasma current. Each datapoint represents the neutron normalized alpha loss integrated over pitch angle and gyroradius for one DT discharge, and the shaded region represents modelling of the expected first orbit alpha loss without radial diffusion, normalized to the data at $I = 0.6$ MA. The vertical bar at $I = 2.5$ MA represents the calculated alpha loss for $D_\alpha = 0.1$ m^2/s, implying that the radial diffusion for counter-passing alphas near the plasma centre was considerably less than this. The vertical axis also represents the approximate percentage global alpha loss calculated for each plasma current.

(about a factor of 2). Similar results were previously obtained in TFTR using DD fusion products in D discharges (as cited in Ref. [8]).

The pitch angle and gyroradius distributions of the alpha loss measured 90° below the outer midplane also agreed well with the first orbit loss model, as shown in Fig. 9. The peak pitch angle of the alpha loss increased significantly from high to low plasma current, as expected, and the gyroradius distribution was in both cases consistent with the first orbit loss of 3.5 ± 1.0 MeV alphas (given the Doppler spread from the beam–target reactions).

Except for MHD-active DT discharges (Section 2.1.4), the time dependence of the alpha loss in all the scintillator detectors followed the time dependence of the alpha (i.e. neutron) source rate to within about ±10–20%. Thus there was no clear sign of any 'delayed' alpha loss in DT, such as previously seen in the 90° detector for DD fusion products [58]. This was somewhat surprising, since the first orbit loss process is not significantly different for DD and DT fusion products. This difference in the delayed loss between DD and DT fusion products is most likely due to their different classical collisionalities; in

particular, the 1 MeV tritons from DD reactions have a considerably larger pitch angle scattering over their slowing down time than the 3.5 MeV DT alpha. This pitch angle scattering causes only a small increase of fusion product loss in the axisymmetric case (without TF ripple) [10, 11], but with TF ripple the collisional loss can at least qualitatively explain the delayed loss observed in the 90° detector for DD fusion products (Section 2.1.3).

An attempt was made to directly measure the presence of collisionally thermalizing alphas near the plasma centre by a controlled plasma shift experiment [59]. An inward plasma shift was expected to move marginally counter-passing alphas across their passing–trapped boundary, thus allowing them to be detected at the wall in a similar fashion to the usual prompt first orbit loss. However, the experimental results showed that this additional alpha loss during an inward plasma shift did not occur. This was explained by the parallel energy gain of these passing alphas due to this inward shift, which caused their calculated orbits to remain passing in spite of the inward shift.

2.1.3.   Toroidal field ripple induced alpha loss

The other classical alpha particle loss mechanism in tokamaks is due to the TF ripple, which can cause trapped alpha orbits to diffuse rapidly due to the breaking of toroidal angular momentum conservation [12–15]. This process is a concern for future DT experiments such as ITER for which TF ripple loss of alphas might cause localized overheating of the first wall [28]. In TFTR the calculated alpha ripple loss was dominated by alpha orbits trapped in the main $1/R$ toroidal field, as illustrated in Fig. 2, for which most of the alpha loss occurs between 0 and 90° below the outer midplane. Only a very small fraction of the alpha ripple loss was due to orbits trapped between two adjacent TF coils (Fig. 1(b)).

The first TFTR measurements to look for TF ripple loss of fusion products were made in D plasmas using the radially movable 20° 'midplane' scintillator detector [60]. The results clearly showed a non-first-orbit component of the DD fusion product loss at a pitch near to that expected for collisionless stochastic TF ripple diffusion (SRD). The plasma current dependence of this midplane alpha loss was clearly different from that calculated for first orbit loss, and was similar to that expected from SRD. Direct measurements of the radial diffusion of DD fusion products were made in the shadow of small and large
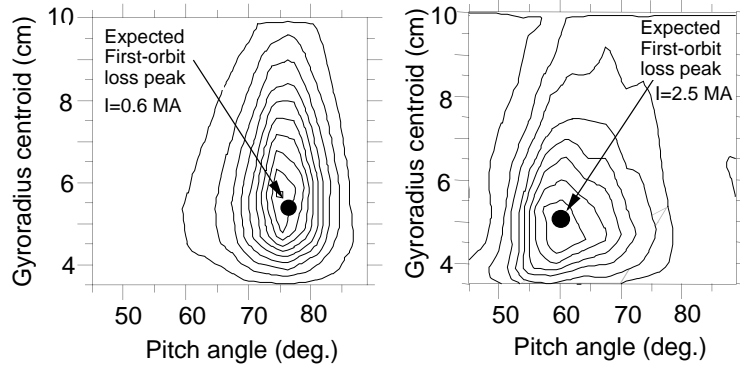
Figure 9. Typical time averaged 2-D patterns of alpha loss versus pitch angle and gyroradius as measured by the $90°$ scintillator detector in TFTR. At both low and high plasma currents the centroids of the data are consistent with the first orbit loss of alphas. The widths of the pitch angle distributions are consistent with the widths of the expected distributions; the widths of the gyroradius distributions are dominated by the instrumental width, but are also consistent with 3.5 ± 1 MeV alphas.

obstacles, which also showed a radial diffusion step size per bounce similar to that expected from the SRD mechanism (i.e. ≈ 1 cm) [61].

Similar measurements were made using the $20°$ scintillator detector for DT alphas, resulting in qualitatively similar pitch angles, plasma currents and radial dependences [62]. This was not too surprising, since the TF ripple loss process depends mainly on the ion gyroradius, which is only 10% higher for alphas than for DD fusion products. For example, the measured radial dependence of the DT alpha loss on the detector aperture position near the outer limiter shadow was similar for DD and DT fusion products, as shown in Fig. 10. These results were highly reproducible, indicating that they were not due to the variable MHD activity. At moderate plasma currents, ≥ 1.4 MA, the alpha loss observed in this detector was larger than the first orbit loss rate [62, 63], as expected from global calculations of TF ripple loss (e.g. Table 2).

However, the detailed modelling of alpha ripple loss to the midplane detector was much more difficult than initially expected, so there is presently only a partial explanation of these midplane alpha loss results in terms of TF ripple loss modelling. This origin of this difficulty can be seen from Fig. 10; namely, the detected alpha loss signal increased by over an order of magnitude as the detector aperture was moved inward by only ≈ 3 cm near the geometrical shadow of the outer midplane limiter. Clearly the modelling of these data must take into account the radial position of the detector with respect to the
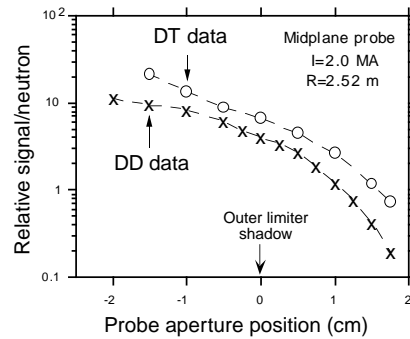

Figure 10. Radial profiles of DT alpha and DD fusion product loss near the outer limiter as measured by the $20°$ ('midplane') scintillator detector at $I = 2.0$ MA. Each data point represents the neutron normalized loss for one discharge in these radial detector scans. The horizontal axis is the radial position of the detector aperture with respect to the geometrical shadow of the (distant) poloidal ring limiter, where negative values correspond to the aperture radially inside this limiter shadow. The measured signals increase as the detector aperture is moved inwards, suggesting that the stochastic TF ripple diffusion loss is highly modified by the limiter shadowing effect. The profiles of DT and DD fusion product signals are similar, as expected from their similar gyroradii.

physical obstruction caused by the outer midplane limiters on the other side of the machine, and also by the detector probe itself. Such modelling was done for a collisionless SRD model [63], but is much more

difficult for a collisional alpha ripple loss model due to the need to follow orbits for many transits.

The most accurate available TF ripple loss model is based on the Monte Carlo guiding centre ORBIT code [14–17], which incorporates classical pitch angle scattering and thermalization and the full 3-D magnetic geometry. However, given the available computing power, only $\approx 10^3$ alpha orbits could be run for their full slowing down time using this code. Thus the global alpha ripple loss fraction of ≈ 10–20% can be calculated with good accuracy, but direct simulation of the alpha loss to the small midplane detector aperture (≈ 0.1 cm^2) would require >1000 times this number of test particles for good statistics. An approximate poloidal distribution can be found assuming a smooth toroidal first wall, but the radial distribution corresponding to the data of Fig. 10 can not be calculated directly [62].

Nevertheless, an experiment was done to systematically vary the $q(r)$ profile with respect to a baseline $I = 1.4$ MA DT discharge to determine if the relative variation of the midplane alpha loss data was consistent with the collisional TF ripple loss model [63]. It was found that, as the $q(r)$ profile and toroidal field were varied, the measured alpha loss rate (per DT neutron) did *not* scale with the calculated variations of the global collisional ripple loss fraction, as shown in Fig. 11. Note that these calculations covered the full energy e-folding time of $75\,000$ toroidal transits, since less than half the ripple induced alpha loss occurred over a 'collisionless' time of only 5000 transits. Further analysis showed that the midplane alpha loss data were at least qualitatively consistent with the Monte Carlo calculations of TF ripple loss, but that a quantitative comparison (within a factor of 2) could not be made due to inadequate statistics [63].

A significant advance in modelling the alpha ripple loss in TFTR was made by using a 3-D Fokker–Planck model which approximates the collisional and stochastic ripple diffusion to calculate the alpha ripple loss, including an improved model for the vacuum magnetic fields and the poloidal limiter shadowing effect [64, 65]. The main result from this modelling, which was later verified by the Monte Carlo code, was that the poloidal distribution of the TF ripple loss extends further towards the vessel bottom than previously expected. This was largely due to the increased inward shift of the vacuum flux surfaces, which makes the shapes of the alpha orbits near the outer midplane flattened and shifted inwards, causing the marginally confined alpha orbits
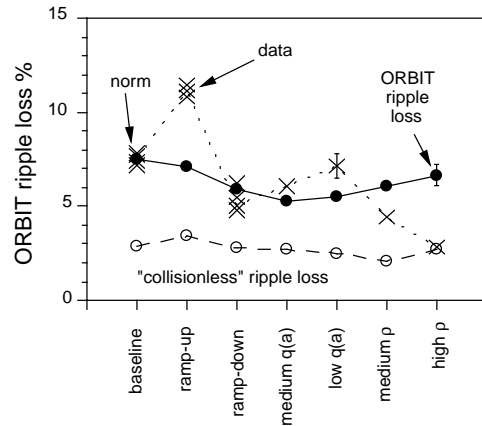

Figure 11. Measurements of the relative variation of alpha loss at the midplane probe for controlled variations of the $q(r)$ profiles and toroidal fields in TFTR. The crosses show the neutron normalized alpha loss for various discharges for a fixed radial aperture position. The solid circles show the global collisional ripple loss as calculated by the ORBIT code, normalized to the baseline $I = 1.4$ MA case and the open circles show the 'collisionless' ripple loss. The lack of correspondence between the data and the modelling is attributed to difficulty in calculating the local alpha ripple loss to the detector aperture.

to hit the limiter at larger poloidal angles. The strongest effect comes at high currents ($I \geq 1.4$ MA) and for partially thermalized alphas, since these alpha orbits most closely follow the magnetic flux surfaces.

This model has not explained the radial profile or $q(r)$ dependence of the midplane alpha loss data in Figs 10 or 11, but was successfully used to understand previous data on the plasma current dependence of the alpha loss in the 20 and 45° detectors. The measured alpha loss (per neutron) peaked at $I = 1.0$ MA in the 20° detector [62] and at $I = 1.8$ MA in the 45° detector [66], which was different from the expected first orbit loss, which decreased monotonically with increased current, as for the 90° detector data of Fig. 8. Calculations based on the 3-D Fokker–Planck ripple loss model predicted the correct plasma current dependence for both cases [65], as illustrated for the 45° data in Fig. 12. Note that this behaviour is also obtained for DD fusion products, so is not a collective alpha effect, and the good shot to shot reproducibility excludes an MHD induced effect.

In addition, this Fokker–Planck model was used to explain previously seen 'delayed' loss of partially
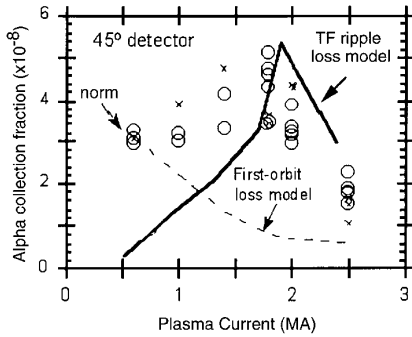
Figure 12. Measurements of the neutron normalized DT alpha (open circles) and DD fusion product (crosses) losses to the scintillator detector $45°$ below the outer midplane versus plasma current. The loss for both DT and DD fusion products peaks at $I = 1.8$ MA, but does not follow the expected dependence of the first orbit loss model. The solid curve is based on a collisional ripple loss model which includes an improved vacuum model and the poloidal shadowing of the limiter [65].

thermalized DD fusion products at $90°$ as simply the collisional TF ripple loss, which could reach the vessel bottom for small major radius plasmas with a large vacuum region at the outer midplane. Details of this analysis and further discussion of the status of the theory are given in Section 2.4, and a comparison with other diagnostic data on TF ripple loss is given in Section 8.1.

2.1.4. MHD induced alpha loss

Plasma driven low frequency MHD activity causes fluctuating internal magnetic perturbations which can cause a deterioration fast particle confinement, even without any 'collective' instability driven by the fast particles themselves. Many examples of such MHD induced loss of DD fusion products in D plasmas were seen in the scintillator detector data on TFTR, and modelling was done to calculate the expected ion loss versus the size and mode number of these perturbations [58].

The MHD activity observed in TFTR was qualitatively similar in DT and D plasmas, and MHD induced alpha loss was seen in about 10–20% of the TFTR DT plasmas [67]. Examples of MHD induced alpha loss were seen in all four of the scintillator detectors with every type of conventional MHD activity, as summarized in Table 7, for example low frequency coherent modes, high frequency kinetic

ballooning modes (KBMs), sawtooth crashes, and minor and major disruptions.

One example of MHD induced alpha loss is shown in Fig. 13 for a DT plasma with $I = 2.3$ MA and 27 MW of NBI. In this case there was an $m = 2$, $n = 1$ global mode at a frequency of ≈ 300 Hz. This mode caused up to a factor of 2 increase in the alpha loss in the $60°$ scintillator detector, but very little increase occurred in the 90 or $45°$ detectors. Evidently the MHD induced loss can be very localized poloidally (and most likely also toroidally), causing the strong modulations in time. These alpha losses can occur even without a significant degradation in plasma confinement, as seen in the unperturbed neutron rate versus time. Other examples show similar behaviour for different frequencies and mode numbers, but the largest MHD induced alpha loss can occur at other detector locations.

By far the largest MHD induced alpha loss occurred during the thermal quench just prior to major plasma current disruptions, when the rate of alpha loss often increased by up to a factor of ≈ 1000 for a few milliseconds [8, 67, 68]. It was estimated that about 10% of the confined alpha population could be lost before the current began to decay, with the largest loss measured at the $90°$ detector. This alpha loss is most likely due to the large internal magnetic field perturbations which accompany the disruption [67]. All other MHD-induced losses in high current plasmas, such as those associated with ELMs in limiter H modes [69], were comparable to first orbit loss, i.e. a few per cent globally. The relative MHD induced alpha loss appears to be somewhat less than that which occurred for DD fusion products, possibly due to the shorter slowing down time for alphas compared with 1 MeV tritons, which results in a smaller confined alpha population which is susceptible to loss via MHD activity.

The theory of MHD induced alpha loss is fairly well developed [70], and calculations of global alpha loss can be made using Monte Carlo codes, as illustrated in Fig. 5. There are two general mechanisms for coherent MHD-induced alpha loss. First, both passing and trapped alphas can undergo radial transport to the wall due to the internal field perturbations. Second, passing alphas near the plasma centre can undergo radial diffusion and become converted to trapped alphas which are promptly lost to the wall. Since the MHD frequency is low, both these mechanisms conserve magnetic moment and energy.

An analysis of the MHD induced alpha loss data was done for a DT experiment in which there was

Table 7. Types of MHD– and RF–alpha interactions in TFTR

Interaction	Frequency range (kHz)	Relative alpha loss[a]
Locked modes	$\ll 0.1$	2
Tearing modes	0.1	3
ELMs [69]	1	2
Fishbones [67]	10	0.5
Disruptions [8, 68]	10	100–1000
Sawtooth [67, 72, 91, 102]	100	10
BAE [131]	100	n.o.[b]
KBM [71, 176]	100	2
TAE [138]	100	n.o.[b]
AFM [71]	100	0
IBW [173]	10^5	n.o.[b]
ICRF [148]	10^5	2
ICE [151]	$>10^5$	n.o.[b]

[a] Maximum alpha loss in the scintillator detectors during these phenomena, normalized to alpha loss without these phenomena.
[b] n.o. means not observed on TFTR DT discharges.
Note: BAE, β-induced Alfvén eigenmode; KBM, kinetic ballooning mode; TAE, toroidal Alfvèn eigenmode; AFM, Alfvén frequency mode; IBW, ion Bernstein wave; ICE, ion cyclotron emission.

high frequency activity identified as KBMs near the β limit [71]. The alpha loss as measured in the 90° detector increased by a factor of 2 during these high frequency ($f \approx 150$ kHz), high-n ($n = 6$–10) magnetic fluctuations, and the pitch angle of the observed MHD induced alpha loss was localized at the passing–trapped boundary. The ORBIT code was used to show that there was a resonant alpha interaction near the mode rational surface which pushed counter-passing alphas across the passing–trapped boundary and out to the wall on the first trapped orbit. The code was able to predict the approximate magnitude of this loss based on the measured fluctuation level.

A somewhat similar process is likely to cause the sawtooth induced loss, which also appears at the pitch angle of the passing–trapped boundary [72]. However, the alpha loss due to low frequency modes (such as in Fig. 13) does not always occur at the passing–trapped boundary, and is probably due to an increased diffusion of trapped alphas, perhaps in conjunction with TF ripple loss.

In MHD quiescent plasmas the radial diffusion of alphas is very small ($D < 0.1$ m^2/s), indicating that their interaction with the ever present small scale turbulent fluctuations is very weak [30]. This can be deduced from the measured decrease in the alpha loss with increasing plasma current, as shown in Fig. 8, and from the confined alpha measurements described in Sections 3 and 4. The standard explanation for this is the 'orbit averaging' effect expected when the alpha gyroradius is larger than the turbulence size scale [20–23]. However, no direct correlation has yet been established between the level or structure of the turbulence with measurements of alpha particle transport (Section 8.1).

Toroidal Alfvén eigenmodes with high frequency ($\approx$100–300 kHz) and low n($n \approx 1$–5) are global MHD instabilities driven by fast ions resonant with the shear Alfvén waves in a toroidal plasma. There were several experiments in which TAEs were generated in DT plasmas (Section 6), but there was never any observable alpha particle loss associated with these TAEs. Similarly, there was no alpha loss associated with observations of Alfvén frequency modes [71], or ion cyclotron wave emission (Section 7).

2.2. Alpha collector probe

A different type of alpha loss diagnostic based on the deposition of alphas in a stack of thin metal foils was tested for the first time on TFTR, in
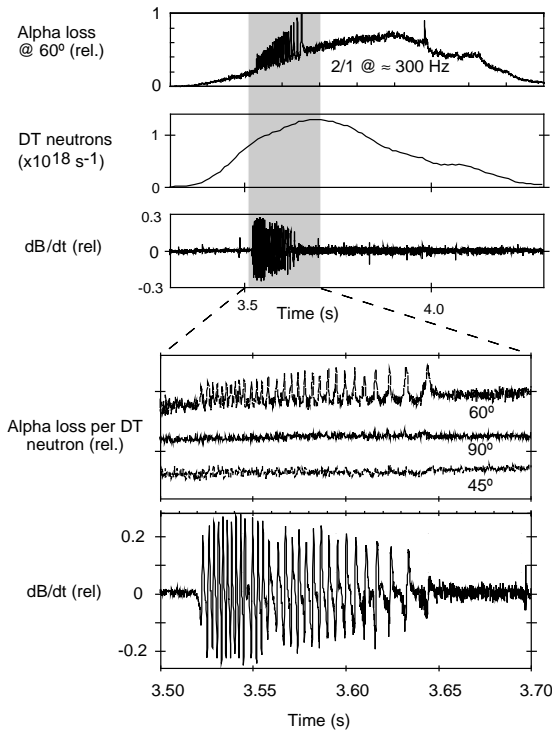
Figure 13. An example of MHD induced alpha loss in TFTR. This $I = 2.3$ MA discharge had an $m = 2$, $n = 1$ mode just after the start of 27 MW of NBI at 3.3 s. The magnetic fluctuations measured at the wall are correlated with fluctuations in the alpha loss measured at the 60° scintillator detector; the detectors at 90 and 45° show less MHD induced alpha loss. The peak alpha loss at the 60° detector during this MHD activity is about double the loss without MHD activity.

collaboration with the University of Toronto. This detector was installed on a movable probe inserted 90° below the outer midplane about 18° toroidally away from the 90° scintillator detector.

This technique was based on an idea by Langley et al. [73] to use the well known range–energy relation for alphas in metal foils to make an energy resolved, absolutely calibrated alpha loss measurement. The TFTR detector had 16 separate stacks of ten 1 μm thick aluminium foils, each located behind its own collimated port cut into the top of a radially movable probe head [74]. These ports were aligned to view eight different poloidal angle ranges in each of two vertical rows separated by about 1 cm. The absolute flux of alphas was measured by removing the foils from the vessel, vaporizing them, and

measuring their He content using a sensitive mass spectrometer at Toronto.

For each DT discharge of interest, the probe was moved into the vessel for only one DT discharge, and the alpha loss was integrated over the duration of this discharge. Two slightly different port designs were tried, and one exposure was made with each, at both at low plasma current ($I = 1.0$ MA) and a high plasma current ($I = 1.8$ MA).

Data and modelling of the total alpha loss to the detector (integrated over alpha energy) as a function of the port orientation for two cases is shown in Fig. 14 [75]. For the low current $I = 1.0$ MA cases the absolutely measured alpha loss agreed very well with the first orbit loss model calculation, as expected from the scintillator measurements (Section 2.1.2). However, for the higher current case at $I = 1.8$ MA, there was a significantly larger alpha loss than expected from the first orbit loss model for the port orientations between 20 and 80°. This discrepancy is typically a factor of 5–7 for the upper row of ports (radially inside the limiter shadow), but only a factor of typically 2–3 for the lower ports (roughly at the limiter shadow). Such a discrepancy was *not* observed in the 90° scintillator detector for these discharges, the aperture of which was ≈1 cm behind the limiter shadow.

Other data from the foils support the conclusion that it is detecting an 'anomalous' alpha loss at $I = 1.8$ MA. The average energy of the alpha loss in the ports with the anomalously large flux was only ≈2.5 ± 0.3 MeV, whereas at $I = 1.0$ MA it is close to 3.5 MeV, as expected for first orbit loss. The pitch angle distributions at $I = 1.0$ MA were consistent with the first orbit loss model, but those at $I = 1.8$ MA appeared to occur in a narrow region just above the pitch angle of the passing–trapped boundary. Only four useful foil exposures were made, so the data set is limited to these two cases.

Taken together, these observations of anomalous alpha loss in the collector foils at high current are qualitatively similar to the 'delayed loss' seen in the 90° scintillator detector in D plasmas (but not seen in the scintillator for DT plasmas). In both cases the anomaly involved a loss of partially thermalized trapped fusion products at pitch angles above the normal first orbit loss in high current plasmas. The most likely cause for the different behaviours in the collector foils and the scintillator is their different radial positions, since the upper row of foils showed a much larger level of anomalous loss, and the scintillator aperture was below the lower row of foils. The
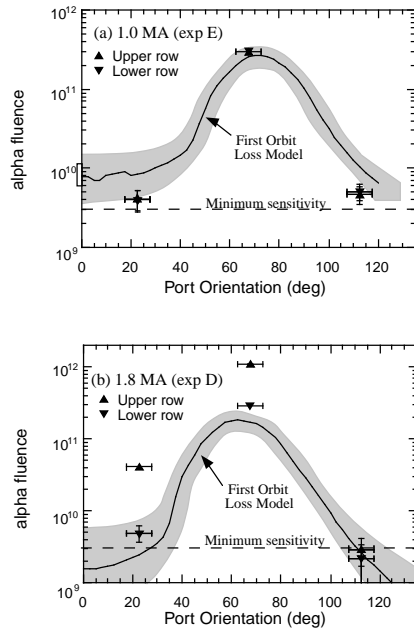
Figure 14. Alpha loss measurements made by the alpha collector probe 90° below the outer midplane. Panel (a) shows the measurements for a discharge at $I = 1.0$ MA, and panel (b) shows the measurements at $I = 1.8$ MA. At 1.0 MA the alpha loss agrees with the first orbit loss model (shaded region), but at 1.8 MA the loss is up to 5–7 times higher than the first orbit model predictions. This anomaly decreases significantly for the lower row of detector apertures, most likely due to the shadowing effect of the limiters on alphas approaching the bottom row of detectors.

most likely explanation for this delayed loss in both cases is classical collisional TF ripple loss, which can potentially reach the vessel bottom due to the influence of the vacuum fields on the marginally confined orbits (Section 2.4).

2.3. Summary of alpha loss results

The main conclusions from these alpha loss measurements are:

(a) The alpha loss measured by the scintillator detector 90° below the outer midplane agreed well with the first orbit loss model in all MHD quiescent DT discharges.
(b) The alpha loss measured by the 20 and 45° scintillators nearer the outer midplane was not consistent with first orbit loss alone, but was at

least partially consistent with models of collisional TF ripple loss,
(c) The alpha loss measured by a foil detector 90° below the outer midplane agreed with the first orbit loss model at low plasma current, but showed an anomalous alpha loss at high plasma current, particularly in the ports located inside the limiter shadow.
(d) Plasma driven MHD activity sometimes caused the alpha loss measured by the scintillators to increase by up to about a factor of 2, but no measurable alpha loss was observed due to any collective alpha effects.

2.4. Theoretical interpretations

These results present a fairly complex pattern, only part of which is understood at present. The largest uncertainty, and the most likely explanation for most of the observed anomalies, involves the effect of collisional TF ripple loss, the calculation of which was much more difficult than initially supposed.

Until recently, calculations of the alpha ripple loss indicated that it was localized to within about 20° of the outer midplane, due to the relatively small radial step per bounce of ripple diffusing trapped alphas [60–62]. However, a more realistic model for the vacuum magnetic fields has shown that collisional ripple loss can actually reach up to nearly 90° below the outer midplane in some cases [64, 65]. This effect occurs only when the plasma major radius is less than the chamber major radius of $R = 260.2$ cm; for example, most high powered DT plasmas with $R = 2.52$ m had a 20 cm wide vacuum region between the outer midplane plasma edge and the outer midplane limiter.

With this correction for the vacuum magnetic fields, the 3-D Fokker–Planck model of collisional TF ripple loss [65] can explain at least qualitatively the delayed loss of partially thermalized DD fusion products in D plasmas, for example its increase for smaller major radius plasmas, and also the partially thermalized alpha loss detected by the alpha collector probe. The key to this explanation is that the poloidal angle of the ion loss is determined by the *shape* of the outer leg of the marginally confined banana orbits near the wall, such that lower energy (partially thermalized) alphas tend to be lost nearer the bottom of the vessel in higher current discharges, consistent with the 'delayed' losses seen there.

This improved ripple loss model also explained at least qualitatively the plasma current dependences

of the alpha loss measured in the 45 and 20° detectors, which were clearly not consistent with first-orbit loss [62, 66]. The conclusion is that for $R = 2.52$ m plasmas the collisional TF ripple loss dominated the alpha loss observed in the 45° detector above $I = 1.4$ MA, and in the 20° detector above $I = 0.7$ MA [65].

However, it is still surprising that there was a clear difference between the delayed loss signatures for D and DT fusion products measured at the 90° scintillator detector, since the gyroradii of the relevant fusion products differ by only $\approx 10\%$. This difference may be due to the higher ratio of pitch angle scattering to thermalization rate for 1 MeV tritons with respect to 3.5 MeV alphas, which tends to increase the collisional ripple loss of the tritons [65]. However, there is no direct experimental evidence for this, in part due to the difficulty of separating the effects of tritons and protons in D plasmas.

Another generic problem in interpreting the lost alpha results is the complexity of the actual outer wall structure, combined with the relatively small size of the detector apertures. This makes the calculation of the local alpha loss to these detectors prohibitively difficult, except when this loss is unshadowed by the limiters, as for first-orbit loss. Thus there is presently no quantitative explanation of the radial scans of the midplane probe (Fig. 10), nor the variations with $q(r)$ (Fig. 11), although the collisional ripple loss model can a least qualitatively explain some of these data [63–65].

The measured MHD induced alpha loss in DT was similar to that observed for DD fusion products, and is most likely due to the internal magnetic perturbations and reconnection. Modelling of such losses has been done for idealized mode structures [41, 67], but a quantitative evaluation of the measurements is complicated by the variability of the MHD activity from shot to shot, and by lack of knowledge of the internal magnetic structure. The simplest MHD induced alpha loss mechanism involves movement of counter-passing alphas across the passing–trapped boundary directly to the wall, but the MHD induced diffusion of trapped alphas involves the same difficulty of calculating the poloidal and radial distributions as the TF ripple loss.

2.5. Directions for future research

The most important need for further data concerns the spatial distribution of the alpha loss to the wall, since any highly localized alpha loss in a large DT reactor might cause impurity flux or even damage to any insufficiently protected first wall components. The lost alpha detectors in TFTR provided very detailed information useful for identifying various alpha loss mechanisms, but they were like 'microscopes' which covered only a very small fraction ($\approx 10-8$) of the vessel wall area.

Thus there is a need to develop large area alpha detectors which could directly evaluate the alpha loss fraction and location over a large fraction of the vessel wall. The simplest system would be an infrared imaging system to measure the heat load to the wall, as was done for beam ion and RF tail ion loss in JT-60U [38]. However, this metho has no intrinsic species, pitch angle or energy resolution, and would most likely work only for DT plasmas which have a reasonably high Q of about 1. Alternatively, a large area alpha collector panel might be inserted at the wall, but it would have to withstand high heat flux to measure the most interesting regions of alpha loss, and would probably need to be remotely removed for analysis.

Localized alpha loss detectors could still be useful for 'spot checks' of the pitch angle, energy and time dependences. Possible detectors include Faraday cups [36, 76], diamond detectors [32], solid target deposition samples [77] or high temperature scintillators. However, such detectors would probably need to be removable to accommodate radiation damage to the detector elements and signal transmission components.

Finally, there is a need for improved numerical modelling of the alpha particle TF ripple and MHD induced loss which takes into account the detailed 3-D geometry of the outer magnetic flux surfaces and the tokamak first wall, including the alpha detectors themselves. This does not necessarily involve new physics, but does require new ways to speed up Monte Carlo calculations and to make analytic estimates for the finite gyroradius effects. Only with such improvements in modelling will it be possible to understand the data from localized alpha loss detectors, and then to make realistic predictions of the first wall heat load due to alpha loss in a tokamak reactor.
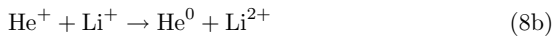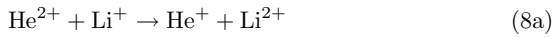
3. Pellet charge exchange diagnostic measurements

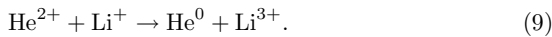Confined trapped alpha energy spectra and differential radial density profiles in TFTR DT plasmas

were obtained with the PCX diagnostic [78] which measured high energy ($E_\alpha = 0.5$–3.5 MeV) trapped alphas ($V_\parallel/V = -0.048$) at a single time slice ($\Delta t \sim 1$ ms) with a spatial resolution of $\Delta r \sim 0.05$ m. A brief description of the measurement technique and instrumentation is given in Section 3.1. A review of the PCX measurements is given for MHD quiescent plasmas in Section 3.2 and for MHD active plasmas in Section 3.3. Applications of the PCX diagnostic to the measurement of ICRF driven energetic minority H [79], ^{3}He [80] and T [81] ions, which were useful in validating the diagnostic technique and analysis procedure, are not reviewed here. A summary of the PCX measurements and suggested directions for future work is given in Section 3.4.

3.1. PCX measurement technique and instrumentation

In the PCX diagnostic on TFTR [82], low-Z impurity pellets were injected along a midplane major radius. For most experiments, cylindrical Li or B pellets of 2.0 mm diameter by $\sim$2.0 mm length were injected with velocities in the range of 400–600 m/s and typically penetrated to $r/a \sim 0.2$ during the postbeam phase. Upon entering the plasma, the pellet produced a toroidally elongated ablation cloud. Using Li pellets as an example, a small fraction of the alphas incident on the ablation cloud is neutralized either by sequential single electron capture,

$$\text{He}^{2+} + \text{Li}^+ \rightarrow \text{He}^+ + \text{Li}^{2+} \tag{8a}$$

$$\text{He}^+ + \text{Li}^+ \rightarrow \text{He}^0 + \text{Li}^{2+} \tag{8b}$$

or by double electron capture

$$\text{He}^{2+} + \text{Li}^+ \rightarrow \text{He}^0 + \text{Li}^{3+}. \tag{9}$$

If the line integral target density for particles traversing the cloud is sufficiently large, then the fraction of particles emerging from the cloud as neutrals approaches the equilibrium fraction, $F_0^\infty(E)$, which is independent of the linear density of the cloud. Pitch angle scattering and energy loss are not important at the pellet ablation cloud densities expected in TFTR [83]. By measuring the energy distribution, dn_0/dE, of the resultant helium neutrals escaping from the plasma, the energy distribution of the incident alpha particles, dn_α/dE, can be determined using

$$dn_\alpha/dE \propto K(E)dn_0/dE \tag{10}$$

where

$$K(E) = \left(F_0^\infty(E)v_\alpha \, \frac{\Omega}{4\pi} \, \eta(E)\Delta E \right)^{-1} \tag{11}$$

and $F_0^\infty(E)$ is the neutral equilibrium fraction, V_α is the ion velocity associated with energy E, $\Omega/4\pi$ is the solid angle of the analyser, $\eta(E)$ is the calibrated analyser detection efficiency and ΔE is the energy resolution of the analyser.

The neutral equilibrium fractions, $F_0^\infty(E)$, used for alphas and tritons are obtained from modelling calculations [83, 84]. The ion cross-sections entering this evaluation were calculated using the classical trajectory Monte Carlo (CTMC) method developed by Olson, and the electron cross-sections were obtained using the data compiled by Janev [85]. Since the PCX was not absolutely calibrated, the main uncertainty was in the energy dependence of $F_0^\infty(E)$, which was about a factor of 2 from the lowest to the highest alpha energy. The neutral particle analyser (NPA) detection efficiency, $\eta(E)$, was calibrated [86] for alphas using megaelectronvolt helium ion beams generated by a cyclotron accelerator and was derived for tritons using hydrogen ions. The re-ionization of neutral alphas coming out of the plasma was negligible for alpha energies above about 0.5 MeV, as was the neutralization cross-section for knock-on deuterons in the Li/B pellet clouds.

The escaping helium neutrals were mass and energy analysed using a high energy (0.3–3.7 MeV for ^{4}He) NPA [86]. The NPA viewed the cloud surrounding the radially injected pellet from behind at a toroidal angle of 2.75° to the trajectory of the pellet. As a result, only near perpendicular energetic ions with velocities close to $v_\parallel/v = -0.048$ were detected by the PCX diagnostic. The radial position of the pellet as a function of time was measured using a linear photodiode array situated on the top of the vacuum vessel. By combining this measurement with the time dependence of the PCX signal, radially resolved fast ion energy spectra and radial profiles of the alpha signal were derived with a radial resolution of $\sim$0.05 m.

In the TFTR DT experiments, pellets typically were injected 0.1–0.3 s after termination of the neutral beam heating. This timing delay led to deeper penetration of the pellet as a result of decay of the plasma electron temperature and density, as well as to enhanced signal to noise ratios because the neutron and gamma ray induced background decayed significantly faster than the confined alpha particle population [82]. Because of the long alpha

slowing down time of 0.3–0.5 s in TFTR DT discharges, alphas observed at the pellet injection time are representative of the alphas during the DT beam phase.

The PCX alpha profiles are relative measurements, since the diagnostic is not absolutely calibrated. While the instrumental response of the NPA was absolutely calibrated, the absolute efficiency for neutralization of the measured ions by the pellet ablation cloud is uncertain due to uncertainties in the spatial distribution of ionization states in the cloud. It has been shown that provided the line integral pellet density in the cloud is sufficiently high that the charge changing reactions are independent of the density and attain an equilibrium fraction, as expected in the TFTR applications, the details of the pellet ablation cloud have little effect on the measured energy distribution but do have a strong effect on the absolute alpha density measurements [83].

The experimental data were compared with modelling results obtained using TRANSP which is a 1 1/2-D transport code (calculations of magnetic equilibrium are 2-dimensional) that uses measured plasma parameters along with some additional assumptions to model plasma discharges. While TRANSP provides a good calculation of the alpha and triton distributions integrated over all pitch angles, for proper simulation of the PCX measurements the pitch angle should be constrained to account for only the deeply trapped particles. For this purpose, a Fokker–Planck post-TRANSP (FPPT) processor code [87] was developed which is based on a numerical solution of the drift averaged Fokker–Planck equation. FPPT uses the radial and energy profiles of the pitch angle integrated alpha source from TRANSP to calculate alpha distributions for experimental conditions specific to the PCX measurements.

3.2. PCX measurements in MHD quiescent plasmas

The alpha particle distributions measured by the PCX diagnostic can be influenced by the effects of classical slowing down and pitch angle scattering, stochastic diffusion associated with toroidal magnetic field ripple [88] and MHD activity [84]. In order to separate the classical behaviour from the other effects, PCX measurements were obtained during MHD quiescent discharges in the plasma core region where stochastic ripple diffusion effects are negligible. This 'plasma core' is taken to be the region well inside the boundary determined using the expression provided by the GWB theory in Eq. (7).

3.2.1. Monotonic shear discharges

The alpha distribution from 1.0–3.5 MeV was obtained using a single boron pellet injected 200 ms after termination of a 1.0 s beam pulse in a supershot discharge, as shown by the solid circles in Fig. 15(a), with the following parameters: major radius $R = 2.52$ m, minor radius $a = 0.8$ m, plasma current $I = 1.5$ MA, toroidal field $B = 5.2$ T and neutral beam heating power $P_{NBI} = 16$ MW. Also shown (solid squares) is the energy spectrum measured for a 'beam blip' case ($P_{NBI} = 20$ MW), where the boron pellet was injected 20 ms after a beam pulse of only 100 ms duration. The curves are the FPPT simulations of the PCX measurements. Reasonable agreement is seen between the data and the FPPT code results, which indicates that the alpha particles slow down classically.

The alpha slowing down spectrum for the 1.0 s beam pulse case in Fig. 15(a) was modelled to derive information on the global alpha confinement time, $\tau_{c\alpha}$, as shown in Fig. 15(b). The dashed curves show the FPPT calculations where the alpha velocity e-folding time is taken from TRANSP to be $\tau_{\alpha e} = 0.32$ s for cases where $\tau_{c\alpha}/\tau_{\alpha e} = 3.0, 1.5, 0.8$ and 0.4 are assumed. The solid curve shows the FPPT calculation assuming that $\tau_{c\alpha} \gg \tau_{\alpha e}$, i.e. $\tau_{c\alpha} = 300\tau_{\alpha e}$. In comparison with the FPPT simulation, the PCX alpha slowing down spectrum is consistent with an alpha confinement time of $\tau_{c\alpha}/\tau_{\alpha e} > 3.0$. This further supports the assertion that the alpha particles thermalize classically [89], which is important for good alpha heating in a fusion reactor.

The PCX diagnostic measures trapped alpha particles at the midplane with small pitch angle ($V_\parallel/V = -0.048$), which are very sensitive to toroidal magnetic field ripple. During pellet penetration, the rise of the PCX alpha signal was delayed relative to the pellet light emission. The delayed rise of the alpha signal correlated with the pellet crossing inside the ripple loss boundary for the trapped ions viewed by the PCX. This signal behaviour was used in a study to examine the scaling of the GWB theory (Eq. (7)) with the q profile and energy [88, 90]. Over the range of q profile variations and alpha energies available in this study, the PCX measured ripple boundary scaled with q and E in a manner consistent with the GWB ripple theory. However, the PCX measured boundaries consistently occurred at smaller major radii than predicted by GWB theory,
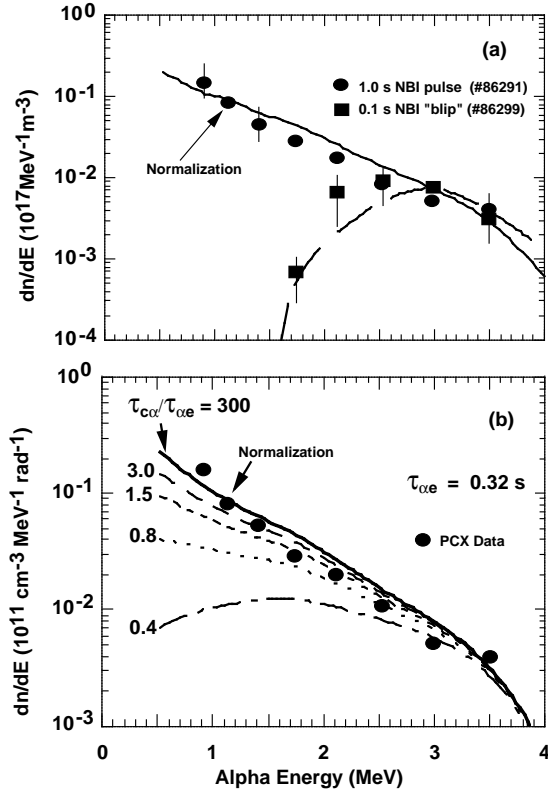
Figure 15. (a) PCX measured alpha energy spectra near the plasma core ($r/a \approx 0.1$) compared with FPPT simulations during the fully slowed down phase (circles and solid curve) and the partially slowed down phase (squares and dashed curve). (b) FPPT modelling of the alpha slowing down spectrum for the 1.0 s beam pulse used to derive information on the global alpha confinement time, $\tau_{c\alpha}$. In comparison with the FPPT simulation, the PCX alpha slowing down spectrum is consistent with an alpha confinement time of $\tau_{c\alpha}/\tau_{\alpha e} > 3.0$. The agreement between measurements and modelling in this figure indicates that alpha particles thermalize classically in the core of MHD quiescent discharges.

with an average difference of $\sim$0.06 m. Such a difference is not too surprising, since the GWB theory does not include finite banana width and Larmor orbit effects.

The shape of the alpha density profile was measured in the core of MHD quiescent supershot discharges using the PCX diagnostic. Figure 16(a) presents radial profiles of alphas with energies of 0.64, 0.80, 1.0, 1.2 and 1.4 MeV measured 0.3 s after termination of 20 MW beam injection, normalized at $R = 2.65$ m. Also shown is the GWB [12] stochastic
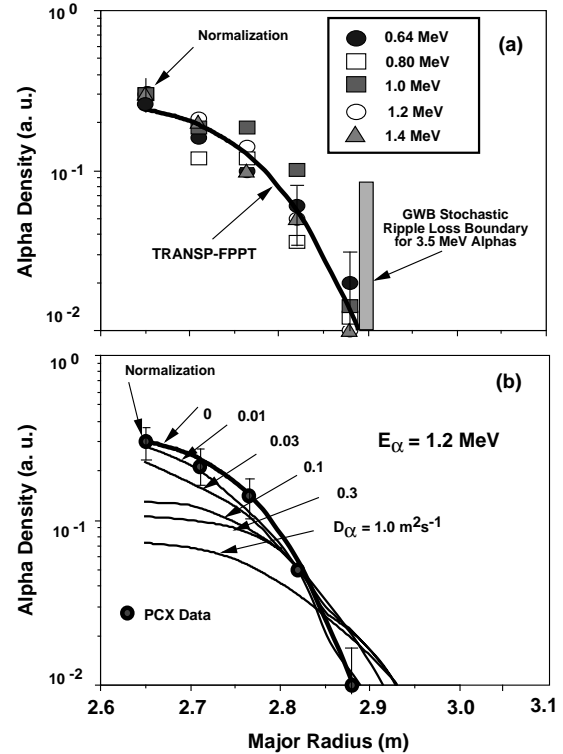

Figure 16. (a) Radial profiles of the confined alphas as measured by the PCX diagnostic in a sawtooth-free discharge (No. 84550), showing good agreement with FPPT modelling, which includes stochastic ripple diffusion. The measured alpha profiles were similar for all energies and were delimited spatially by the GWB stochastic ripple loss boundary for $E_\alpha = 3.5$ MeV. The solid curve shows the FPPT profile simulation for $E_\alpha = 1.0$ MeV, which includes this ripple loss boundary. Panel (b) shows that in comparison with the FPPT simulation, the PCX radial profiles of the alpha signal are consistent with a diffusion rate of $D_\alpha < 0.01$ m^2 s^{-1}. This is comparable to the neoclassical diffusivity and indicates that there is no significant radial transport.

ripple diffusion radial boundary corresponding to an alpha energy of 3.5 MeV. Alphas born outside this boundary are rapidly lost as a result of stochastic ripple diffusion. Only the 3.5 MeV trapped alphas born inside the stochastic ripple boundary are confined and can slow down to produce the measured profiles. The self-similarity of the profiles as the alphas slow down is further evidence that significant radial transport does not occur.

The PCX radial profiles of the alpha signal, such as those shown in Fig. 16(a), were analysed to obtain

information on the radial transport of trapped alpha particles using the FPPT code. However, the FPPT code is based on the method of integration over the particle characteristics, which does not allow inclusion of the second derivative operator. Thus, FPPT does not have pitch angle scattering in the collisional operator, which results in radial transport, and therefore the FPPT code cannot treat the diffusion self consistently. Nevertheless, a diffusive type equation can be constructed within the FPPT formalism to model radial diffusion [87]. The results of this procedure are shown in Fig. 16(b) for a fixed alpha particle energy of $E_\alpha = 1.2$ MeV. It can be seen that the best fit to the measured PCX profile occurs for the smallest diffusion value, $D_\alpha < 0.01$ m^2 s^{-1}, which is comparable to the neoclassical diffusivity and indicates that there is no significant radial transport.

3.2.2.   Reversed shear discharges

In monotonic shear $q(r)$ profiles, in the absence of any MHD activity, the radial profiles of alphas measured by the PCX have shapes similar to those shown in Fig. 16, which are defined by the source function and the ripple losses for newly born alphas. In reversed shear discharges which are characterized by an elevated central q factor, the measured alpha radial profiles of higher energy ($\sim$1.7 MeV) alphas were observed to be significantly broader than those for lower energy ($\sim$0.5 MeV), as shown in Fig. 17. Enhanced collisional stochastic ripple loss due to the high $q(0)$ of reversed shear discharges appeared to be the cause of this behaviour. Calculations of the toroidal ripple loss were made for alpha particles in a reversed shear plasma [17] using an enhanced version of the ORBIT code [13] which utilizes a rapid, accurate algorithm for the stochastic free domain and includes pitch angle scattering and slowing down. ORBIT modelling of reversed shear discharges was in agreement with the q-dependent alpha profiles observed [90] and predicted the general characteristics of alpha loss in reversed shear which clarified how a hollow profile could arise.

3.3.   PCX measurements in the presence of MHD activity

MHD activity (e.g. sawtooth oscillations and TAE activity) can transport alphas from the plasma core which might affect ignition and/or damage of the first wall components of the vessel by feeding the alphas into the stochastic ripple loss region. In DT
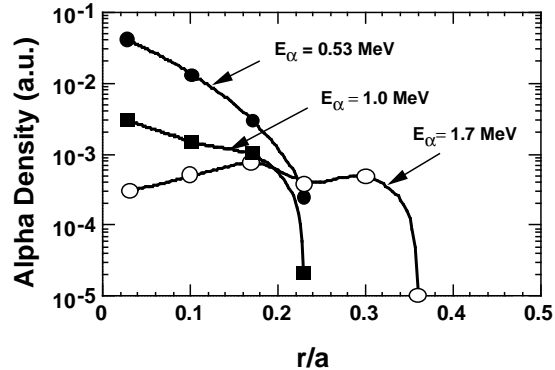

Figure 17. Redistribution of trapped alpha particles measured by the PCX diagnostic in reversed shear discharges in which the plasma core region was characterized by an elevated q factor, $q(0) \sim 4$, negative magnetic shear. Depletion of alpha particles in the core and increased profile broadening with increasing alpha energy were found.

experiments on TFTR, the behaviour of fast confined alphas in the presence of sawtooth activity was measured using the PCX diagnostic which showed a strong depletion of the alpha core density and transport of the alphas radially outwards well beyond the $q = 1$ surface after a sawtooth crash, as discussed in Section 3.3.1. In addition, PCX measurements have been obtained in discharges in which TAE activity occurs in conjunction with reduced shear operation, as discussed in Section 3.3.2.

3.3.1.   Alpha redistribution due to sawtooth oscillations

PCX measurements and modelling of alpha redistribution due to sawtooth oscillations were performed in standard TFTR DT supershots [91], with $I = 2.0$ MA, $B = 5$ T, $R = 2.52$ m, $a = 0.87$ m and $P_{NBI} = 20$ MW of DT neutral beam power injection. Sawteeth did not normally occur during beam injection in supershots. However, large sawteeth began to develop 0.2–0.3 s after the termination of beam injection when the plasma β dropped below the level required to suppress sawteeth. To obtain PCX data, a Li pellet was injected before and after the sawtooth crashes in sequential similar discharges. Measured radial profiles for alpha energies of 0.8 and 1.2 MeV before and after the crash are shown in Fig. 18. The alphas were depleted in the core and redistributed to well outside the $q = 1$ radius, but were not observed beyond the stochastic ripple loss
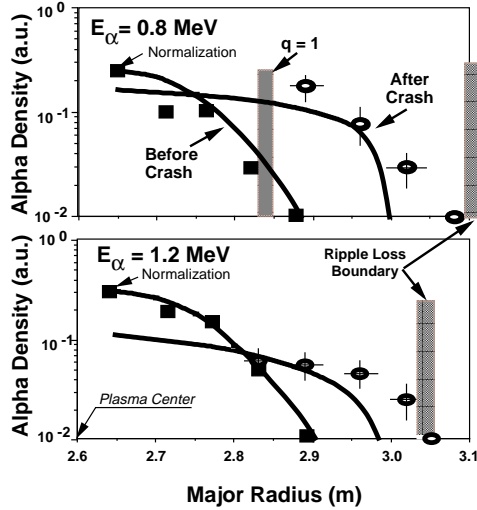
Figure 18. In the presence of strong sawtooth activity, alphas were depleted in the core and redistributed to well outside the $q = 1$ radius, but were not observed beyond the stochastic ripple boundary for the associated energy. The observed broadening decreased with increasing alpha energy. Reasonable agreement is seen between the PCX sawtooth redistribution measurements and the FPPT simulation for both pre-sawtooth radial profiles (squares, discharge 84550) and the post-sawtooth redistribution (circles, discharge 84549). Measurements could not be made inside $q = 1$ after the crash due to insufficient pellet penetration.

boundary corresponding to the alpha energy being measured. The broadening decreased with increasing energy, as did the radius of the stochastic ripple loss boundary.

A model based on generation of a helical electric field during the crash timescale, $\tau_{cr} \sim 10^{-5}$–10^{-4} s, was incorporated in the FPPT code for simulation of the sawtooth redistribution observed by the PCX diagnostic [87]. This electric field leads to a change of the alpha energy due to this toroidal drift motion. In FPPT, we introduced a simple analytical transformation formula for alpha particle energy redistribution, which was previously shown to obey a diffusion type of equation [92]. In this approach, particles can undergo significant displacement within the alpha mixing radius during the crash. The interaction of the fast particles with the perturbed electric field can be considered as resonant, even though the mode itself has very low frequency and was assumed not to be rotating during the short crash. Therefore, particles with energy higher than some

critical value, E_{cr}, perform toroidal precession during the crash and do not interact with the perturbed electric field. This critical energy, $E_{cr} = 2\omega_c m_\alpha r R/\tau_{cr}$, is defined [92, 93] from comparison of the particle toroidal precession time and the sawtooth crash time, where ω_c is the cyclotron frequency, m_α is the alpha particle mass and r, R are the minor and major radii, respectively. E_{cr} plays the role of an adjustable parameter in simulations of the experimental data and avoids the need for precise knowledge of the crash time τ_{cr}. Figure 18 shows a comparison of the PCX data with the sawtooth redistribution model for measured alpha energies of 0.8 and 1.2 MeV. Within the accuracy of the PCX measurements and the model, good agreement was observed in comparisons of the experimental alpha radial profile and the model.

Comparison of the PCX and α-CHERS data with lost alpha measurements showed that, in the sawtooth crashes, radial redistribution of the alphas occurs without significant ripple losses of particles. The sawtooth oscillations effectively transport the alphas outwards along the major radius close to the stochastic ripple domain. Under conditions of larger mixing radius than occurs in TFTR, this transport might lead to enhanced ripple loss of fusion alpha particles in tokamaks.

3.3.2. Alpha redistribution in the presence of TAE activity

Purely alpha particle driven TAEs with toroidal mode numbers $n = 1$–6 were observed in DT plasmas on TFTR (Section 5). The peak measured TAE amplitude was $\tilde{n}/n \sim 10^{-4}$ at $r/a \sim 0.3$–0.4, which corresponded to an estimated peak internal amplitude $\tilde{B}/B \sim 10^{-5}$, whereas $\tilde{B}/B \sim 10^{-8}$ was measured at the plasma edge, confirming the core localization of the mode activity.

PCX radial profiles of the alpha signal at different energies in the presence of a TAE ($n = 3$, $\tilde{B}/B \sim 10^{-5}$) are shown in Fig. 19. These were taken in a single discharge (No. 94001) having plasma current 1.7 MA, neutral beam power 25 MW, $q(0) = 2.35$ and a flat $q(r/a)$ profile as measured by MSE in the plasma core. These measurements were performed 150 ms after the TAE activity ended. The solid curves indicate experimental data, while the dashed curves show classical predictions (without TAE activity). With TAE activity, the redistribution becomes broader and more depleted in the core with increasing alpha energy. In addition, deviation
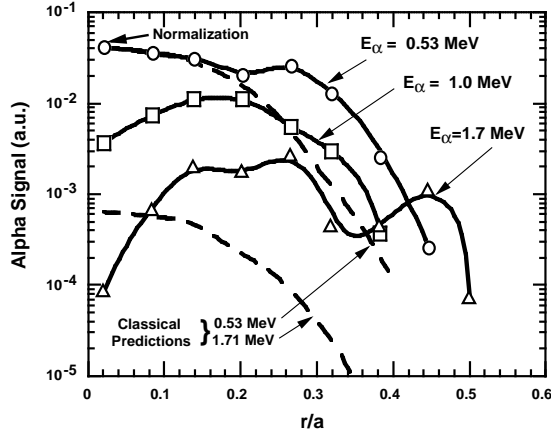
Figure 19. Redistribution of trapped alpha particles was measured by the PCX diagnostic in the presence of TAEs which had very weak fluctuation levels $\tilde{B}/B \sim 10^{-5}$ in the core. The redistribution became broader and more depleted in the core with increasing alpha energy. Significant redistribution occurred only in conjunction with an elevated central q factor $q(0) \sim 2$ or higher.

of the alpha energy spectra from classical behaviour was observed.

In view of the weak magnetic fluctuation levels attending the core TAE activity, it is natural to question how this could produce the significant modifications of the alpha energy spectra and radial distribution observed by the PCX diagnostic. Analysis of the resonance condition of trapped alphas during their interaction with TAEs, which included finite banana width effects, showed that near the plasma centre the resonance was very broad for trapped alphas in terms of their vertical displacement. This meant that trapped particles in the resonance zone could be displaced vertically and lost from the PCX pitch angle viewing window. Only a very small change in the alpha energy due to interaction with the TAEs would be needed to cause a displacement of the trapped alpha orbit from the narrow pitch angle window viewed by the PCX diagnostic to produce the observed redistribution. On the other hand, analysis indicated that the elevated central q which leads to destabilization of the TAEs by alphas also leads to significant ripple induced redistribution of trapped alpha particles, which in itself is a plausible explanation for the PCX data for discharges with $q(0) > 2$ and low shear. Thus an ambiguity remains about the cause of the redistribution shown in Fig. 19, since the analysis could

not clearly separate the high-q and low shear effect from the TAE effect. For medium-q discharges ($1.4 < q(0) < 2.0$), uncertainties in the measured values of central q and shear did not allow definite conclusions regarding ripple induced redistribution. In order for the TAE–particle interaction modelling of alpha redistribution to be consistent with the PCX measurements in these discharges, the TAE amplitude needed to be at least an order of magnitude higher than was measured. Further experiments and modelling will be needed to understand the relative importance of these two mechanisms in the redistribution of trapped alpha particles.

3.4. Summary of PCX measurements and directions for future work

Using the PCX diagnostic, which views deeply trapped alpha particles ($v_\parallel/v = -0.048$), the first measurement of the alpha slowing down distribution up to the 3.5 MeV birth energy was obtained using B pellet injection. In the core of MHD quiescent DT supershot discharges in TFTR, good agreement was obtained between the PCX measurements of the confined trapped alpha particles (and tritons) and TRANSP and FPPT model predictions. This agreement implies that the alphas and tritons are well confined and slowing down classically.

In these monotonic shear supershots, the radial profiles of the alpha signal were centrally peaked and their shape did not depend on energy. However, in sawtooth-free discharge scenarios with reversed shear operation, the PCX diagnostic revealed radial profiles of the alpha signal that were significantly broader than those for monotonic $q(r)$ supershots. ORBIT modelling of reversed shear and monotonic shear discharges were both in agreement with the q-dependent alpha profiles observed.

In the presence of strong sawtooth activity, the PCX diagnostic observed significant redistribution of the alpha radial profile, wherein alphas were depleted in the core and redistributed to well outside the $q = 1$ radius, but apparently not beyond the energy dependent stochastic ripple loss boundary. The helical electric field produced during the sawtooth crash played an essential role in the successful modelling of the sawtooth redistribution data (Section 3.3.1), and redistribution of trapped alpha particles in the presence of core localized TAE activity was observed (Section 3.3.2). However, ambiguity remains about the cause of this redistribution, since the analysis could not clearly separate the ripple induced

redistribution due to the high q and low shear in such discharges from the TAE–alpha interaction effect.

Although the PCX diagnostic yielded an extensive set of alpha particle measurements during the TFTR DT experiments, application of the diagnostic was constrained by several factors. First, the strong perturbation of the plasma discharge due to injection of impurity pellets limited its application to judiciously selected discharges or to experiments designed specifically for PCX purposes. Second, adequate pellet penetration was not obtained during high power neutral beam operation, so the PCX measurements had to be made 0.1–0.3 s after termination of beam injection [82]. More advanced injectors with pellet velocities approaching an order of magnitude greater than available on TFTR now exist and should be considered in any potential future application of this diagnostictechnique, such as on ITER [94]. Third, absolute measurement of the alpha density was not possible since the absolute efficiency for alpha neutralization by the pellet ablation cloud was unknown due to uncertainties in the spatial distribution of ionization state mix in the cloud. Finally, for the TFTR DT experiments the PCX line of sight was fixed at an angle of 2.75° to the major radius viewing in the co-direction. This constrained the diagnostic to view trapped alpha particles on the inner leg of their banana orbits with pitch angles in a narrow range around $v_\parallel/v = -0.048$. A diagnostic arrangement capable of scanning about $\pm10°$ to measure alphas on both inner and outer legs of the banana orbits over a significant pitch angle range would provide access to a very rich variety of confined trapped alpha phenomena. Ideally, the impurity pellet injector should be scanned together with the diagnostic in order to minimize data interpretation issues that could be expected to arise due to viewing different regions of the ablation cloud when scanning.

4. Alpha charge exchange recombination spectroscopy measurements

The α-CHERS (Alpha CHarge Exchange Recombination Spectroscopy) diagnostic was implemented for DT operation of TFTR to observe non-thermal confined alpha particles in the low energy range of $E_\alpha \leq 0.7$ MeV. A brief description of the measurement technique and instrumentation is given in Section 4.1, followed by a summary of the alpha physics results obtained during DT operation of TFTR in

Section 4.2. The initial measurements of energetic ^{3}He ions produced by ICRF heating in TFTR [95], which were important in developing the instrumentation and data analysis algorithms, are not reviewed here. Possibilities for further development and application of the α-CHERS diagnostic are discussed in Section 4.3.

4.1. α-CHERS measurement technique and instrumentation

The α-CHERS diagnostic measured visible light emission excited by charge exchange between alpha particles and D atoms injected by the TFTR heating neutral beams,

$$\mathrm{He}^{2+} + \mathrm{D}^0 \rightarrow (\mathrm{He}^+)^* + \mathrm{D}^+$$
$$\rightarrow \mathrm{He}^+\ + \mathrm{D}^+ + \gamma(n = 4{-}3). \qquad (12)$$
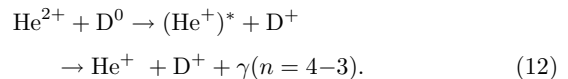
The He$^+$ ion can be created in an excited state, which stabilizes by emitting line radiation appearing as a Doppler shifted wing on the thermal line. The TFTR α-CHERS system observed the He$^+$ 468.6 nm line, and the viewing geometry was chosen to view the red side of the Doppler shifted emission spectrum of the energetic alphas to avoid the intense C edge lines on the short wavelength side of the He$^+$ 468.6 nm line. The charge exchange cross-section peaks at low relative collision energy ($\sim$30 keV/amu), limiting the alpha energy range observable with the TFTR heating beams ($\sim$50 keV/amu) to $E_\alpha \leq 0.7$ MeV. The energetic alpha signal was less than 1% of the bremsstrahlung background signal, so a high throughput optical system with low noise detectors was required to observe it.

The α-CHERS instrumentation as used during the TFTR DT run [96] had an array of five spatial channels which viewed the beams from a single TFTR beam line in the toroidal midplane, as shown in Fig. 20. These lines of sight intersected the beams at major radii in the range $R = 2.72$–3.13 m, corresponding to $r/a \approx 0.05$–0.6 in a high power DT discharge. The lines of sight were deployed in this way because the non-thermal alpha signals were too weak to be observed at larger radii due to the very peaked alpha density profiles. The lines of sight were nearly tangential to the flux surfaces at their intersection with the beams, resulting in radial resolution of 0.02–0.03 m for an individual spatial channel. The light from each channel was brought to the remotely-located spectrometers by 10 optical fibres (1 mm diameter) filled at $f/2$. The light from one
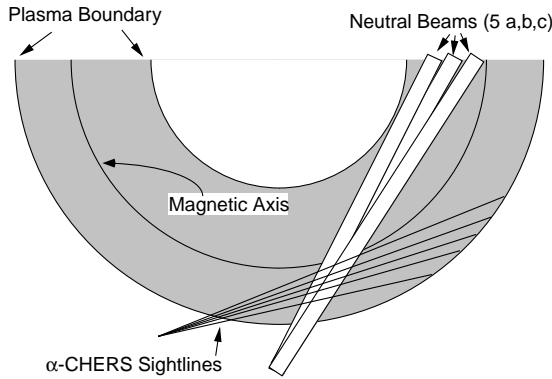
Figure 20. Schematic diagram of α-CHERS lines of sight and neutral beam trajectories on TFTR. The α-CHERS diagnostic measures alphas in the energy range 0.15–0.6 MeV, and primarily observed passing alphas.

spatial channel was coupled to one of three 0.275 m, $f/3.8$ Czerny–Turner spectrometers with 0.7×40 mm entrance slits. The 3600 lines/mm gratings that were used resulted in ∼0.5 nm spectral resolution.

Remotely controlled input optics coupled the light from the fibres to the spectrometers and allowed selection of the spatial channel to be viewed by each spectrometer. Three radii could be observed in a single discharge, making it necessary to combine data from two similar shots to obtain a five point radial profile. Each spectrometer was equipped with a low read-out noise, back illuminated CCD camera. As a result of the high optical throughput and low noise detection, the noise on the signal was determined by the photon statistics. Since the alpha signal was a small fraction of the bremsstrahlung background, the noise on the alpha signal was dominated by the photon statistics of the bremsstrahlung signal. The cameras were read out at 0.05 s intervals, but the data were averaged over 0.1–0.4 s intervals to improve the signal to noise ratio. The entire system was radiometrically calibrated, so absolute measurements of the alpha density were possible.

The energetic alpha signal was extracted from the spectrum in the following way, described in detail in Ref. [97]. For each discharge in which the alpha signal was to be measured, a background discharge was performed with the same total beam power, but with the beams observed by α-CHERS turned off during the period of interest. This 'background' discharge had a similar bremsstrahlung spectrum to that of the 'signal' discharge, but without the alpha signal. The edge impurity lines were fitted and removed from

the spectra from both discharges. This line removal procedure was done carefully to avoid introduction of significant systematic errors. The data were then averaged over 0.8 nm spectral bins, resulting in alpha energy resolution of 0.03–0.09 MeV per bin. The spectra were normalized to each other in the region of the spectrum corresponding to alpha energies of 0.7–1.0 MeV, where the alpha signal was negligible due to the small charge exchange cross-section. The normalized background spectrum was then subtracted from the signal spectrum, resulting in the alpha signal. This procedure was effective because the spectral dependence of the bremsstrahlung background was insensitive to modest variations in plasma parameters between the signal and background discharges, and variations in the intensity of the bremsstrahlung background were compensated for by the normalization procedure. Alpha signal extraction was successfully performed with both DT and D background discharges, although DT background discharges usually yielded better results because the fluorescence of the optical fibrer due to gamma radiation, which was typically 10–20% of the bremsstrahlung background at the end of beam injection, was present in the background signal and was therefore corrected by the subtraction procedure.

The most reliable extraction of the non-thermal alpha signal was obtained for measurements during a D-beam-only phase following the end of the DT beam period of the discharge. There were three reasons for this:

(a) The bremsstrahlung background was significantly lower during the lower power D-beam-only phase due to the electron density drop when the T beams were turned off.
(b) Beam penetration was better due to the lower plasma density.
(c) The contribution of fibre fluorescence rapidly became negligible after beam turn-off and could be neglected, simplifying the signal extraction.

A correction for the contribution of fibre fluorescence to the signal was successfully used at times immediately following the end of the T beams, but it introduced an additional uncertainty in the extracted signal. Note that, as a result of the long alpha slowing down time of 0.3–0.5 s in TFTR DT discharges, measurements of the lower energy alphas observed by α-CHERS made immediately after the main DT beam period of the discharge are representative of the alphas during the DT phase.

4.2. Confined alpha slowing down and transport

The first α-CHERS measurement of a non-thermal DT alpha spectrum is shown in Fig. 21 [98]. The discharge was a DT supershot [99] with $R = 2.52$ m, $a = 0.87$ m, $I = 2.0$ MA and $B = 5.1$ T. The total beam power was $P_{NBI} \sim 22$ MW during the main DT heating phase, which lasted 1.3 s; the D beams, including those viewed by α-CHERS, were kept on for an additional 0.7 s at a power level of $\sim$12 MW. The spectrum shown in Fig. 21 corresponds to $r/a \approx 0.3$ and the signal was averaged over 0.4 s (4.3–4.7 s) of the D-beam-only phase. At this point the alpha slowing down time was $\approx$0.5 s and the pitch angle scattering time was $\approx$20 s at the time of the measurements.

The spectrum was modelled using the TRANSP code [19] predictions of the alpha distribution function at 4.5 s and $r/a = 0.3$ for this discharge, beam atom densities calculated by a beam attenuation code [100], and cascade corrected line excitation cross-sections [101]. The model included three sources of signal: direct alpha-beam–atom charge exchange, charge exchange between alphas and halo thermal neutrals created by atom-deuterium charge exchange, and electron impact and ion impact excitation of alpha plume He$^+$ ions. The alpha plume He$^+$ ions were created by charge exchange with the neutral beam atoms primarily outside the line of sight, and could follow field lines into the spectrometer lines of sight. Figure 21 shows that direct alpha-beam–
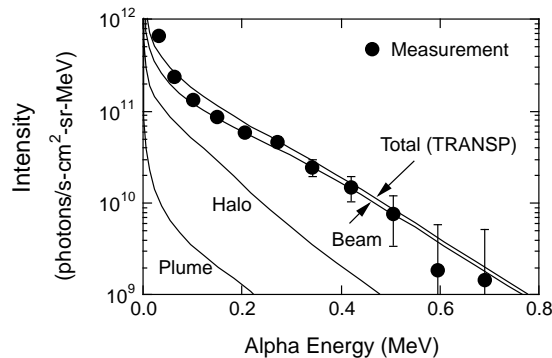

Figure 21. α-CHERS spectrum at $r/a \approx 0.3$ in a DT supershot averaged over 0.4 s: measured spectrum, solid circles; calculated spectrum, solid curves. Contributions from beam–neutral charge exchange halo neutral charge exchange and alpha plume ions are shown. The absolutely calibrated experimental signals and TRANSP calculations are shown on the vertical axis.

atom charge exchange was the dominant source of signal, but that halo atom charge exchange contributed significantly to the signal at alpha energies below approximately 0.2 MeV. The contribution of plume ion emission to the signal was negligible at all alpha energies because the alpha density was small at the large radii which are connected by field lines to the α-CHERS observation radii.

Agreement between the measured and calculated signals is quite good, indicating that the measured alpha energy distribution was close to the TRANSP prediction, which assumed classical slowing down, neoclassical alpha transport and stochastic magnetic field ripple effects. There was no normalization of the measured and predicted spectra in Fig. 21. The absolute intensity of the predicted signal, as well as its energy dependence, is quite sensitive to the slowing down time and radial transport of the alphas. Thus, the good agreement between the measured and predicted signals is strong evidence that the TRANSP model accurately described the behaviour of the class of alphas observed by α-CHERS. Examination of the relative contributions of passing and trapped alphas to the α-CHERS signal in this and other similar cases showed that the signal was dominated by passing alphas, but that trapped alphas contributed 1/4–1/3 of the total signal. Further evidence for classical slowing down is seen in Fig. 22, which shows the time evolution of measured and predicted α-CHERS signals at $r/a \approx 0.3$ from the same experiment as in Fig. 21 integrated over successive 0.1 s periods. Agreement between the measured and predicted spectra is good, and the effect of the contraction of the alpha distribution function to low energies at this late time in the discharge is clearly seen, providing additional evidence that classical slowing down accurately describes the alpha behaviour.

Following these initial measurements at a single radial location, five point radial profiles of the non-thermal alpha signal were measured in similar supershot discharges in two experiments [97] in which R, a, I and B were the same as for the measurements shown in Figs 21 and 22. A result from this alpha particle radial profile measurement is shown in Fig. 23. As before, the observations were made during a D-beam-only phase following the main DT beam heating phase. In the case shown in Fig. 23, the D beams were left on for an additional 0.7 s following the turn-off of the T beams. The D beam power was $\approx$20 MW during this observation phase, comparable to the power of $\approx$22 MW during the DT phase, to prevent the occurrence of sawteeth caused by a
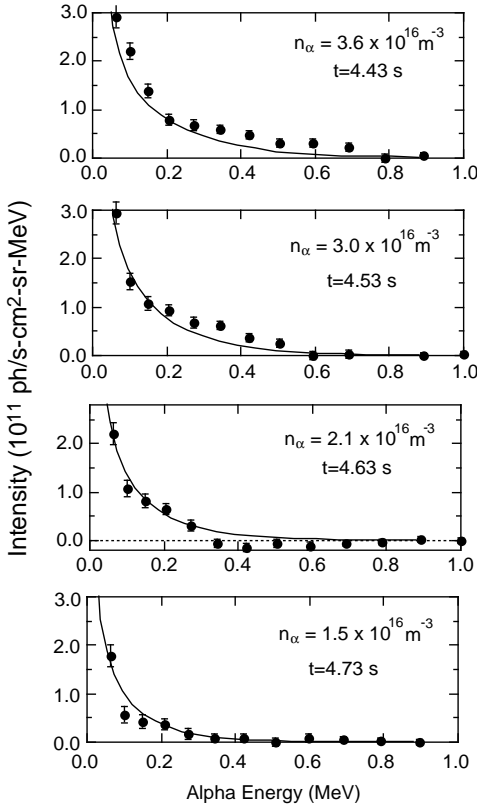
Figure 22. Time evolution of measured (solid circles) and calculated (solid curves) α-CHERS spectra averaged over 0.1 s in the same discharge as that for Fig. 21. The T NBI was turned off at 4.1 s, so these distributions show the thermalization of the alpha distribution after the alpha source has been largely turned off.

Figure 23. Radial profile of α-CHERS signals averaged over 0.15–0.6 MeV in DT supershot discharges (solid circles). The shaded bands show calculated signals based on the TRANSP code calculations of the alpha distribution function for assumed anomalous diffusivities of $D_{\alpha,anom} = 0$ (neoclassical transport only), 0.03 and $0.1~\mathrm{m}^2/\mathrm{s}$.

large drop in beam power following the turn-off of the T beams. In the second experiment, the measurements were made earlier in the D-beam-only phase at a somewhat lower beam power of ≈ 15 MW. The results of these two experiments were similar [97] so only the first one will be discussed in detail here.

The measured signals at each radius were averaged over alpha energies of 0.15–0.6 MW to improve the statistics. The lower end of this range was chosen so as to exclude contributions from thermal alphas, and the upper end was the highest observable alpha energy in these discharges. The error bars shown on the measurements in Fig. 23 were based on the one standard deviation statistical uncertainty of the signals and estimates of the systematic uncertainty in the alpha signal extraction process.
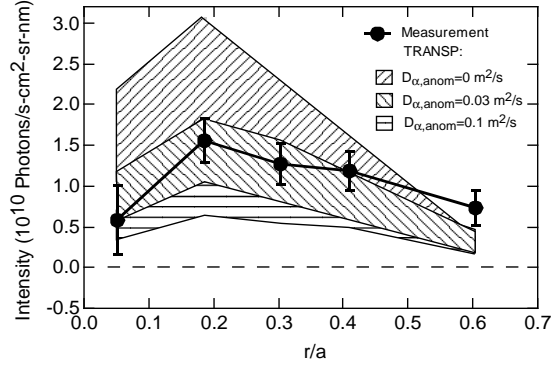
The calculated signals shown in Fig. 23 were based on TRANSP calculations of the alpha distribution function at each radius, as described above. The calculated signals are shown as one standard deviation uncertainty bands. The uncertainties were based on the combined uncertainties of the neutral beam stopping cross-sections, cascade corrected line excitation cross-sections, and the TRANSP calculation of the alpha distribution. In order to set an upper bound on any anomalous radial diffusion of the alphas that could be present, the TRANSP simulations were also performed with an anomalous radial diffusivity in addition to the collisional neoclassical transport included in the basic TRANSP model. This anomalous diffusivity, $D_{\alpha,anom}$, was assumed to be radially constant. In addition to the base case with $D_{\alpha,anom} = 0$, simulations were also performed with $D_{\alpha,anom}$ values of 0.03 and $0.10~\mathrm{m}^2/\mathrm{s}$. The calculated signals were integrated over the same alpha energy range, 0.15–0.6 MeV as for the measurements. Again, there is no normalization between the measured and calculated signals in Fig. 23.

In Fig. 23, the best agreement between the measured and calculated signals is seen for $D_{anom} = 0.03~\mathrm{m}^2/\mathrm{s}$, although the $D_{\alpha,anom} = 0$ prediction generally falls within the error bars on the measurements. Overall, the two measurements of the alpha signal radial profiles, combined with their uncertainties and those in the calculated signals are consistent with values of $D_{\alpha,anom}$ in the range 0–$0.1~\mathrm{m}^2/\mathrm{s}$, with the lower values $D_{\alpha,anom} \leq 0.03~\mathrm{m}^2/\mathrm{s}$

being most likely. For comparison, the neoclassical alpha particle diffusivity was in the range 0.01–0.05 m^2/s, depending on alpha energy and radial location. Similar results were also obtained in DT plasmas using the PCX diagnostic, which measured only deeply trapped alphas (see Fig. 16). These values are 1 to 2 orders of magnitude smaller than the ion thermal diffusivities in these discharges and indicate excellent energetic alpha confinement. The residual level of anomalous diffusion, if any, is most likely due to incomplete averaging of the large gyro-radius alphas over small scale turbulence, as discussed in Section 8.1.

4.3. Observation of non-thermal alpha redistribution due to sawteeth

Early α-CHERS measurements [98] showed evidence of weaker signals following sawtooth crashes, indicating that sawteeth cause redistribution of non-thermal confined alphas. To investigate this in more detail, an experiment was performed to make α-CHERS measurements of the radial profiles of the alpha density before and after sawtooth crashes [102].

The experiment was performed in DT supershot discharges with the same plasma parameters as those described in Section 4.2. The time evolution of the injected neutral beam power, neutron source strength and core electron temperature, $T_e(0)$, are shown in Fig. 24. Five deuterium and three tritium beams were injected at energies of 100 keV for a period of 1.3 s to establish a nearly steady state alpha population in the intermediate energy range observed by α-CHERS. The 95 keV deuterium beams viewed by α-CHERS were injected for an additional 0.7 s period, during which the alpha density radial profile was measured.

Sawteeth did not normally occur during the beam injection phase of supershots, so it was necessary to induce them by dropping the beam power 0.2 s after the end of the DT beam phase, as seen in Fig. 24(a). This caused the plasma β to drop below the level required to suppress sawteeth, and a sawtooth usually occurred within 0.25 s of the beam power drop, about halfway through the α-CHERS observation period. As seen in Fig. 24(c), there was only one sawtooth before the end of beam injection. By inducing the sawtooth in this way, the alpha density profile could be measured before and after the sawtooth crash. The alpha density profiles were obtained by combining data from two similar discharges of this
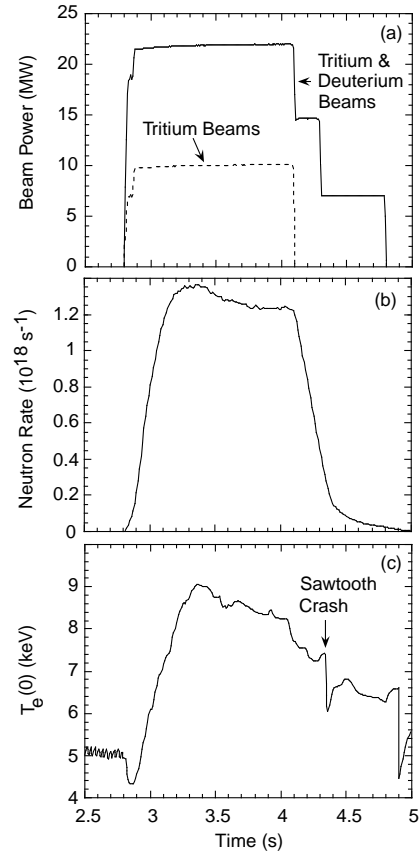

Figure 24. Plasma parameters for α-CHERS measurements of sawtooth redistribution of alphas: (a) neutral beam power, (b) neutron rate and (c) $T_e(0)$. The sawtooth crash occurs just after the end of the T NBI at 4.3 s.

type. The sawteeth were similar in both discharges, with $T_e(0) = 7.3$ keV and $n_e(0) = 5.0 \times 10^{19}$ m^{-3} before the sawtooth crash, and $\Delta T_e(0) = 1.5$ keV and $\Delta n_e(0) = 1.0 \times 10^{19}$ m^{-3} at the sawtooth crash.

The measured alpha spectra were modelled from TRANSP code predictions of the alpha distribution function at each time and radial point in these specific discharges as described above. For the purpose of comparison with the sawtooth model, it was desirable to deduce alpha densities from the measured spectra. To do this, the measured and predicted spectra and TRANSP alpha density at each time and radial point were integrated over the 0.15–0.6 MeV alpha energy range to improve statistics, and the integrated TRANSP alpha density was then normalized by the ratio of the measured alpha spectral signal to the predicted alpha signal. This process was

appropriate because the shape of the measured alpha spectrum did not change within the noise on the signal during the sawtooth crash, and it was therefore just a direct normalization of the measured and predicted signals to obtain a measured alpha density.

The alpha density profiles measured at one time before the sawtooth crash (t_1) and at two times after it (t_2 and t_3) are shown in Fig. 25(a); the integration time was 0.2 s. The sawtooth crash occurred early in the t_2 time period. Several features of the effect of the sawtooth crash on the alpha density are clearly seen in Fig. 25(a). There was a sharp drop in the core alpha density following the sawtooth crash, followed by partial recovery approximately 0.2 s later. Full recovery of the alpha signal was not expected because the source of 3.5 MeV alphas dropped strongly at the end of DT beam injection, well before the sawtooth crash. Electron cyclotron emission (ECE) measurements of the T_e profile as a function of time yielded an inversion radius of $r/a = 0.25$ during this sawtooth crash, which is consistent with the point at which the profiles t_1 and t_2 in Fig. 25(a) cross. There was a small increase in the alpha density at $r/a = 0.3$, which was just outside the inversion radius, although it was comparable to the size of the error bars. A large increase was not expected due to the long integration time of the measurements, since particles from the volume inside the inversion radius were displaced to a much larger volume outside it and the effect of post-crash radial diffusion is significant, as discussed below. There was no significant change in the alpha density at the two outermost radii. The lost alpha detectors showed no expulsion of alphas from the plasma during this sawtooth crash, indicating internal redistribution only.

The observed changes in the alpha density profiles shown in Fig. 25(a) were simulated with the sawtooth model of Kolesnichenko et al. [103]. This model is based on a Kadomtsev-like [104] rigid shift of the core plasma due to a $m = n = 1$ kink instability combined with a quasi-interchange influx of external plasma to the core, as in the Wesson model [105]. This is expressed through conservation equations for particles, energy and magnetic flux, and, unlike the Kadomtsev model, it allows $q(0) < 1$ following the crash due to the existence of two reconnection layers. Finite orbit width effects were not included in this model but were estimated to be small for the lower energy, predominantly co-going passing alphas observed by α-CHERS [102].

The post-crash alpha density profile was predicted by a transformation of the measured pre-crash profile
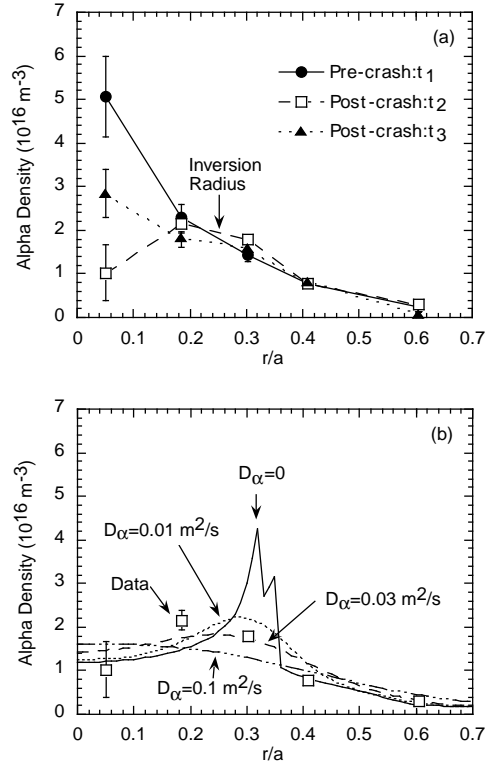

Figure 25. (a) α-CHERS measurements of alpha density profiles before sawtooth crash (t_1) and at two times after the sawtooth crash (t_2 and t_3). (b) Measured post-crash alpha density profile at time t_2 compared with model profiles assuming various values of alpha diffusivity.

based on input q profiles before and after the sawtooth crash. Measurements of the q profile were not available in these discharges, so q profiles similar to those measured before and after sawtooth crashes in other TFTR discharges were used [106]. The plasma redistribution was most sensitive to the values of the radius of the $q = 1$ surface, rs, and the mixing radius, r_{mix}, and it was relatively insensitive to the detailed shape of the q profile. The q profile parameters used before the crash were $q(0) = 0.87$, $r_s/a = 0.25$ and $r_{mix}/a = \sqrt{2} \times r_s/a = 0.35$, and after the crash: $q(0) = 0.90$ and $r_s/a = 0.24$. These values of r_{mix}/a and r_s/a were consistent with ECE T_e profile measurements.

Figure 25(b) shows the results of this model overlaid on the measured post-crash alpha density profile from the second time point in Fig. 25(a), t_2. The four model curves correspond to different assumed values of the alpha radial diffusion coefficient, D_α, in the

range 0–0.1 m^2/s. The radial diffusion was allowed to act for 0.2 s, corresponding to the signal integration time. The role of D_α was to simulate the radial motion of the alphas during the integration period following the sawtooth crash. This integration period was long compared with the timescale of the sawtooth crash itself, and significant radial motion of the alphas could occur during this time; thus, simulation of this effect was required for comparison with the measurements. It is clear from Fig. 25(b) that the observed large drop in the core alpha density was reproduced well by all values of D_α in this range, but that the relatively small increase in the alpha density outside the inversion radius was reproduced best by $D_\alpha = 0.03$ m^2/s. This value is in the range of values for the neoclassical diffusion coefficient in these discharges, as discussed in Section 4.2.1, and it is consistent with the observed upper limit on anomalous radial diffusion of $D_{\alpha,anom} = 0$–0.03 m^2/s.

4.4. Summary and directions for future work

The experiments performed with the α-CHERS diagnostic on TFTR were the first charge exchange recombination spectroscopy measurements in a tokamak plasma of non-thermal, confined alpha particles produced by DT fusion reactions. It is remarkable that these measurements could be made, given the difficulty of observing the weak alpha signal in the presence of the much brighter bremsstrahlung background. The α-CHERS measurements showed that confined alpha behaviour in supershot plasmas was well described by classical slowing down and neoclassical transport, and that sawteeth caused significant redistribution of confined alphas, in agreement with theory.

Despite these successful measurements, there were limitations to the α-CHERS technique on TFTR [107]. It is useful to briefly discuss these limitations with possible future use of this diagnostic technique in mind. One limitation of the TFTR α-CHERS measurements was that the low energy (50 keV/amu) D heating neutral beams estricted the maximum alpha energy that could be observed to approximately 0.7 MeV. Higher energy beams would allow higher energy alphas to be observed; in principle, alphas with energies up to the 3.5 MeV birth energy could be observed with an ∼880 keV/amu beam. However, high beam intensity would be required to observe the high energy alpha signal against the bremsstrahlung background because the alpha density, and thus the α-CHERS signal, decreases with increasing alpha energy. As a result, the maximum alpha energy observable using such a beam would be determined by the ability to extract the weak signal from the bremsstrahlung background.

Another limitation was that it was difficult to reliably measure the alpha signal during the DT heating phase of TFTR discharges because the bremsstrahlung background was high, which increased the noise on the alpha signal, and fibre fluorescence was a significant contribution to the signal. The best way of making reliable measurements during the DT phase of the discharge would be to modulate the beams observed by α-CHERS during this period. This would allow accurate correction for both the bremsstrahlung background and the fibre fluorescence. Such an experiment was planned for the final TFTR run, but was not performed due to lack of time.

In general, useful α-CHERS data were only obtained from dedicated experiments where the timing and species selection for each beam could be tailored to the needs of α-CHERS measurements. As a result, α-CHERS measurements were not made in the interesting reversed shear and enhanced reverse shear regimes due to lack of time in the two final TFTR runs. Making such measurements would certainly be a high priority in any future α-CHERS measurements on other tokamaks. Clearly, a modulated diagnostic neutral beam that can be controlled independently of the main heating beams is required for routine α-CHERS measurements.

Finally, it is worthwhile to briefly speculate [107] on the possibility of making α-CHERS measurements on a future DT reactor such as ITER. Given the high radiation levels in the vicinity of ITER, the viewing optics and light transmission system would have to be designed to eliminate fluorescence and transmission losses due to radiation [108]. This would require the use of high throughput reflective optics to bring the light to a shielded area where optical fibres could be used. This would be difficult but not impossible. Assuming this could be done, the primary issues are beam penetration in the large, dense ITER plasma and extraction of the small alpha signal from the intense bremsstrahlung background. This situation is helped to some extent by the higher alpha density in ITER compared with that in TFTR. Calculations of the expected α-CHERS signals in ITER show that a 5 MW, 200 keV/amu beam focused to 0.1 m height in the plasma core would allow α-CHERS measurements at signal to noise ratios

similar to those achieved on TFTR. Integration times of several seconds would be required. Such a beam would permit measurements over a range of alpha energies similar to that observed on TFTR; going to higher beam energy would not significantly increase this range because the alpha density drops faster with increasing alpha energy than the increase in beam penetration achieved by a higher energy beam.

However, the α-CHERS signal in ITER would be 10^{-5}–10^{-6} times the bremsstrahlung background, while this ratio was 10^{-2}–10^{-3} in TFTR. Thus, the primary difficulty in making α-CHERS measurements on ITER is that a major advance in the ability to extract the weak alpha signal from the bremsstrahlung background would be needed. Rapid modulation of the neutral beam would aid the signal extraction process, but it is not clear at this point whether or not it would be sufficient to overcome fluctuations in the bremsstrahlung background to allow the α-CHERS signal to be clearly observed. Use of a short pulse, intense neutral source would help resolve this problem, but it is still not clear whether α-CHERS measurements would be possible in a reactor such as ITER.

5. Alpha particle heating and alpha ash buildup

The alpha particle densities in TFTR were up to 0.3% of the total plasma ion density, a fraction similar to that expected in a reactor (Table 1). Since the alpha particle birth energy is typically 2 orders of magnitude higher than the temperature of the DT fuel ions, they slow down predominantly on electrons. The direct observations, discussed earlier in this review, of well confined alpha particles which slow classically in TFTR DT plasmas, motivated experiments to look for direct evidence for core alpha particle heating of electrons. These experiments, discussed in Section 5.1, yielded the first evidence for self-heating of a tokamak plasma [109].

DT operation on TFTR also provided the first opportunity to observe the helium ash which arises from thermalizing the fusion generated alpha particles. This is important since the accumulation of helium ash in the core of a DT reactor can quench thermonuclear ignition. Although the fusion power in TFTR DT plasmas was relatively low by reactor standards, typically about 5 MW, the on-axis source of helium ash from alpha particle slowing was comparable to that expected for a reactor (Table 1).

Also, although TFTR did not have a reactor relevant helium pumping scheme, the TFTR carbon limiter has been shown to effectively pump helium and other noble gases. This situation enabled the first study of a reactor-like helium ash environment in a DT tokamak plasma [110]. These experiments, discussed in Section 5.2, showed that the helium ash confinement was compatible with sustained ignition in a reactor, and that the ash confinement is dominated by edge pumping rather than core transport.

5.1. Alpha particle heating

Alpha particle heating of electrons in TFTR DT discharges accounted for only about 5% of the global power flow to electrons. However, in the plasma core ($r/a \leq 0.25$) the electron heating fraction reached 15%, as deduced from TRANSP simulations. A systematic study to look for differences in the electron temperature profile was performed for TFTR DT neutral beam heated plasmas, and for comparable D-only and T-only discharges.

Although the central electron temperature, $T_e(0)$, in the DT plasmas was found to be systematically higher than in the D or T plasmas, attempts to observe clear evidence for alpha particle heating by comparing the $T_e(0)$ rise in D and DT plasmas were challenged by several factors. First, there was a reduction in the direct beam heating of electrons in going from D to T neutral beam injection at the same neutral beam injection power, and there were uncertainties in calculating the neutral beam deposition profile. Second, an apparent dependence of the energy confinement on the mixture of hydrogenic isotopes was observed in TFTR [111–114], and this contributed to the rise in $T_e(0)$ in going from D to DT. Finally, inherent performance variations due to MHD instabilities and limiter conditioning resulted in $T_e(0)$ changes which competed with the rise in $T_e(0)$ due to alpha particle heating. For high performance discharges, with similar beam heating powers and plasma operating parameters, TRANSP modelling [114] indicated that approximately half of the 2 keV $T_e(0)$ difference between DT and D plasmas could be attributed to alpha particle heating.

In order to demonstrate the presence of alpha particle heating, it was necessary to show that there is an additional $T_e(0)$ rise in DT plasmas which is not measured in similar D or T plasmas. Experiments specifically to study alpha particle heating were performed in TFTR, but these studies were frustrated by significant D recycling from the C limiter tiles

[99]. As a result of this D influx, the discharges which were nominally only fuelled by T neutral beams had a significant level of DT fusion power production and hence alpha particle heating (i.e. about 1/3–2/3 of the fusion power of a plasma with an optimum species mix).

An alternative approach was to utilize the considerable database of existing plasmas from the TFTR DT campaign and to look for statistically significant systematic trends which supported the existence of core alpha particle heating of electrons. In order to broaden the number of discharges included in the database, plasmas with a wide range of wall conditioning and level of MHD activity were added. In the study, it was assumed that these variations in plasma conditions were expressed through variations in τ_E. An empirical study of $T_e(0)$ scaling in 380 TFTR D beam fuelled plasmas from the 1990 TFTR experimental campaign [115] had exhibited a clear dependence of $T_e(0)$ on global energy confinement time τ_E, with $T_e(0) \sim \tau_E^{0.5}$ under otherwise fixed conditions. The 1990 database also showed a significant dependence on toroidal magnetic field and the average neutral beam energy. There was, however, no significant dependence on injected neutral beam power in the 1990 database, and this was probably the result of choosing to use data from plasmas with no less than 15 MW of neutral beam heating power. The empirical scaling of $T_e(0)$ with τ_E was used to compensate for the variations in $T_e(0)$ due to changes in plasma conditioning and MHD activity.

All the discharges from the 1993–1995 TFTR DT campaigns were examined, and the cases with the largest number of DT and T plasmas within a narrow range of toroidal magnetic field and average neutral beam voltage were identified. The resulting database included $R = 2.52 \pm 0.01$ m major radius plasmas with toroidal fields of $B = 4.85$–5 T and average neutral beam voltages of 98–107 kV. Neutral beam power in the database ranged from 15 to 34 MW. There were 67 D beam heated plasmas, and 22 DT beam heated plasmas with about 60% of the beam power in tritium and fusion powers, P_{fus}, up to 7.5 MW. There were also four T beam heated plasmas with fusion powers of about 2 MW, due to D recycling from the C limiter. The plasma parameters in the database were evaluated 0.7 s into the neutral beam heating pulse, which was late enough for the alpha particle population to build up, but early enough to avoid 'rollover' of plasma performance or turn-off of the heating beams. Plasmas with sawteeth or significant impurity influxes

(from the start of beam injection until the time of interest) were removed from the database. The evolution of the electron temperature profile was obtained from ECE spectrometry [116, 117]. In this study, electron temperature data from Thomson scattering was not included since it was unavailable for many of the plasmas in the database.

Figure 26 shows a plot of $T_e(0)$ versus τ_E for the constrained TFTR database. The empirical scaling for $T_e(0)$ obtained from the 1990 TFTR D plasmas is shown by the shaded region. The width of this region indicates the standard deviation in the scaling. Most of the DT discharges (open circles and triangles) lie on or slightly above the 1990 empirical scaling. It should be noted that the 1990 empirical scaling was derived from plasmas with a major radius of 2.45 m, somewhat smaller than the discharges in the present study. The DT plasmas with $P_{fus} < 6$ MW (solid circles) on average deviate further from the 1990 scaling, and the DT plasmas with $P_{fus} > 6$ MW (shaded circles) show the greatest deviation from the empirical scaling. Since DT plasmas with the highest P_{fus} attain a much higher $T_e(0)$ than D plasmas with similar energy confinement times, it was concluded that heating by alpha particles was the most likely explanation for the rise in $T_e(0)$.

Further evidence for alpha heating was found when the time evolution and the radial profile of the electron temperature were compared between sets of D and DT plasmas with closely matched neutral beam power and τ_E. The time evolution of the incremental electron temperature rise was similar to
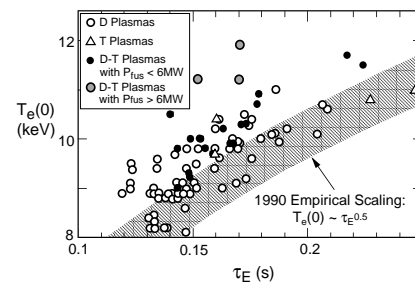
Figure 26. Central electron temperature 0.7 s after the start of neutral beam injection versus the global plasma confinement time for D, DT and T plasmas with major radii of 2.52 ± 0.01 m, toroidal field of 4.85–5 T, neutral beam power of 15–34 MW and beam voltage of 98–107 kV. The empirical scaling for $T_e(0)$ obtained from the 1990 TFTR D plasmas with major radii of 2.45 m is shown by the shaded region, the width of which indicates the standard deviation in the 1990 scaling.

that predicted by the TRANSP time dependent analysis code [18, 19], assuming only classical alpha particle orbit losses. The electron temperature rise due to alpha particle heating was determined by turning the alpha heating on or off in the TRANSP code, and by using a thermal diffusivity from either one of the D or one of the DT discharges from the ensemble of plasmas used for the comparison. This resulted in a range of uncertainty in the predicted temperature rise due to alpha particle heating which was typically ±50% of the measured temperature rise.

Figure 27(a) shows an overlay of the average electron temperature profiles for the sets of D and DT plasmas at a time 0.6 s after the start of neutral beam heating [109]. The temperature difference, as shown in Fig. 27(b), is localized to a region within 0.3 m of the magnetic axis. The magnitude and localization of the temperature rise is consistent with that predicted for alpha particle heating of electrons by the TRANSP analysis code. The localization of the temperature increase in the DT plasmas relative to the D plasmas is consistent with the source profile of DT fusion-generated neutrons, as measured by a multichannel neutron collimator [118] and shown in Fig. 27(c). The profile shape of the alpha particle density and heating are computed to be close to the DT fusion reaction source.

In summary, the electron temperature increase in the DT plasmas relative to the D discharges is primarily in the core region where the alpha particles are born and are expected to provide heating. Because the DT plasmas in the TFTR study had fusion powers which were less than one quarter of the total heating power, the power flow to the core electrons was dominated by beam heating and thermal ion-electron coupling. However, for the plasmas with the highest fusion power in the database, alpha particle heating accounts for about 15% of the electron power flow within $r/a = 0.25$, while ohmic heating accounts for less than 2% of the power flow within $r/a = 0.25$ in these discharges.

There are two complications with the alpha heating study on TFTR in addition to those discussed earlier. First, although Thomson scattering electron temperature profile data were available for most of the shots in the database, it was only available at one time and generally that time was either too early in the neutral beam heating pulse or after a major MHD event. There has been a long standing, unresolved, disagreement between ECE and Thomson scattering measurements of the electron temperature profile on TFTR [119]. Second, the
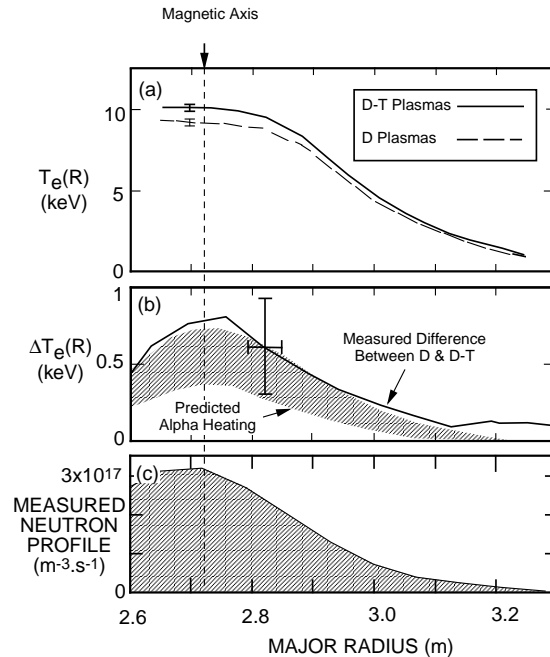

Figure 27. (a) Electron temperature profiles versus major radius 0.6 s after the start of neutral beam injection for six DT plasmas with $\tau_E = 0.155$ s, $P_{fus} = 4.5$ MW and $P_{NBI} = 24.2$ MW (solid line), and seventeen D plasmas with global energy confinement time $\tau_E = 0.15$ s and $P_{NBI} = 24.7$ MW (dashed line). (b) Electron temperature difference between the DT plasmas and the D plasmas of panel (a) versus major radius, compared with the predicted temperature increase due to alpha heating from the time dependent kinetic code, TRANSP (shaded region). (c) Measured neutron emission source profile measured by a multichannel neutron collimator for the DT plasmas in panel (a), which should be similar to the alpha heating profile.

temperature rise due to the isotope effect in TFTR was comparable to the rise due to alpha heating. This can be resolved by an experiment which includes plasmas at higher fusion power and T plasmas with much reduced D recycling. Such an experiment has recently been performed on the JET tokamak [120] in which alpha heating was unambiguously observed and the effects of alpha heating and any potential isotopic dependence of the energy confinement time were successfully separated. This JET experiment was strongly influenced by the TFTR result. A scan of DT concentration was employed to separate the effects of alpha heating and any isotopic

dependence of the energy confinement. In contrast to the experiments on TFTR, no isotopic dependence was found within measurement uncertainties, so that the observed increase in $T_e(0)$, 1.3 ± 0.23 keV in 12.2 keV, was determined to be due entirely to alpha particle heating. Further, the measured alpha particle heating was determined to be as effective as heating by an energetic RF driven hydrogen minority tail in JET.

5.2. Alpha ash buildup and transport

Helium ash studies in TFTR employed pairs of similar D and DT plasmas. Charge exchange recombination spectroscopy [121] was used to infer the thermal He density by observing the Doppler broadening emission from the 468.6 nm, $n = 4-3$ He^+ line, which was excited by charge exchange between D heating beam neutrals and He^{2+}. These were difficult and challenging measurements since C lines, excited by electron impact and charge exchange, had a similar wavelength and brightness.

Figure 28 shows the neutral beam heating pulse shape and timing in these experiments [110]. For both the D and DT discharges, 21–22 MW of neutral beam power was injected between 2.8 and 4.1 s, followed by a phase with only 12 MW of deuterium beam heating from 4.1 to 4.8 s. The DT plasmas had a flat-top fusion power of about 4.5 MW. Sawteeth were absent from the plasmas heated by D neutral beams, and no sawteeth were seen in the DT plasmas until 20 ms prior to the end of beam injection. The alpha particle slowing down time was calculated to be 0.5–0.7 s and the alpha particles continued to thermalize in the core throughout the lower power, D-only, heating period.

The measured neutron emission and the volume integrated thermal helium source due to the thermalizing confined alpha particles are also shown in Fig. 28. The thermal He source was calculated with the TRANSP code using measured plasma profiles and calculated beam deposition, alpha particle source and transport. Classical transport was assumed for the fast alpha particles until they reached an energy which was 1.5 times the local ion temperature. Below this energy the alphas were treated as helium ash, i.e. thermal helium. The measured helium diffusivity and convective velocity from an earlier He transport study [122] were used to model the He ash behaviour in these discharges. The TRANSP modelling implied that the helium ash source profile was similar to the TRANSP neutron
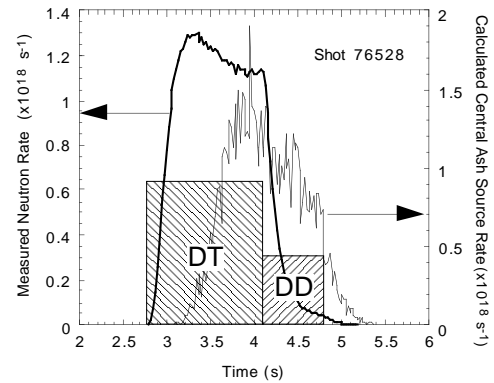

Figure 28. Measured total neutron rate versus time and the calculated rate at which alpha particles are joining the population of thermal particles in the DT plasma used for the He ash measurements. The shaded regions indicate the relative powers and duration of the two neutral beam heating phases.

emission profile since the energetic alpha particles were well confined.

The He ash profile was measured by taking the difference between the total beam induced line brightnesses observed in the D and DT plasmas just before beam turn-off, and subtracting the edge emission just after the beam turn-off. The ash profile was obtained by initially using a trial He density profile in a code which calculates the beam deposition, charge exchange emissivity, and parallel transport and emission of plume ions. The total He ash line brightness was calculated for each line of sight by calculating the toroidal and radial velocity distribution of the He^+ charge exchange products. The trial He ash profile was iterated until there was agreement between the measured and calculated beam induced brightness profiles.

Before alpha particles were expected to thermalize, i.e. at 3.45 s, there was no difference in the spectra in the D and DT plasmas, and the emission was predominantly from C. Later, the brightness of the thermal portion of the CHERS spectrum was observed to increase in the DT plasmas, relative to the D comparison plasmas. This increase was seen on all CHERS lines of sight and was shown not to be due to an increase in carbon, since the 529.2 nm C^{5+} line brightness in other similar discharge pairs was found to be the same within a few per cent throughout the pulse. Also, a change in C density that would result in this increased brightness would have increased the measured Z_{eff} deduced from the
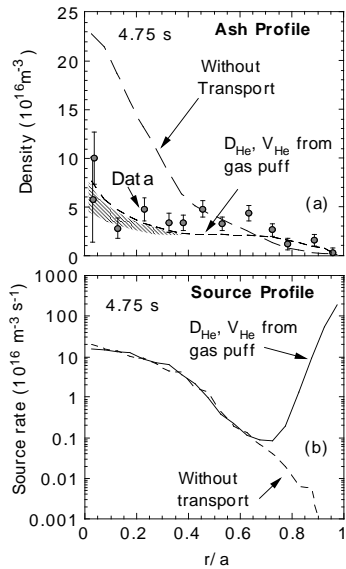
Figure 29. (a) Measured and modelled He ash profiles just prior to the end of beam injection in discharges like that for Fig. 28. The errors include uncertainties in the plume correction, beam attenuation, background emission subtraction, charge exchange emission rates, photon statistics and reproducibility of background C levels. The shaded region represents the difference between the profile shapes that are predicted with and without the central alpha source, but with transport in both cases. (b) Modelled total He ash source profiles with and without anomalous thermal He transport.

visible bremsstrahlung levels by about 0.3 and this was not observed.

The inferred He ash profile late in time is shown in Fig. 29 [110]. The relatively flat He ash profile and the total ash content at this time indicate that the He ash moves rapidly from the core to the edge and is subsequently recycled back to the plasma from the vessel wall, as expected for thermal He ions. If there were no radial transport of thermalized helium, the resulting profile would be much more peaked, as shown in Fig. 29(a), and there would be about twice as many ash particles as were measured. The lower edge of the shaded region in Fig. 29(a) shows the effect of turning off the central source in the code, which implies that the ash profile shape at late times was dominated by radial transport of thermalized helium. The alpha generated He ash resides in the vacuum vessel for 1.2 ± 0.4 s, or about 6–10 global energy confinement times, which is consistent with sustained ignition in a DT fusion reactor [123]. The

intrinsic He particle confinement time (i.e. excluding the effect of limiter recycling), is only about 0.3 s, so edge recycling, rather than core transport, dominate He ash removal, as illustrated in Fig. 29(b).

The time evolutions of the measured and modelled He ash content for two radii in this experiment are shown in Fig. 30 [110]. The modelled He ash time evolution indicates that both the classical alpha particle slowing-down calculation and the nominal anomalous thermal He transport assumptions in TRANSP are consistent with the measurements. The sensitivity of the modelling results to variations in the thermal diffusion and pinch terms is shown in Figs 30(a) and (c), and the sensitivity to the assumed alpha particle slowing down rate is shown in Figs 30(b) and (d). The time behaviour of the measured He ash implies an alpha slowing down time within a factor of 2 of the classical model, and the amplitude of the ash content is not consistent with the prompt loss and burial of any significant fraction of the fast alpha particles.

6. Alpha particle driven toroidal Alfvén eigenmodes in TFTR

It has long been known that MHD activity can enhance energetic particle loss, possibly leading to localized heating and damage to plasma facing components [124]. Instabilities collectively excited by large populations of resonant particles are considered to be particularly deleterious to energetic particle confinement. One instability with the potential for strong interaction with energetic alpha particles in a DT reactor is the TAE [125, 126]. These modes occur within toroidicity induced gaps in the shear Alfvén spectrum and have received considerable attention in recent years due to their low instability threshold and ability to resonate with alpha particles in a DT reactor [127].

Early theoretical analysis of the anticipated TFTR DT plasmas using the NOVA-K code suggested that alpha driven TAEs would be most unstable in a narrow time window following termination of neutral beam injection [126, 128], as illustrated in Fig. 31. The anticipated threshold for alpha driven TAE excitation was predicted to be as low as $\langle \beta_\alpha \rangle \approx 0.5 \times 10^{-4}$ for normal (positive) shear discharges with $q(0) < 1$ and $V_\alpha/V_A \approx 1$, which was well below the expected alpha pressure levels. The most unstable modes were calculated to be global low-n eigenfunctions occupying a large radial extent in the
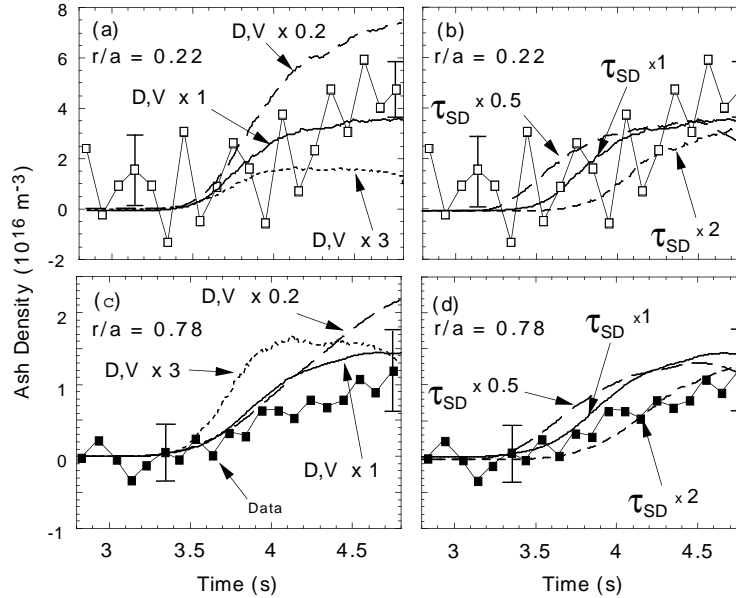
Figure 30. Measured He ash density versus time compared with modelling results based on TRANSP simulations of the alpha particle slowing down and subsequent transport and wall pumping of thermalized ash. Panels (a) and (b) show the effect of varying the assumed values of the anomalous thermal He transport rates and alpha particle slowing down times, respectively, at $r/a = 0.22$. Panels (c) and (d) are the same for $r/a = 0.78$. These results are most consistent with the assumption of classical alpha slowing down to within about a factor of 2 uncertainty.

outer region of the discharge at $r/a > 0.5$. The dominant stabilizing term for the TAE was considered to be thermal ion Landau damping, so that termination of neutral beam injection was expected to decrease this damping term relative to the alpha particle drive 100–300 ms following the end of beam injection.

6.1. Initial attempts to study alpha driven instabilities

The initial high powered DT experiments in TFTR did *not* show any evidence of alpha-driven TAEs, either during or after termination of neutral beam injection [99]. This absence of TAE activity during standard 'supershot' plasmas persisted through the TFTR DT run [44–46], including the highest fusion power discharges which reached up to $\beta_\alpha(0) \sim 0.3\%$, i.e. about 10 times the level of the initially expected theoretical threshold. The non-observation of TAEs in these DT plasmas in TFTR presented a significant challenge to theory. The

discrepancy between theoretical predictions of TAEs and the absence of TAE activity in the experiments led to specific attempts to excite alpha driven TAEs and to better understand the theory, which ultimately produced new predictions and motivated a successful experiment.

One experiment was motivated by the initial theoretical prediction that the dominant damping of TAE modes in high powered DT plasmas was due to thermal ion Landau damping. Helium gas puffs and Li pellet injection were used to transiently cool a standard supershot plasma with $\beta_\alpha(0) \sim 0.2\%$ to reduce ion Landau damping and excite TAEs [129]. Although the ion temperature clearly decreased before the alpha population thermalized, no TAEs were seen in the reflectometer, beam emission spectroscopy or magnetic diagnostics. Detailed analysis of these discharges using the NOVA-K code showed that the total TAE damping was greater than the total alpha drive for this experiment, as shown in Fig. 32. The dominant TAE damping was
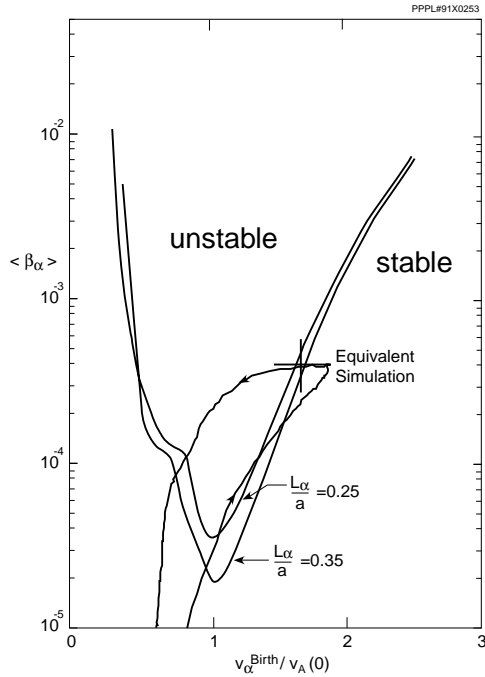
Figure 31. Original calculation of the boundary of the TAE instability region in the space of volume averaged β_α versus V_α/V_A. The β_α was assumed to decay exponentially in minor radius with a decay length of $L_\alpha/a = 0.25$ or 0.35. The trajectory in time of the TRANSP DT simulation is shown, with the large cross indicating the end of NBI.
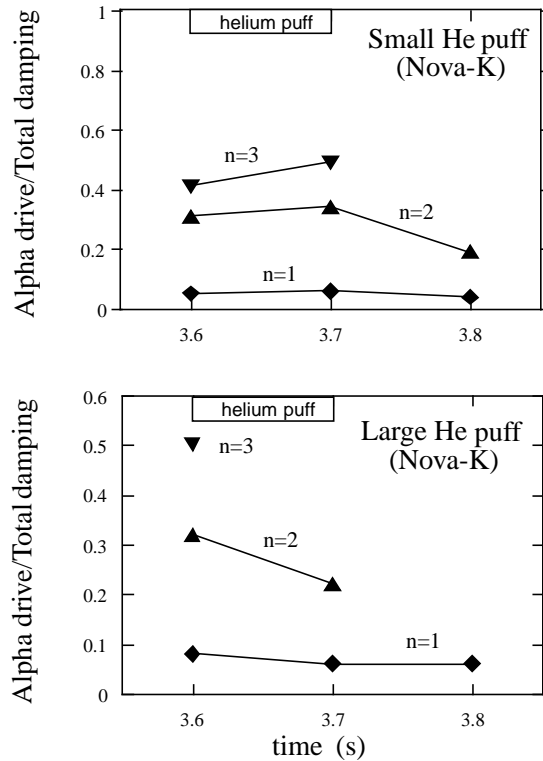

Figure 32. Ratio of the calculated alpha particle TAE drive divided by the total TAE damping for $n = 1\text{--}3$ modes for the small and large He puffs produced at $3.6 - -3.7$ s during DT supershots. This ratio was calculated to be ≤ 1 for all cases, implying TAEs should be stable, consistent with the experimental results of Fig. 32.

created by non-thermalized neutral beam ions with $V_{beam}/V_A \approx 1/3$, and not by thermal ions.

Another experiment was done to create TAEs in D discharges using an ICRH driven minority tail, and then to compare the ICRF power threshold for the TAE instability with similar DT discharges which had an additional alpha particle pressure drive [130]. A lower ICRH power threshold for TAEs was found for the DT discharges, as illustrated in Fig. 33, suggesting that the presence of alphas could have caused 10–30% of the total drive for TAEs in the DT discharges. However, it was difficult to isolate the possible effects of other differences between the D and DT discharges on the TAE damping processes, for example the effect of different beam species.

A third experiment to destabilize alpha driven Alfvén instabilities in TFTR DT discharges was made by creating high-β plasmas in low current discharges to find a 'β-induced Alfvén eigenmode' (BAE) [131], as previously observed in DIII-D using

neutral beam injection. This TFTR experiment created DT plasmas near the β limit with $\beta_\alpha(0) \sim 0.1\%$, but the observed MHD activity was common to both DT and D discharges, i.e. it was not significantly driven by alphas. It was estimated that the alpha drive was much smaller than the beam drive and nearly an order of magnitude less than needed for excitation of the BAE. This result was similar to that obtained from the analysis of the KBM activity observed in other high-β DT TFTR discharges [71], in which it was concluded that the alpha drive did not contribute significantly to the observed instability.

Finally, an experiment was made to decrease the alpha drive needed to destabilize TAEs by increasing the central $q(0)$, thereby better aligning the radial location of the alpha pressure gradient with the TAE location [132]. Discharges with $\beta_\alpha(0) \sim 0.1\%$ were
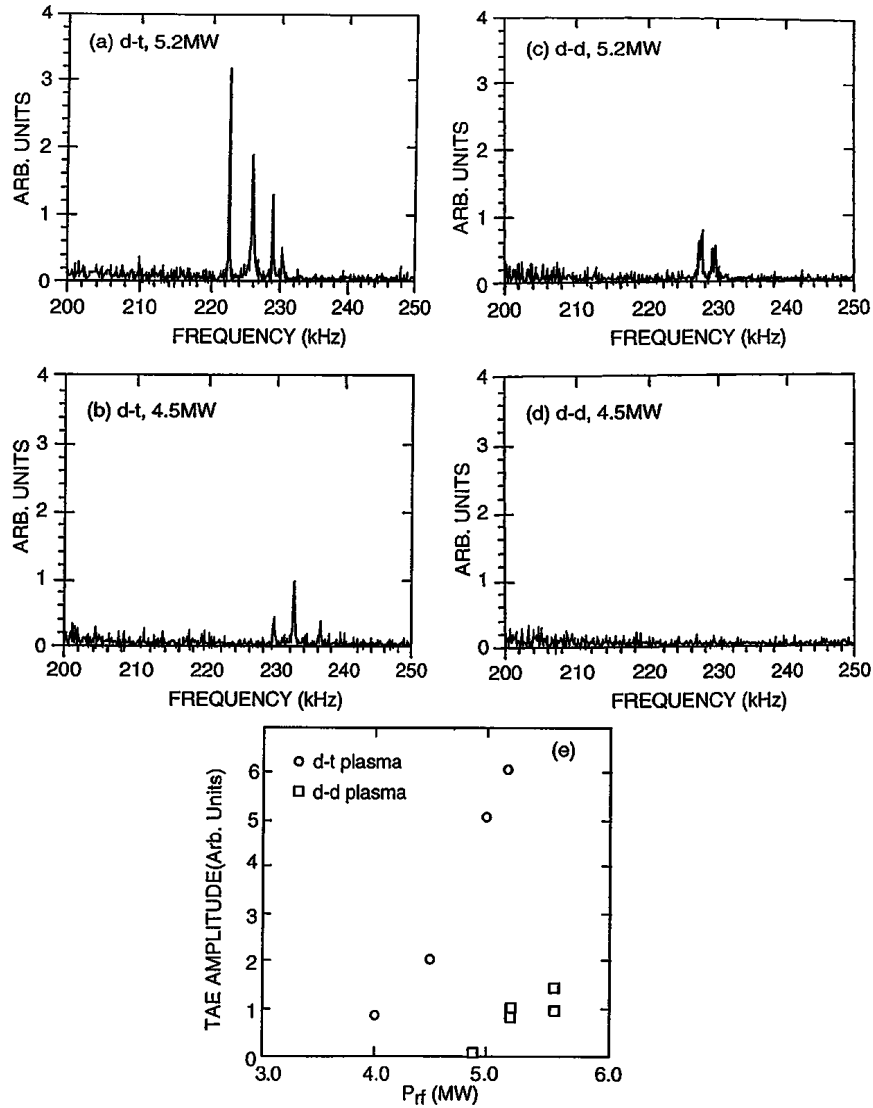
Figure 33. Variation of the edge magnetic fluctuations levels from TAEs generated mainly by ICRH hydrogen minority tail ions in DT versus DD discharges. The magnitude of these TAEs is larger in DT discharges compared with DD discharges at the same applied RF power, suggesting that alpha particles in the DT discharges are contributing to the drive for these TAEs.

created with $q(0) \approx 1.5$, with positive shear everywhere, but no signs of TAEs were observed. The theoretical analysis in Ref. [132] indicated that the TAEs were close to the instability threshold, but still not unstable when all of the damping mechanisms were included.

6.2. Theoretical developments concerning TAE instability

The net result of these early efforts was the sense that some other factors may be contributing to the stability of these modes, particularly in the afterglow

of DT plasmas when thermal and beam ion Landau damping were expected to be small. A number of seminal contributions to the theoretical understanding of TAEs quickly followed, which eventually lead to the first experimental observation of alpha driven TAEs.

First, a revised non-perturbative kinetic analysis of TAE damping on electrons revealed the surprising result that modes within the toroidicity induced gap could still be strongly damped by coupling to kinetic Alfvén waves (KAWs) [133]. It was proposed in the original work that this damping mechanism (called radiative damping) could account for the higher than expected damping rates observed in low toroidal field experiments where TAEs were excited with neutral beam ions. However the full significance of this work for alpha particle excited TAEs in TFTR plasmas was recognized only later with the second key discovery, that of core localized TAEs.

This second breakthrough was the recognition that a new form of TAE, the core localized mode, could exist in the central weak magnetic shear region of TFTR DT plasmas [134, 135]. Unlike the global TAEs which were previously expected to be unstable in the outer region ($r/a > 0.5$) of DT plasmas (as described in Section 6.1), the core modes were calculated to be unstable inside the half minor radius. These modes could occur in the steep gradient region of the alpha particle pressure, potentially lowering the threshold for exciting alpha particle driven TAEs provided radiative damping and ion Landau damping could be reduced. Detailed theoretical analysis revealed that reduced central magnetic shear near the central region of the discharge could dramatically lower radiative damping and hence significantly lower the critical β_α required for excitation of core localized modes. The anomalously high calculated TAE damping rates after the termination of neutral beam injection in DT plasmas were now recognized as being due to radiative damping, and the prescription for exciting these modes was to reduce the magnetic shear.

Finally, as noted at the end of Section 6.2, it was pointed out that elevating the central safety factor would allow low-n TAE resonances to move closer into the core of the discharge where they could sample more of the energetic alpha particle distribution [136, 137]. Lower toroidal mode numbers tend to have lower net damping rates provided the eigenfunction does not intersect the Alfvén continuum. The importance of this work is that the reduction of the central magnetic shear could only be achieved by

elevating the central safety factor in TFTR, so that reducing the magnetic shear also leads to lowering the toroidal mode numbers for core localized modes.

6.3. Experimental observations of alpha driven TAEs in TFTR DT plasmas

Motivated by these predictions for alpha driven TAEs under conditions of low beam ion Landau damping, weak magnetic shear and elevated central safety factor, an experiment was done which led to the first observation of purely alpha particle driven TAEs in TFTR [138]. Further investigations led to the first ever mapping of the internal structure of alpha driven TAEs, confirming their core localization and also revealing a significant anti-ballooning feature not predicted by theory [139].

In these experiments the central safety factor was raised above unity by use of fully grown plasmas during current rampup, similar to the startup used for reverse shear plasmas [46], but without neutral beam pre-heat. Alpha driven TAEs were then observed in a transient phase 100–300 ms following the end of DT neutral beam injection. Figure 34 shows $q(r)$ and β_α profiles 150 ms after neutral beam injection for a discharge in which relatively strong alpha driven TAE activity is observed. The central safety factor of $q(0) \approx 1.5$ was measured using the motional Stark effect (MSE) diagnostic and is consistent with the absence of sawteeth in these discharges [140].

A necessary criterion for these modes to be TAEs is that their frequency falls into the toroidicity induced gap in the shear Alfvén spectrum. Shown in Fig. 34 is the radial gap structure calculated using NOVA-K for the $n = 4$ mode. The gaps are all radially very well aligned and the measured mode frequency occurs inside the gap. The well aligned gap would in principle allow excitation of global TAEs. However, NOVA-K analysis indicated that the global TAEs occur in the outer half of the plasma where the alpha particle drive is very weak. Isolated core localized modes exist in the central region of the discharge which can be destabilized by the centrally peaked alpha particle β. The core localized gap at $r/a \approx 0.35$ resides in the region of weak central magnetic shear with a large radial separation to the next gap position at $r/a \approx 0.6$. Under these conditions, theory predicts the core TAEs (localized to the region around a single gap) will be most unstable in TFTR DT plasmas. In general, the observed mode frequencies fall within the gap width, for all except some $n = 1$ and $n = 2$ modes.
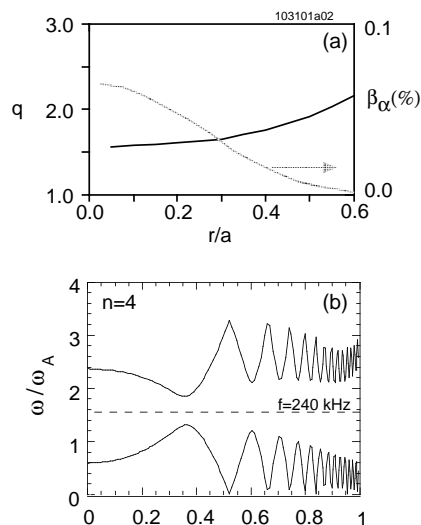
Figure 34. (a) Radial profiles of β_α and $q(r)$ at $\sim$ 150 ms following turn-off of neutral beam heating in a weak central shear discharge with alpha driven TAE activity. (b) Corresponding toroidicity induced $n = 4$ gap in the shear Alfvén spectrum at the time of observed $n = 4$ activity. The gap structure is radially well aligned and the mode frequency (marked by the dashed line) occurs in the gap, as expected for TAEs. The dominant uncertainty in the gap frequency arises from the uncertainty in the central safety factor obtained from MSE measurements ($\omega \sim V_A/qR$).

Figure 35 shows the time traces of the central β_α and plasma β as well as contours of magnetic fluctuations versus frequency and time in a DT plasma with $q(0) > 1$. Theory indicates that Landau damping (both thermal and beam ion) and radiative damping are dominant stabilizing terms during high power neutral beam injection, so that the only window for observing TAEs is in the narrow time slice following the end of beam injection as shown in Fig. 35. Typical D or T beam ion slowing down times are of the order of 80–100 ms, and the decay of the plasma β occurs on a similar timescale after termination of neutral beam injection as indicated by the trace of the central plasma β. However, energetic alpha particles have a slowing down time considerably longer (300–500 ms depending on the plasma conditions in the afterglow) as indicated by the β_α trace. Thus, one of the key factors in exciting TAEs in TFTR is the decay of the plasma β on a timescale short compared with the alpha particle slowing down time.
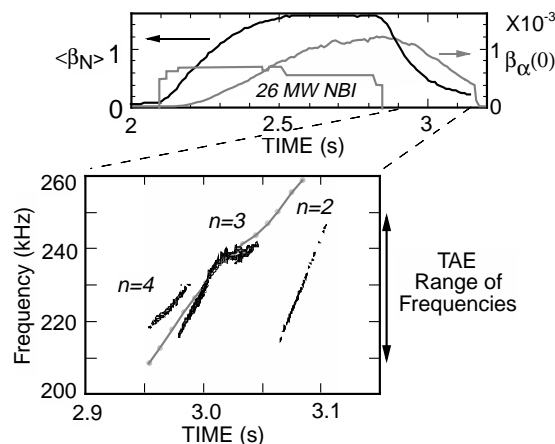

Figure 35. Evolution of DT neutral beam power, central $\beta_\alpha(0)$ and Troyon normalized volume averaged plasma β for a discharge in which TAEs appear in a narrow time window after the termination of neutral beam injection (discharge 95796). The contour plot of magnetic fluctuations versus frequency and time indicates multiple modes near the calculated TAE frequency at $r/a \approx 0.3$ (solid line). The plasma parameters during mode activity were: $B = 5$ T, $I = 2.0$ MA, $R = 2.52$ m, $n_e(0) = 4.3 \times 10^{19}$ cm^{-3}, $T_e(0) = 6$ keV, $T_i(0) = 15$ keV. Mode activity appears after the slowing down of neutral beam ions ($t_{Beam} \sim 80$–100 ms) but before the thermalization of 3.5 MeV alphas ($\tau_\alpha 300$–400 ms), and in the TAE range of frequency: $f_{TAE} \sim 200$–250 kHz.

The TAE activity is clearly seen after termination of neutral beam injection as indicated by the amplitude of magnetic fluctuations. A sequence of short bursts 50–100 ms in duration are observed with toroidal mode numbers ranging from $n = 2$ to $n = 4$. At the time of mode activity, $q(0) \approx 1.5$ as obtained from MSE measurements, and $\beta_\alpha(0) \approx$ 0.05% as obtained from TRANSP code kinetic analysis. Mode activity appears after the slowing down of neutral beam ions ($t_{Beam} \sim 80$–100 ms), but before the thermalization of 3.5 MeV alphas ($t_a \sim$ 300–400 ms), and in the TAE range of frequency $f_{TAE} \sim 200$–250 kHz. The level of magnetic activity observed at the plasma edge is typically very small ($\tilde{B}/B \sim 10^{-8}$), however the internal level of magnetic fluctuations as inferred from reflectometer measurements of the density is considerably higher.

Figure 36 displays the theoretical predictions of the critical β_α for TAE instability at 150 ms after termination of neutral beam injection for a normal (positive) shear discharge with $q(0) < 1$,
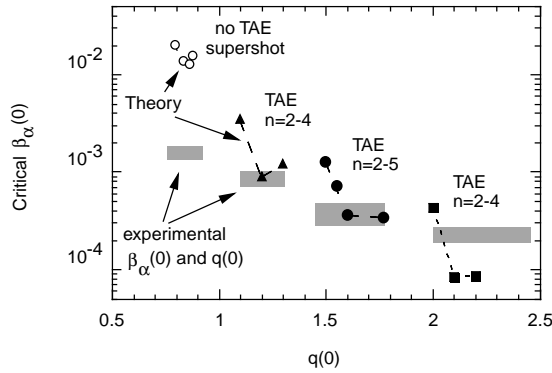
Figure 36. Calculated critical $\beta_\alpha(0)$ for excitation of alpha driven TAEs versus $q(0)$ from NOVA-K for a range of DT plasmas. The rapid decrease in the threshold β_α with increasing $q(0)$ from NOVA-K is shown (symbols) along with the experimental range of values for β_α and $q(0)$ as computed by TRANSP and MSE for these discharges (shaded regions). The analysis is performed at ≈ 150 ms after the end of neutral beam injection. The q profile for $r/a > 0.5$ is held fixed while the central q is varied so that the increase of $q(0)$ indicates a reduction of the central magnetic shear. No alpha driven TAEs are observed in normal magnetic shear DT supershot plasmas where $q(0) < 1$ (open circles). Alpha driven TAEs are observed in discharges with $q(0) > 1$ (closed symbols), consistent with the rapid decrease in the threshold β_α expected from NOVA-K.

compared with three $q(0) > 1$ reduced shear discharges which exhibit TAE activity. Also shown is the experimental range of $q(0)$ and β_α in these plasmas. No alpha driven TAE activity has been observed in $q(0) < 1$ plasmas following the end of neutral beam injection, consistent with the much larger calculated critical β_α required for TAE excitation. The theoretically expected trend of decreasing critical β_α with increasing $q(0)$ is qualitatively consistent with the experimental observation of alpha driven TAEs in TFTR.

6.4. Radial structure of alpha particle driven TAEs

Internal measurements of the alpha driven TAEs were obtained using the X mode core reflectometer diagnostic on TFTR [141, 142]. This diagnostic measures phase fluctuations induced on a probing microwave beam reflected from its cut-off layer as the layer moves due to density variations in the plasma.
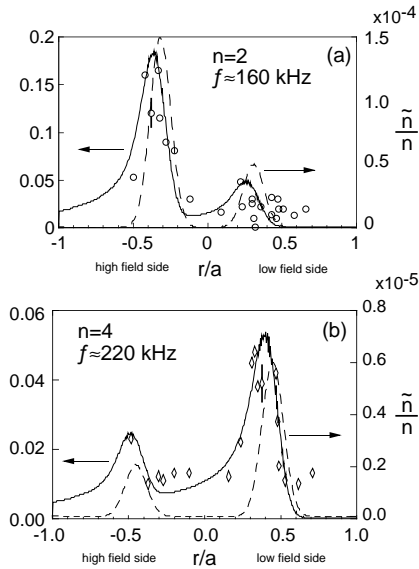

Figure 37. Map of (a) the phase observed on the reflectometer (open circles) for the $n = 2$ mode, and (b) the $n = 4$ mode, taken over a range of similar plasmas with $\sim 10\%$ variation in toroidal field keeping $q(a)$ constant. These plasmas showed essentially identical TAE activity. In panel (b) the data correspond to the time of peak magnetic fluctuation level on the outer midplane of the plasma. The simulation of the reflectometer response (solid line) to two Gaussian density perturbations (dashed line) is also shown. In panel (a) the two Gaussians are centred at $r/a = 0.32$ with a halfwidth of $r/a = 0.1$, while in panel (b) the two Gaussian density perturbations are located at $r/a = 0.45$. The radial mode structure of the low frequency $n = 2$ mode is clearly antiballooning, while that of the $n = 4$ mode is strongly ballooning at the time of peak magnetic fluctuation level on the outer midplane. The data confirm the core localization of the modes to the region of weak central magnetic shear.

A surprising result from the reflectometer measurements is that the structure of the low frequency $n = 2$ mode in Fig. 35 is strongly anti-ballooning, i.e. has a larger amplitude on the high field side of the plasma, as shown in Fig. 37. The reflectometer measurements clearly indicate a strong $n = 2$ mode on the high field side of the magnetic axis, with weak or no activity on the low field side of the magnetic axis, counter to the theoretically predicted radial eigenfunction. This mode is also observed at a frequency $\sim 30\%$ below the expected TAE frequency, and the mode is calculated to intersect the Alfvén continuum

[135]. The reflectometer data are consistent with an anti-ballooning mode structure with a peak amplitude $\tilde{n}/n \sim 1.5 \times 10^{-4}$, which corresponds to a peak magnetic field fluctuation level $\tilde{B}/B \sim 1.5 \times 10^{-5}$ in the plasma core. This should be compared with the peak magnetic signal on the outer midplane of $\tilde{B}/B \sim 2 \times 10^{-9}$ for the same mode, indicating it is highly core localized. Calculations indicate that these levels are too weak to induce significant loss of alpha particles from the plasma.

In contrast, the radial mode structure of the $n = 4$ mode at the time of peak magnetic activity on the outer midplane is also shown Fig. 37. The core localization, narrow mode width and frequency of the $n = 4$ mode is generally consistent with core localized alpha driven TAEs as predicted by theory [135]. However, the anti-ballooning structure of the $n = 2$ mode and its low frequency is difficult to explain using current TAE theory, which predicts that higher frequency outwardly ballooning modes should be unstable [135].

The density fluctuation level of all these modes is small ($\tilde{n}/n \sim (0.6{-}0.8) \times 10^{-4}$) and corresponds to $\tilde{B}/B \sim 10^{-5}$, as estimated from theoretical calculations of the radial eigenfunction. Preliminary analysis indicates that the peak density fluctuation level is of the order expected from non-linear theory for single mode saturation [143–145]. However, these estimates depend strongly on the value of the linear growth rate, such as calculated by NOVA-K.

At present no alpha particle loss associated with these modes has been observed on the lost alpha detectors, consistent with the weak mode amplitudes. Internal measurements of deeply trapped alpha particles in DT plasmas with TAE activity indicate possible redistribution of alpha particles (Section 3.3.1). The relative role of TAEs and toroidal field ripple in the redistribution of alpha particles is still under investigation.

The implications of these findings for a future tokamak reactor with advanced plasma shaping and reversed magnetic shear are still under investigation. However, the identification of the dominant damping and drive terms in current experiments provides an improved foundation for projecting TAE behaviour in future fusion devices (Section 8.3).

7. RF–alpha interactions

Radiofrequency waves, and especially ICRF waves, can interact with fusion product ions in a plasma [146–148]. The first potential consequence is that RF power which is intended to be absorbed on other species for heating or current drive can be absorbed by alphas, thereby reducing the heating or current drive efficiency. The second is that absorption of RF power by the alphas can cause them to escape from the plasma. Although this has the negative potential to put an additional heat load on the wall, it is also conceivable that this mechanism could be used for alpha ash removal [149]. Thirdly, measurement of low power ICRF absorption by alpha particles in certain harmonic number ranges may become a possible technique for diagnosing the alpha particle density profile.

In the same way that alpha particles can absorb RF wave power, they can also radiate it. This can result in so-called ion cyclotron emission (ICE) from the alphas in the plasma, as observed in JET and TFTR [150–152]. In another application of wave emission, radiation or amplification of RF waves by alphas with subsequent damping on other plasma species has been suggested as a means of harnessing alpha particle energy for plasma heating or current drive [26, 153, 154]. This has been termed 'alpha energy channelling'.

7.1. Historical background and previous work

A number of authors have made calculations of the expected rate of RF wave damping on alpha particles, and the rates of transport expected from such wave–particle interactions [155–157]. RF induced loss of fast ions has been observed in several tokamaks: TFTR [148], JT-60U [158, 159], Tore Supra [160] and TEXTOR [161]. This arises from RF induced transport of the alphas in velocity space, typically to more perpendicular velocities, that convects them into an existing loss cone. Experimentally observed rates of RF induced velocity space transport can equal or exceed those due to collisions with plasma particles. In present devices, the measured loss rates of fusion products to the wall associated with RF induced transport are tolerable.

The ICRF fast wave induced losses of DD fusion products were measured in TFTR [148], using the escaping fast ion loss diagnostic described in Section 2. With 3 MW of applied ICRF power, the loss rate at the detector was observed to be $\sim$1.8 times the baseline first orbit loss rate. The RF induced loss was concentrated at the pitch angle of the passing–trapped boundary, consistent with a process of perpendicular heating of marginally passing

counter-going fusion products such that they converted to 'fattest banana' (i.e. just barely trapped) orbits and were lost to the wall. The RF induced loss rate scaled as $P_{RF}^{0.6}$, roughly consistent with a diffusive model, which predicted a loss rate proportional to $P_{RF}^{0.5}$. This scaling arises from the fact that the wave fields produce a change in velocity given by ($\delta v \propto E_{RF} \propto P_{RF}^{0.5}$) [148]. In addition, it was found that the rate of RF induced diffusion, at the power levels used, was comparable to that induced by collisions.

ICE from fusion products has been observed in JET [150], TFTR [151] and JT-60U [152]. There have also been a number of theoretical efforts to explain the observed frequency spectrum and amplitude over a range of conditions and devices [162–167].

A number of theoretical papers detail the conditions under which alpha channelling could occur and improve the efficiency of a reactor [26, 168]. In general, that improvement in efficiency arises readily if the alpha energy can be applied to current drive. However, plasma heating by alpha channelling is most advantageous if the electrons and ions do not undergo rapid thermal equilibration—otherwise heating energy deposited in one selected species is quickly shared among all and the advantages of selective heating are lost.

ICRF heating in the H minority regime can produce an energetic proton tail, and this energetic tail can be used to study some aspects of alpha particle physics without the actual presence of alphas. In TFTR, this technique has been used principally to study TAEs [169]. In one condition, such TAEs caused sufficient losses of tail ions to the wall that the TFTR vacuum vessel was damaged [170].

7.2. ICRF induced loss of alpha particles

ICRF fast wave induced loss of alpha particles has been observed in TFTR [148]. Figure 38 shows the loss rate of alpha particles to the 90° fast ion loss detector from a DT discharge with modulated ICRF power. This is for a plasma with $R = 2.61$ m, $a = 0.99$ m, $B = 4.4$ T and $I = 1.75$ MA. The RF frequency was 43 MHz, so the T would be resonant at its second harmonic at $R = 2.72$ m, which is approximately the location of the Shafranov shifted magnetic axis. The rate of alpha particle loss shows modulation coincident with that of the RF power, indicating that the losses result from interactions between the alpha particles and the waves, since the RF did not change the background plasma properties
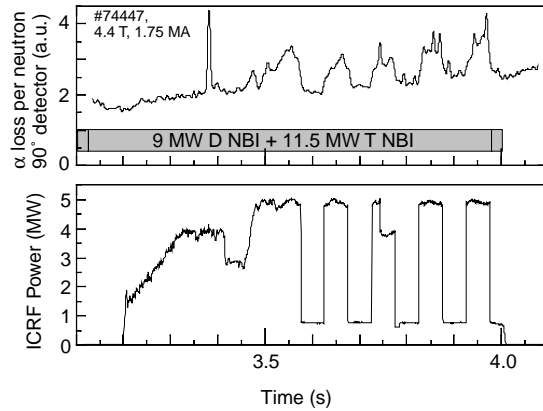

Figure 38. Alpha particle loss rate per neutron and applied ICRF power in a TFTR DT discharge. There is an additional loss of alpha particles which is synchronous with the applied ICRF power, indicating that the ICRF waves are inducing the loss of alpha particles. The baseline level of loss is due to first orbit loss. The spike of loss just before 3.4 s arises from an MHD instability in the plasma.
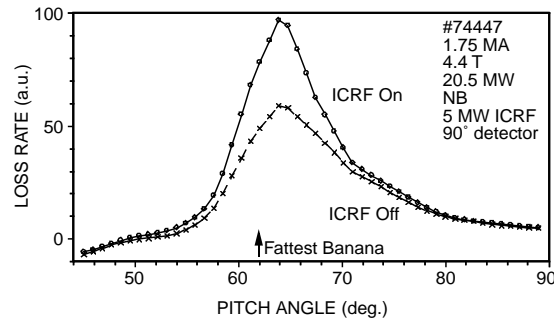

Figure 39. Pitch angle distributions of the alpha particle loss during two time slices of the discharge shown in Fig. 38. One time slice is during the low power phase of the ICRF modulation, and the other is at the high power phase. The additional alpha particle loss produced by the ICRF is concentrated around the pitch angle of the fattest banana orbit, indicating that it probably arises from conversion of marginally passing orbits into fat banana orbits by the ICRF waves.

on the modulation timescale. For this discharge, the applied RF power of 5 MW caused an increase of the detected signal level (first orbit loss) of ∼50%.

Figure 39 displays pitch angle distributions observed in the same detector during the same discharge. One distribution is taken during an interval of low RF power (labelled 'ICRF Off'), and the other

is taken during an interval of high RF power (labelled 'ICRF On'). It is apparent that the additional losses due to the RF waves are centred at a pitch angle of $\sim 64°$, which is very close to the pitch angle of the passing–trapped boundary at this detector, 62°. As with DD fusion products [148], the loss appears to be due to conversion of marginally passing particles to the 'fattest banana' loss orbits. By computing the alpha particle orbits from the energy and pitch angle measured, it is found that they cross the midplane at $r/a \approx 0.2$. This is therefore inferred to be their flux surface of origin. The banana orbits are essentially all confined inside of this surface. Since the birth distribution of alphas is very peaked, varying radially approximately as $[1 - (r/a)^2]^8$, the signal contains only a small component of alphas at $r/a > 0.2$.

The RF induced loss has been measured as a function of the toroidal field, as shown in Fig. 40. The RF induced loss is seen only at B values above 3.4 T and below 4.8 T, with the strongest loss arising at ~ 4.1 T. The range of B over which a marginally passing alpha particle at $r/a \sim 0.2$ could interact with the ICRF wave can be readily calculated from the Doppler–shifted cyclotron resonance condition, $\omega_{RF} = \Omega_\alpha - k_\| V_\|$. Here ω_{RF} is the frequency of the ICRF wave, Ω_α is the local cyclotron frequency of the alpha particles, $k_\|$ is the parallel wavenumber of the ICRF wave and $V_\|$ is the parallel velocity of the particles. The range of potential interaction derived from this formula agrees well with the range over which loss is observed, as shown by the shaded region in Fig. 40.

7.3. ICE from DT plasmas

ICE from TFTR DT plasmas was measured with a set of single turn loops inside the TFTR vacuum vessel [151], and also observed in JET [150] and JT-60U [152]. Ordinarily, harmonics of the cyclotron frequencies of fast ions at the outer midplane edge of the plasma were observed. For typical TFTR supershots in DT, emission at alpha particle cyclotron harmonics arises at the start of neutral beam injection, and then vanishes within 100–250 ms. Thereafter, harmonics of the injected beam species are observed, until NBI ceases.

The observed features of ICE agree well with those predicted by the mechanism of the magnetoacoustic cyclotron instability (MCI), also known as the Alfvén cyclotron instability (ACI) [162–167]. This is an Alfvén wave which can be destabilized by a
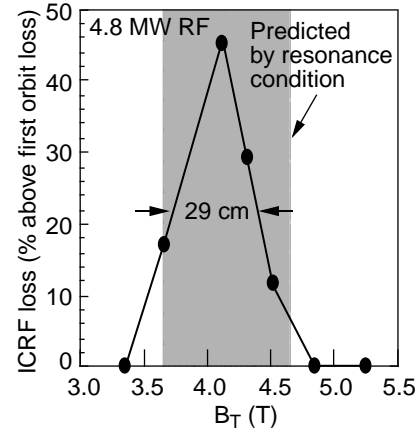

Figure 40. Alpha particle loss rate to 90° detector during ICRF heating as a function of B. Points show measurements from experiment, and the shaded region shows the range of B over which marginally passing alphas are in Doppler shifted cyclotron resonance with the ICRF wave. The FWHM of the range of interaction corresponds to a movement of the resonance location by 29 cm.

population of energetic ions. The differences between the behaviour in JET and TFTR L mode and supershot plasmas are now understood to be determined by the difference in growth rates found when the MCI is driven by sub-Alfvénic versus super-Alfvénic particles. Alpha particles in the edge of TFTR supershots are sub-Alfvénic while those in JET and in TFTR L mode shots are super-Alfvénic. The MCI has a positive growth rate for a range of fast ion distributions when the ions are super-Alfvénic, as they are in JET and in TFTR L mode plasmas. However, when the ions are sub-Alfvénic, a strongly anisotropic fast ion distribution is required to produce any instability at all, and the growth rates tend to be smaller than those for super-Alfvénic ions. In TFTR supershots, that type of unstable anisotropic distribution is present for the first 100–250 ms of NBI, but isotropy induced by slowing down and pitch angle scattering as time passes eventually converts the distribution into one which is stable, at which point the ICE subsides. In all cases, a sufficient degree of anisotropy is present in the alpha distribution only near the plasma edge, and the MCI is not unstable in the plasma interior, accounting for why only emission at the edge cyclotron harmonics was seen.

Characteristic 'early' and 'late' ICE spectra from one such DT supershot are shown in Fig. 41, along with a plot of the cyclotron harmonic frequencies
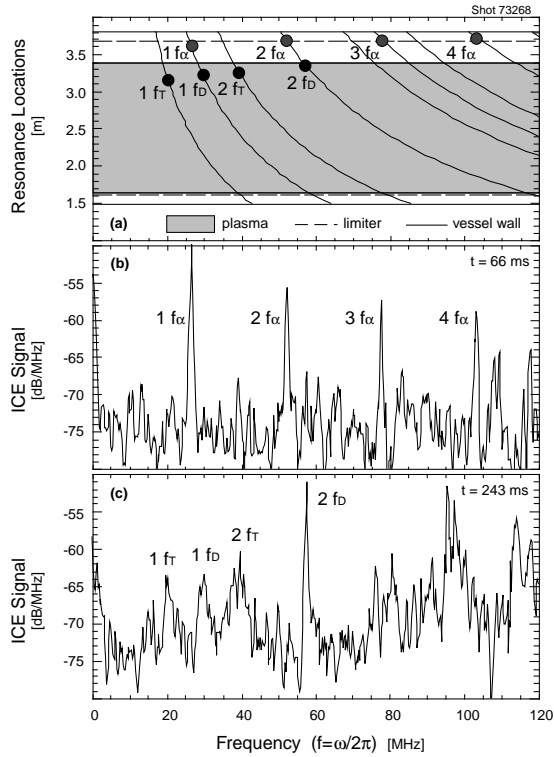
Figure 41. Early (66 ms) and late (243 ms) ICE spectra from a DT supershot. The curves in panel (a) show the cyclotron frequencies (and their harmonics) for several species as a function of major radius. The measured frequency spectrum early during NBI, panel (b), shows multiple harmonics of alpha particles at the outboard edge of the plasma. Later, only frequencies associated with injected beam species, panel (c), are seen, as the alpha particle has isotropized.

versus major radius. It is clear that the observed frequencies match those expected in the vicinity of the outboard edge of the plasma. At 66 ms after the start of beam injection, four harmonics of f_α are clearly visible, with no clear evidence of emission from beam species. Later, at 243 ms after the start of NBI, the signals at nf_α have vanished and broader peaks at the first and second harmonics of the D and T beam ions have appeared. The time history of the first harmonic, f_α, emission is shown in Fig. 42. In contrast to the results from TFTR supershots, JET ICE [150] persisted throughout NBI. Emission at f_α harmonics also persists throughout NBI in TFTR L mode DT discharges, as shown in Fig. 43.
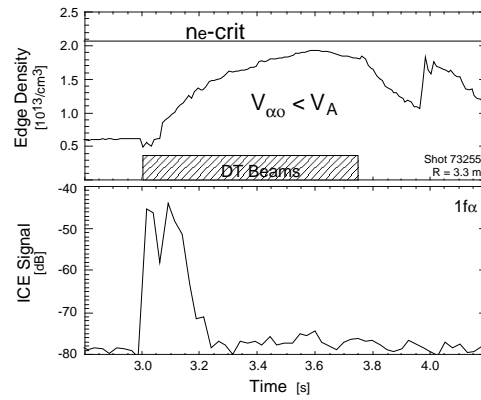

Figure 42. Measurement of the alpha particle driven ICE during a typical DT supershot. The edge electron density and ICE power in the f_α fundamental are plotted as functions of time. Birth alpha particles are sub-Alfvénic in the plasma edge, and the f_α fundamental is only excited briefly at the onset of NBI. The line marked 'n_e-crit' designates the density at which the edge Alfvén velocity equals the alpha particle birth velocity. For densities below that line, the alphas are sub-Alfvénic.
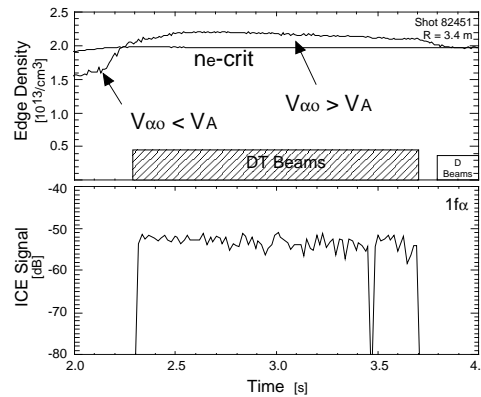

Figure 43. Measurement of the alpha particle driven ICE during a DT L mode discharge. The same quantities are shown as in Fig. 42. In this case, $V_{\alpha 0} > V_A$ throughout the beam injection phase. The fundamental is excited at the onset of NBI and persists until the beams are turned off.

7.4. Search for alpha channelling in DT plasmas

As noted above, it has been conjectured that ICRF waves could be used to extract energy from the alpha particle population in a DT plasma and deposit that energy in bulk electrons or ions for the purpose of plasma heating or current drive, a process

termed 'alpha channelling' [26, 153, 154, 168, 171]. Under some plasma conditions, alpha channeling could improve the performance of a fusion reactor. Although it is conceivable that alpha channelling could result from random fluctuations, it would be more controllable if an externally launched wave is applied to the plasma which then extracts energy from the alphas and damps it on another species. Theoretical considerations, namely the need to move alpha particles a large distance in minor radius as their energy is absorbed by the wave, and a desire to interact with the widest possible range of alpha velocities, dictate that waves with a large k are best for alpha channelling. The ion Bernstein wave (IBW) is such a wave in the ICRF, and it was most readily generated in TFTR through the process of mode conversion of fast waves in a two ion species plasma. Such waves were used for electron heating and current drive in D^3He plasmas in TFTR [172] and, to a limited extent, in DT plasmas. For complete alpha channelling in TFTR or a reactor scale tokamak, a second wave would be required to assure that low energy alphas were completely removed from the plasma [168].

Some experiments were run in DT plasmas in order to look for signatures of alpha channelling or related effects. These were done with the ICRF system operating at 30 MHz. Plasmas were made with $B \sim 6$ T and with $n_T/(n_T + n_D) \sim 0.5$ (about the maximum concentration of T attainable in TFTR, given the rate of D recycling from the limiters) in order to locate the mode conversion layer at or just outside of the magnetic axis position. This latter constraint should have provided the widest spectrum of $k_\parallel$ in the resultant IBW, thereby maximizing the likelihood of interaction with alpha particles. Numerical modelling predicted that the IBW should have caused $\sim 13\%$ of alpha particles to be lost near the midplane at energies well below their birth energy [171]. Only a few DT shots under these conditions were attempted. However, none of these showed any measurable signal that could be attributed to cooled alpha particles in any of the fast ion loss detectors, including the detector at 20° below the midplane.

A more extensive campaign to develop and test components of alpha channelling was conducted in D^3He plasmas with neutral beam ions in place of alpha particles [168, 171, 173]. This campaign demonstrated that the IBW could cause significant diffusion in energy and minor radius at a rate large compared with collisional diffusion and slowing down. Evidence was also obtained for reversal of

the IBW $k_\parallel$ while propagating in the interior of the plasma. Both these properties are required for alpha channelling.

A major hindrance in the alpha channelling experiments on TFTR was the lack of knowledge about the parameters of the IBW. Its presence could be inferred only indirectly, from evidence of electron heating seen in the electron temperature profile. A direct measurement of the IBW would have been valuable to confirm its presence, amplitude, position within the plasma and wavenumber spectrum. The microwave scattering diagnostic on TFTR was tried, but it proved unable to detect the IBW. Without measurements of the wave parameters, much of the experimental work proceeded on the basis of assumptions about the wave parameters in the plasma interior.

7.5. Open issues and future work needed

Further work is warranted in the area of alpha particle damping of ICRF waves, as not much time was devoted to this issue on TFTR. Concerning RF induced alpha particle losses, a good calculation of the expected loss rate versus toroidal field is needed. In addition, understanding of whether the pitch angle difference between the peak of the distribution during RF and the computed fattest banana orbit is significant, and a calculation of the average energy gain of alpha particles due to the RF wave fields in each condition would be valuable.

At present, the theory and experimental results for ICE are in good agreement. One area that could be further pursued here is the question of whether measurement of the absorption of low power ICRF waves could be used as a diagnostic of alpha particle density in a future DT tokamak.

In the area of alpha energy channelling, there are many things that could be done to further the work. These include measuring the wave fields in the plasma, obtaining better control of the IBW parameters and developing more detailed measurements of the behaviour of the confined fast ions as they are acted upon by the IBW.

8. Summary and conclusions

The TFTR DT experiments during 1993–1997 provided the most extensive set of data so far on alpha particle behaviour in tokamaks. This section summarizes the results discussed in Sections 2–7 and

outlines the needs for future alpha diagnostics, modelling and experiments.

8.1. Alpha particle behaviour in MHD quiescent discharges

The general conclusion from these experiments is confinement and thermalization of 3.5 MeV alpha particles appears to be consistent with classical models under normally MHD quiescent plasma conditions. However, this general statement is based on a rather complex and incomplete set of data and modelling, and so is only an approximate description of the actual behaviour of alpha particles in TFTR.

The principal evidence for classical confinement and thermalization of alpha particles in MHD quiescent TFTR DT discharges consists of the following (listed in order of the discussion within this article):

(a) Consistency between the relative alpha particle loss measured by the scintillator detector 90° below the outer midplane and the calculated first orbit loss as a function of plasma current (Fig. 8), and agreement between the measured and calculated loss versus pitch angle and gyroradius (Fig. 9);

(b) Consistency between the absolute magnitude, energy and pitch angle distribution of the alpha particle loss measured by the alpha collector probe at $I = 1.0$ MA and the calculated first orbit loss (Fig. 14);

(c) Consistency between the shape of the alpha energy spectrum in the energy range $E \approx 1.0-3.5$ MeV as measured by PCX near the plasma centre and the calculated classical slowing down spectrum (Fig. 15);

(d) Consistency between the radial alpha profiles measured by PCX and the calculated profiles, including the approximate location of the stochastic TF ripple diffusion boundary at large r/a (Fig. 16),

(e) Consistency between the absolute magnitude and shape of the alpha energy spectrum as measured by α-CHERS in the range $E \approx 0.05-0.7$ MeV near the plasma centre and the calculated classical spectrum (Fig. 21) and its time dependence after NBI turn-off (Fig. 22);

(f) Consistency between the shape of the radial profile of the measured α-CHERS signals and calculated profiles from TRANSP modelling (Fig. 23);

(g) Consistency between the measured central electron heating attributable to alpha particles and the calculated heating based on classical alpha modelling (Fig. 27);

(h) Consistency between the measured thermal alpha ash (i.e. He) levels versus time and the calculated levels expected from classical fast alpha particle confinement and the known anomalous radial transport of thermal He (Figs 29 and 30).

Among these various comparisons of data and modelling, the best evidence for classical alpha confinement and thermalization in TFTR probably comes from the comparisons of the α-CHERS measurements with TRANSP calculations, as discussed in Section 4.2. These measurements showed absolute agreement with the classical model to within about $\pm 20\%$. This is a rather remarkable level of agreement, given the uncertainties in the alpha source and thermalization rates, and the great difficulty of this measurement. Note, however, that the classical alpha loss was small for these experiments ($<10\%$), so these results do not accurately check the modelling of the alpha loss itself.

Probably the next best evidence of classical alpha confinement and thermalization comes from comparisons of the energy spectra measured by the PCX diagnostic with the classical slowing down spectrum, as discussed in Section 3.2. The shape of the spectrum measured near the plasma centre agreed with the model to within the error bars of the measurement, which are typically $\pm 70\%$ at each point. However, the PCX diagnostic was not absolutely calibrated and viewed only a relatively small fraction of the confined alpha orbits.

The lost alpha measurements yielded a mixture of agreement and apparent disagreement with classical model predictions. The scintillator detector 90° below the outer midplane showed the classically expected decrease in the alpha loss per neutron over a factor of about 7 between $I = 0.6$–2.7 MA, as described in Section 2.1.2. The alpha collector probe at 90° below the outer midplane showed an absolute agreement with the expected first orbit loss to within about $\pm 50\%$ at $I = 1.0$ MA, as discussed in Section 2.2. However, the results from the scintillator detectors at poloidal angles nearer to the outer midplane, and also the results from the 90° alpha collector probe at higher plasma current ($I = 1.8$ MA), were both in clear disagreement with the first orbit loss model. As discussed in Section 2.4, these results are probably due to TF ripple loss, but the spatial distribution of this loss cannot yet be

calculated accurately enough for a quantitative comparison with the data, mainly due to the very small aperture which collects only a tiny fraction of the alpha particle source ($\approx 10^{-8}$).

The experiments on alpha heating and He ash content sampled the largest fraction of the alpha distribution function (essentially all of it), but also gave the most indirect evidence for classical alpha confinement and thermalization. The uncertainties in these two measurements were about $\pm 50\%$ for the alpha heating and $\pm 30\%$ for the alpha ash content. However, both experiments rely on supplementary empirical information to infer the classical alpha behaviour, i.e. on the temperature scaling with τ_E for the alpha heating measurement and on the anomalous thermal He diffusivity for the He ash measurement.

The largest uncertainty concerning the classical alpha particle behaviour in TFTR involved the mechanism of alpha particle ripple loss. Since the calculated alpha ripple loss fraction is only ≈ 10–20% for normal TFTR discharges, most of the alpha measurements were not sufficiently accurate to check these calculations. The best comparison for confined alphas comes from the PCX measurements, which showed a depletion in the trapped alpha density near the outer midplane where TF ripple loss was expected, and a larger central depletion at higher $q(0)$ and reversed magnetic shear, as expected from theory (Section 3). However, the cases with normal shear were only compared with the simplified stochastic ripple model (e.g. without collisions), and the reversed shear cases had a very limited data set. A systematic experiment on alpha ripple loss in the midplane detector showed qualitative consistency with the TF ripple modelling, but a quantitative check of the theory was not possible due to difficulty of the modelling (Section 2.1.3). Therefore, a definitive verification of the classical alpha ripple loss theory was not obtained on TFTR.

One way to summarize the TFTR alpha confinement measurements is to evaluate effective radial diffusion coefficients D_α for the alphas in specific experimental circumstances [44]. Three independent estimates of the alpha diffusion coefficients were made, each based on different alpha diagnostics, as shown in Fig. 44; also shown are estimates of the corresponding diffusion coefficients for 1 MeV tritons in TFTR [174], and inferences for thermal and beam on diffusion coefficients. The alpha particle diffusion coefficients are all in the range $D_\alpha \approx 0.01$–0.1 m^2/s, although each diagnostic measured a different part of

phase space (minor radius and pitch angle). Assuming that the alpha diffusion coefficients are at the high end of this range, the implied global alpha confinement time is roughly

$$\tau_\alpha \approx a^2/(4D_\alpha) \approx (1 \text{ m})^2/(4 \times 0.1 \text{ m}^2/\text{s}) \approx 2 \text{ s} \quad (13)$$

Since this time is considerably longer than the alpha thermalization time of $\tau_\alpha \approx 0.4$ s (Table 1), the overall alpha confinement should be very good, which is consistent with the results obtained from the alpha heating and ash measurements. However, it is important to note that this low effective diffusion rate does *not* directly imply a negligible alpha loss, since parts of the alpha distribution function were not measured in these experiments, for example, trapped high energy alphas which are sensitive to stochastic TF ripple diffusion could still be lost rapidly.

It is interesting that the inferred alpha diffusion coefficients are similar to the 1 MeV triton diffusion coefficient obtained from the DD triton burnup measurements on TFTR. This implies that this good alpha confinement is not just a property of DT plasmas, but is most likely a property of fast ions in all TFTR plasmas. The observed decrease of the fast ion diffusion coefficients with increasing fast ion energy suggested by Fig. 44 is at least qualitatively consistent with the model of spatial orbit averaging (Section 1.2), but a quantitative test of this model has not yet been carried out, in part due to large uncertainties about the structure of the internal plasma turbulence.

In cases where the alpha particle confinement was best, i.e. in MHD-quiescent plasmas, it was seen that the alpha thermalization process was consistent with the classical collisional models. This was most clearly seen for alphas measured near the plasma centre by both the PCX (e.g. Fig. 15) and α-CHERS (e.g. Fig. 22) diagnostic. Although there was also evidence for an unexpected loss of partially thermalized alphas at the vessel bottom (Section 2.2), this was at least qualitatively explained as collisional TF ripple loss [65].

Thus there is no unambiguous evidence for any non-classical alpha diffusion or loss in MHD-quiescent TFTR DT discharges.

8.2. Effects of MHD and RF waves on alpha behaviour

The overall conclusion from these experiments is that MHD and RF waves certainly did affect alpha particles in TFTR, but that these effects do not significantly degrade the normally good global alpha
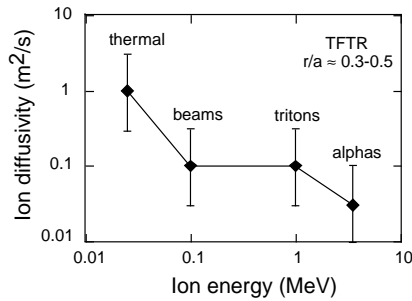
Figure 44. Estimates of the radial fast ion diffusion coefficient at $r/a \approx 0.3$–0.5 for various types of ions in TFTR. Three independent measurements of the radial alpha diffusion coefficient give $D \approx 0.03$ m^2/s (within a factor of about 3), which is comparable to or slightly less than the inferred $D \approx 0.1$ m^2/s for 1 MeV tritons measured by their burnup [174]. Thermal ions at $E \approx 20$–30 keV have typically $D \approx 1$ m^2/s [25], and beam ions 0.05–0.2 m^2/s, both of which appear to have a D which increases with r/a.

particle confinement. However, it should be emphasized that this statement is based on a limited set of data and modelling, and that all of these interactions depend strongly on the details of the MHD and RF wave amplitudes and spectra.

A list of the various MHD and RF–alpha interactions studied in TFTR is shown in Table 7, ordered in terms of their characteristic frequencies. The most complete data and analysis was done for the sawtooth crash effect, which was observed in all three alpha diagnostics. All the other MHD and RF interactions were observed only in the alpha loss detectors, with the exception of a possible TAE interaction seen in the PCX data (Section 3.3.2), and ICE emission observed using magnetic pick-up loops (Section 7.3). This was largely because lost alpha detectors took data with good time resolution for almost every DT discharge, whereas the other alpha diagnostics were only used under specific experimental circumstances, usually in the absence of MHD or RF.

An internal redistribution of confined alphas due to the sawtooth crash was observed in both the PCX, which measured only deeply trapped alphas (Section 3.3.1) and α-CHERS, which was dominated by passing alphas (Section 4.3). In a few cases, alpha loss was also observed at sawtooth crashes (Section 2.1.4). In the best studied case ($I = 2.0$ MA), the α-CHERS diagnostic showed that alphas were

significantly redistributed from inside to outside the $q = 1$ surface with no apparent loss of alpha particle density (Fig. 25). This result was at least qualitatively consistent with both the PCX and lost alpha measurements, which showed a strong internal redistribution of the trapped alphas (Fig. 18), and no significant alpha loss at the crash.

Theoretical analysis and modelling of the sawtooth crash has been applied in various ways to explain this behaviour. The data from α-CHERS was successfully explained using a simple magnetic reconnection model in which the alpha density was moved radially along with the magnetic flux surfaces, without considering the detailed time evolution or alpha distribution function. The relatively larger radial redistribution seen in the PCX data for trapped alphas could not be explained by this simple reconnection model, but needed the addition of a model for the transient helical electric field, which further changed the alpha particle energy and the position of trapped orbits (Section 3.3.1). An analysis of this redistribution based on the time dependent orbit dynamics was tried [175], but was limited by a lack of knowledge of the actual internal perturbations. An analysis of the alpha loss data based on the energy and pitch angle dependent reconnection model is in progress [72]. In general, these models can explain the existing data to within the joint uncertainty of the alpha particle measurements and the sawtooth dynamics, and so could be applied to future machines like ITER.

The effects of the other types of MHD listed in Table 7 (and described in Sections 2, 6 and 7) were less well understood, since there were few controlled experiments with these waves 'on' and 'off', such as were done for the sawtooth crash effect. There was also limited knowledge of the internal structure and amplitudes of the relevant waves, and an absence of data on the confined alpha populations. The best studied MHD–alpha interaction was for the KBM mode [71, 176], and the best studied RF–fusion-product interaction was for the ICRF fast wave [148]. In both cases a theoretical model was successful in explaining the relative increase in the lost alpha signals to within about a factor of 2. In most other cases there was an alpha loss observed but the modelling is still incomplete, largely due to lack of knowledge of the internal MHD or RF perturbations. Despite this lack of experimental verification, the theory of MHD and RF effects on alphas is fairly well developed and can serve as the basis for calculations of alpha effects in future machines.

The most important experiment on MHD–alpha interactions in the TFTR DT run was the observation of the alpha driven TAE (Section 6). However, there was only one piece of evidence for an effect of this wave on the alpha particle behaviour, as shown in the PCX data of Fig. 19. No systematic measurements were made using α-CHERS, and this TAE was so small and transient that there was no significant alpha particle loss. Much more work is needed to evaluate the effect of collective alpha instability on alpha particle confinement.

8.3. Alpha particle driven instabilities

The DT experiments on TFTR have greatly advanced our understanding of TAEs and their interaction with fusion alpha particles. These experiments demonstrated the value of TAE theory as a predictive tool for the stability analysis of tokamak plasmas.

The observation of low-n alpha driven TAEs in weak magnetic shear discharges in TFTR confirmed the critical role of the q profile in mode stability. These experiments should be followed up on other tokamak experiments in which magnetic shear modification is used to access regimes of enhanced plasma confinement. Other features of advanced tokamak performance such as strong flow shear, steep pressure gradient and large radial electric field should also be evaluated with respect to their effect on fast ion driven TAE stability.

The most unstable TAE n-number is expected to increase with machine size, since the most unstable modes are in the range $k_{pol}\rho_\alpha \sim 1$, and since the alpha gyroradius is fixed by the toroidal field. Thus existing alpha particle experiments cannot directly simulate the high-n TAE spectrum expected in fusion reactors the size of ITER ($n = 10$–50). Also, the centrally peaked alpha particle pressure gradient in TFTR plasmas may not be a feature of fusion reactors operating with broader pressure profiles. Thus a reactor relevant goal of future alpha particle simulation experiments would be to vary the toroidal magnetic field and fast ion pressure gradient to verify the scalings of TAE instability.

The reactor relevance of TAEs also needs to be assessed in alternate confinement schemes such as spherical tokamaks and quasi-axisymmetric tokamaks. In spherical tokamaks such as NSTX and MAST, neutral beam ions far exceed the Alfvén velocity, implying the potential to excite TAEs. The small aspect ratio, high-β and low magnetic field of these devices opens up entirely new regimes for studying the basic physics of Alfvén eigenmodes and for assessing their reactor relevance in alternate confinement schemes.

It should be noted that there was no clear experimental evidence for any alpha driven high-n KBMs or BAEs in TFTR, even though the effect of KBMs on alpha loss was seen in some high-β discharges [176]. Similar MHD activity was observed in comparable DD discharges [131, 176], and the presence of any possible alpha drive was not isolated in the DT cases. However, early theoretical predictions for an alpha particle induced reduction in the KBM instability threshold [3, 177, 178] were not explicitly tested on TFTR, so it is possible that such effects were simply unobservable in the DT discharges.

8.4. Alpha particle diagnostics

The alpha particle diagnostics on TFTR were very successful, given that they all involved substantial technical challenges and were tested in DT for the first time during these TFTR experiments. This section reviews the overall performance and limitations of these diagnostics, and points to potential improvements for future experiments.

The main limitation of the confined alpha diagnostics (PCX, α-CHERS) was that each required very special plasma conditions to operate, so the confined alpha data were not available for most of the DT experiments. For example, the α-CHERS could only operate with a relatively low electron density and low neutron background, due to visible bremsstrahlung and fibre-optic fluorescence, respectively, so most of its data was taken after the main DT source was turned off. This limitation could in principle be overcome with beam modulation and additional shielding on the fibre-optics of α-CHERS, but the PCX requirement for pellet penetration was not achievable during high power NBI on TFTR. However, passive double charge exchange of alphas on intrinsic impurities has recently been demonstrated on JET [179], and may be more suitable for future experiments.

The main limitation of the alpha loss detectors was their very small apertures (≈ 0.01 cm^2), so they could only measure the alpha loss through a few small 'keyholes' at the wall. Although the scintillator detectors gave very detailed local information on alpha loss for almost every DT discharge, it was not possible to reconstruct the global alpha loss from this data set. Ideally, a large-area alpha loss measurement

should also be available to evaluate the spatial distribution of global loss, even if it lacks energy, time and pitch angle resolution. This might be done by measuring the wall surface temperature rise due to alphas, or perhaps using a large alpha collector panel. However, such a panel probably needs to be removable for analysis, and also must withstand the highest level of alpha heat flux to make the relevant measurements.

The other alpha diagnostics which were either tried or considered for TFTR were listed in Table 4. Of these, perhaps the most effort was made on the collective Thomson scattering using a gyrotron source. Ideally, this could have provided a nonperturbing measurement of the confined alpha distribution function, but no alpha measurements were made due to a combination of diagnostic and modelling difficulties. Some progress in this area has been made at JET [180], but as of this writing no alpha measurements have been made this way.

The greatest need for improved alpha diagnostics is to evaluate the TF ripple and MHD/RF wave induced alpha transport, since data on these effects are presently very limited. Particularly useful would be a way to routinely measure rapid time variations of the confined and lost alpha populations, such as those due to sawteeth or TAEs. Such confined alpha measurements would need to be accurate to better than $\approx 10\%$ to identify the global loss due to these effects, and alpha loss measurements would need to measure a global alpha loss level of $\leq 10\%$.

8.5. Alpha particle modelling

The basic features of classical alpha behaviour in TFTR were satisfactorily modelled in the TRANSP code [14, 19], while more specialized codes were used to treat specific physics issues, for example the Lorentz ORBIT code for alpha loss [8, 57], the ORBIT code for TF ripple loss [13, 15, 17], the FPPT code for sawtooth redistribution [87, 90], and the NOVA-K [126, 134] and ORNL [136] models for TAE instability studies. The analysis functions of these codes are summarized briefly in Table 8.

There are a few classical effects which should be added into the TRANSP and ORBIT alpha modelling codes used to interpret experimental data. For example, neither these codes nor the Fokker–Planck alpha modelling codes [65, 181] presently include the Doppler broadening of the alpha birth energy, which can be up to about ± 0.5 MeV for

beam–target reactions in TFTR. Also, neither TRANSP nor ORBIT have an accurate model of the vacuum region between the plasma boundary and the vessel wall, which can be important in determining the location of the alpha loss. Finally, these codes do not calculate the charge exchange of alphas on impurity ions, which is interesting for diagnostic purposes [32, 179], nor do they have a realistic enough model of the 3-D structure of the first wall to calculate the spatial location of the alpha ripple loss.

There is a real need for a qualitative improvement in the speed of the Monte Carlo codes used for collisional TF ripple or MHD induced alpha loss calculations. Progress has been made by following only those alphas which are in sensitive regions of phase space [13, 28], but many orders of magnitude higher computing speed is needed to calculate, for example, the local alpha heat load onto the first wall of a reactor to centimetre scale accuracy.

In the area of MHD– and RF–alpha interactions, the models generally assume a simplified mode structure based on theory, since the internal fluctuating magnetic fields are not directly measured. However, these models should be improved to match the available, but usually very complex data, for example on the time evolution and structure of the sawtooth crash or the coherent modes. Ideally, non-linear codes which include together both the MHD and the fast particle physics [182] should be used to interpret the experimental data.

Perhaps the greatest challenge for improved modelling is on the non-linear interactions between alpha driven collective modes and alpha particle transport, for example the effect of TAEs on the internal redistribution of alphas in TFTR. Some progress has been made in the theory of this interaction [28, 29, 184–187], and in interpreting the TAE induced transport of NBI or RF tail ions due to TAEs [188–191]. The results of such studies would help to clarify the degree to which collective alpha effects will affect the confinement of reactor grade tokamak plasmas.

8.6. Implications for future experiments

This review of the TFTR alpha particle experiments leads to the optimistic conclusion that, given this evidence for classical alpha behaviour in TFTR, it is very likely that efficient alpha particle heating will occur in future tokamak burning plasma experiments and reactors. This is largely due to the general

Table 8. Alpha particle codes used for TFTR experiments

Code name [Ref]	Analysis functions
TRANSP [14, 19]	Classical calculation of time dependent alpha source profiles, alpha pressure and distribution functions, and ripple loss (based on the GWB model)
ORBIT [13, 17]	Guiding centre calculations of alpha particle orbits with pitch angle scattering and slowing down, TF ripple and MHD modes, for a steady state magnetic equilibrium
Lorentz ORBIT [8, 57]	Calculation of alpha first orbit loss, including finite-gyroradius effects, especially for the lost alpha detectors
FPPT [87, 90]	Fokker–Planck post-processor for TRANSP for calculation of classical alpha particle distribution functions, especially for the PCX diagnostic
NOVA-K [126, 134]	TAE stability analysis, including ideal MHD mode structure along with kinetic effects
ORNL code [136]	Gyro-Landau fluid model of TAE stability along with model for fast ion population

expectation that increased plasma size and current will tend to improve alpha confinement beyond the already good level seen in TFTR.

However, there are also many open issues and uncertainties concerning this assessment which motivate further research in this field. The leading issues in alpha particle physics which were left unresolved in the TFTR DT experiments are:

(a) The potential non-linear consequences of alpha driven instabilities such as the TAE, particularly at the higher alpha pressure gradients and mode numbers expected in tokamak reactors, which could result in a significant loss of alpha confinement and perturbation of the background plasma;

(b) A quantitative understanding of the distribution of alpha ripple loss on the first wall, particularly the effects of the vacuum fields and slight misalignments in the surfaces, which could lead to overheating and damage to the wall even at modest levels of global alpha ripple loss;

(c) An understanding of the effect of plasma turbulence on alpha transport, for example to predict alpha transport in future machines given the ratio of alpha orbit size to turbulence size

scale, which might change if the turbulence size scale changes in larger devices;

(d) Development of active methods to control the profiles of alpha heating and thermalized He ash in future burning plasmas, particularly in 'advanced' operating regimes in which these profiles may determine plasma confinement and stability.

Some of these issues, particularly (a) and (b), have already been considered in detail from the perspective of the ITER physics basis [29]. We hope these issues will also be explored further in devices in which fast ions can be used to simulate the open physics issues (c) and (d).

Acknowledgements

References

[1] Heidbrink, W.W., Sadler, G., Nucl. Fusion **34** (1994) 535.

[2] Bosch, H.-S., Fusion Products Bibliography, Rep. IPP 1/313, Max-Planck-Institute für Plasmaphysics, Garching (1998).

[3] Furth, H.P., Goldston, R.J., Zweben, S.J., Sigmar, D.J., Nucl. Fusion **30** (1990) 1799.

[4] Zweben, S.J., Furth, H.P., Mikkelsen, D.R., Redi, M.H., Strachan, J.D., Nucl. Fusion **28** (1988) 2230.

[5] Strachan, J.D., et al., Nucl. Fusion **36** (1996) 1189.

[6] Hively, L.M., Miley, G.H., Nucl. Fusion **17** (1977) 1031.

[7] Kolesnichenko, Ya. I., Nucl. Fusion **20** (1980) 727.

[8] Zweben, S.J., et al., Nucl. Fusion **35** (1995) 893.

[9] Huba, J.D., NRL Plasma Formulary, Office of Naval Research, Washington, DC (1994).

[10] Goloborod'ko, V.Ya., et al., Nucl. Fusion **35** (1995) 1523.

[11] Chang, C.S., et al., Phys. Plasmas **1** (1994) 3857.

[12] Goldston, R.J., White, R.B., Boozer, A., Phys. Rev. Lett. **47** (1981) 647.

[13] White, R.B., Goldston, R.J., Redi, M.H., Budny, R.V., Phys. Plasmas **3** (1996) 3043.

[14] Redi, M.H., et al., Nucl. Fusion **35** (1995) 1509.

[15] Redi, M.H., et al., Nucl. Fusion **35** (1995) 1191.

[16] White, R.B., Chance, M.S., Phys. Fluids **27** (1984) 2455.

[17] Redi, M.H., et al., Phys. Plasmas **4** (1997) 4001.

[18] Budny, R.V., Nucl. Fusion **34** (1994) 1247.

[19] Budny, R.V., et al., Nucl. Fusion **35** (1995) 1497.

[20] White, R.B., Mynick, H.E., Phys. Fluids B **1** (1989) 980.

[21] Manfredi, G., Dendy, R.O., Phys. Rev. Lett. **76** (1990) 4360.

[22] Myra, J., et al., Phys. Fluids B **5** (1993) 1160.

[23] Mynick, H.E., Zweben, S.J., Nucl. Fusion **32** (1992) 518.

[24] Fonck, R.J., et al., Phys Rev. Lett. **70** (1993) 3736.

[25] Efthimion, P., et al., Phys. Rev. Lett. **75** (1995) 85.

[26] Herrmann, M., Fisch, N.J., Phys. Rev. Lett. **79** (1997) 1495.

[27] Sigmar, D.J., et al., Plasma Phys. Control. Fusion **34** (1992) 1845.

[28] Putvinski, S., Nucl. Fusion **38** (1998) 1275.

[29] Romanelli, F., et al., ITER "Energetic Particle Physics", ITER Physics Basis Document, Nucl. Fusion **39** 12 (1999).

[30] Zweben, S.J., et al., Plasma Phys. Control. Fusion **39** (1997) A275.

[31] Von Goeler, S., et al., Rev. Sci. Instrum. **68** (1997) 548.

[32] Krasilnikov, A.V., et al., Rev. Sci. Instrum. **70** (1999) 1107.

[33] Sasao, M., Wurden, G.A., Mansfield, D.K., Fusion Eng. Des. **34 & 35** (1197) 333.

[34] Machuzak, J.S. et al., Rev. Sci. Instrum. **68** (1997) 458.

[35] Cecil, F.E., et al., Nucl. Instrum. Methods Phys. Res. A **271** (1988) 547.

[36] Cecil, F.E., et al., Rev. Sci. Instrum. **68** (1997) 361.

[37] Fisher, R.K., et al., Rev. Sci. Instrum. **68** (1997) 1103.

[38] Ikeda, Y., et al., Nucl. Fusion **36** (1996) 759.

[39] Gerdin, G., et al., Fusion Technol. **7** (1985) 180.

[40] Young, K.M., et al., Plasma Phys. Control. Fusion **34** (1992) 2001.

[41] Stratton, B.C., et al., Nucl. Fusion **39** (1999) 1309.

[42] Proc. 4th IAEA Tech. Comm. Mtg on Alpha Particles in Fusion Research 1995, Nucl. Fusion **35** 12 (1995).

[43] Proc. 5th IAEA Tech. Comm. Mtg on Alpha Particles in Fusion Research 1997, Nucl. Fusion **38** 9 (1998).

[44] Strachan, J.D., et al., Plasma Phys. Control. Fusion **39** (1997) B103.

[45] Hawryluk, R.J., Rev. Mod. Phys. **70** (1998) 537.
[46] Bell, M.G., et al., Phys. Plasmas **4** (1997) 1714.
[47] Meade, D., Fusion Eng. Des. **27** (1995) 17.
[48] Hosea, J., et al., Fusion Technol. **26** (1994) 389.
[49] Strachan, J.D., et al., Nucl. Fusion **29** (1989) 163.
[50] Murphy, T.J., Strachan, J.D., Nucl. Fusion **25** (1985) 383.
[51] Miley, G.H., Kislev, H., Phys. Scri. T **16** (1987) 155.
[52] Elevant, T., A Preliminary Study of Charged Fusion Product Diagnostics for JET, Rep. TRITA-PFU-84-04, Royal Institute of Technology, Stockholm (1984).
[53] Seiler, S., Hendel, H., Bull. Am. Phys. Soc. **23** (1978) 701.
[54] Zweben, S.J., et al., Rev. Sci. Instrum. **63** (1992) 4565.
[55] Darrow, D.S., Rev. Sci. Instrum. **66** (1995) 476.
[56] Tuszewski, M., Zweben, S.J., Rev. Sci. Instrum. **64** (1993) 2459.
[57] Felt, J., et al., Rev. Sci. Instrum. **62** (1990) 3262.
[58] Zweben, S.J., et al., Phys. Plasmas **1** (1994) 1469.
[59] Herrmann, H.W., Anomalous Loss of DT Alpha Particles in TFTR, Rep. PPPL-3214, Princeton Plasma Physics Lab., NJ (1996).
[60] Boivin, R., Zweben, S.J., White, R.B., Nucl. Fusion **33** (1993) 449.
[61] Boivin, R., Zweben, S.J., Phys. Fluids B **5** (1993) 1559.
[62] Zweben, S.J., et al., Nucl. Fusion **35** (1995) 1445.
[63] Zweben, S.J., et al., Nucl. Fusion **38** (1998) 739.
[64] Yavorski, V., et al., Nucl. Fusion **38** (1998) 1565.
[65] Yavorski, V., et al., IAEA-CN-69/THP2/27, paper presented at IAEA Conf. on Fusion Energy, Yokohama, 1998.
[66] Zweben, S.J., et al., in Controlled Fusion and Plasma Physics (Proc. 21st Eur. Conf. Montpellier, 1994), Vol. 18B, Part 1, European Physical Society, Geneva (1994) 290.
[67] Zweben, S.J., et al., Nucl. Fusion **39** (1999) 1097.
[68] Mirnov, S., et al., Phys. Plasmas **5** (1998) 3950.
[69] Bush, C.E. et al., Phys. Plasmas **2** (1995) 2366.
[70] Mynick, H.E., Phys. Fluids B **5** (1993) 2460.
[71] Chang, Z., et al., Phys. Plasmas **4** (1997) 1610.
[72] Kolesnichenko, Ya., et al., Phys. Plasmas **6** (1999) 1117.
[73] Langley, R.A., et al., Bull. Am. Phys. Soc. **29** (1984) 1309.
[74] Herrmann, H.W., et al., Rev. Sci. Instrum. **66** (1995) 352.
[75] Herrmann, H.W., et al., Nucl. Fusion **37** (1996) 293.
[76] Basiuk, V., et al., Nucl. Fusion **35** (1995) 1593.
[77] Bastasz, R., Buchenauer, D., Zweben, S.J., Rev. Sci. Instrum. **61** (1990) 3199.
[78] Fisher, R.K., et al., Rev. Sci. Instrum. **63** (1992) 4499.
[79] Petrov, M.P., et al., Phys. Plasmas **6** (1999) 2430.
[80] Medley, S.S., et al., in Controlled Fusion and Plasma Physics (Proc. 20th Eur. Conf. Lisbon, 1993), Vol. 17C, Part III, European Physical Society, Geneva (1993) 1183.
[81] Duong, H.H., et al., Rev. Sci. Instrum. **68** (1997) 340.
[82] Medley, S.S., et al., Rev. Sci. Instrum. **67** (1996) 3122.
[83] McChesney, J.M. et al., Phys. Plasmas **4** (1997) 381.
[84] Fisher, R. K., et al., Phys. Rev. Lett. **75** (1995) 846.
[85] Janev, R.K. , Elementary Processes in Hydrogen–Helium Plasmas, Springer-Verlag, Berlin (1987).
[86] Kislyakov, A.I., et al., Fusion Eng. Des. **34 & 35** (1997) 107.
[87] Gorelenkov, N.N., et al., Nucl. Fusion **37** (1997) 1053.
[88] Duong, H.H., et al., Nucl. Fusion **37** (1997) 271.
[89] Medley, S.S., et al., Plasma Phys. Control. Fusion **38** (1996) 1779.
[90] Medley, S.S., et al., Nucl. Fusion **38** (1998) 1283.
[91] Petrov, M.P., et al., Nucl. Fusion **35** (1995) 1437.
[92] Kolesnichenko, Ya.I., et al., Nucl. Fusion **32** (1992) 449.
[93] Kolesnichenko, Ya.I., et al., Phys. Plasmas **5** (1998) 2963.
[94] Fisher, R.K., et al., Rev. Sci. Instrum. **68** (1997) 336.
[95] Stratton, B.C., et al., Nucl. Fusion **34** (1994) 734.
[96] McKee, G., et al., Rev. Sci. Instrum. **66** (1995) 643.
[97] McKee, G., et al., Nucl. Fusion **37** (1997) 501.
[98] McKee, G., et al., Phys. Rev. Lett. **75** (1995) 649.
[99] Strachan, J.D., et al., Phys. Rev. Lett. **72** (1994) 3526.
[100] Janev, R.K., Boley, C.D., Post, D.E., Nucl. Fusion **29** (1989) 2125.
[101] von Hellermann, M.G., et al., Plasma Phys. Control. Fusion **33** (1991) 1805.
[102] Stratton, B.C., et al., Nucl. Fusion **36** (1996) 1586.
[103] Kolesnichenko, Ya.I., et al., Phys. Rev. Lett. **68** (1992) 3881.
[104] Kadomtsev, B.B., Sov. J. Plasma Phys. **1** (1976) 389.
[105] Wesson, J.A., Plasma Phys. Control. Fusion **28** (1986) 243.
[106] Levinton, F.M., et al., Phys. Fluids B **5** (1993) 2554.
[107] Stratton, B.C., et al., Rev. Sci. Instrum. **68** (1997) 269.
[108] Ramsey, A.T., et al., Rev. Sci. Instrum. **66** (1995) 871.
[109] Taylor, G., et al., Phys. Rev. Lett. **76** (1996) 2722.
[110] Synakowski, E.J., et al., Phys. Rev. Lett. **75** (1995) 3689.

[111] Scott, S.D., et al., Phys. Scr. **51** (1995) 394.

[112] Hawryluk, R.J., et al., Phys. Rev. Lett. **72** (1994) 3530.

[113] Scott, S.D., et al., Phys. Plasmas **2** (1995) 2299.

[114] Budny, R.V., Nucl. Fusion **34** (1994) 1247.

[115] Strachan, J.D., et al., Nucl. Fusion **3** (1993) 991.

[116] Stauffer, F.J., et al., Rev. Sci. Instrum. **56** (1985) 925.

[117] Cavallo, A., et al., Rev. Sci. Instrum. **59** (1988) 889.

[118] Johnson, L.C., et al., Rev. Sci. Instrum. **63** (1992) 4517.

[119] Taylor, G., et al., Plasma Phys. Control. Fusion **34** (1994) 523.

[120] Thomas, P.R., et al., Phys. Rev. Lett. **80** (1998) 5548.

[121] Stratton, B.C., et al., in Time Resolved Two- and Three-Dimensional Plasma Diagnostics (Proc. IAEA Tech. Comm. Mtg Nagoya, 1991), IAEA, Vienna (1991) 78.

[122] Synakowski, E.J., et al., Phys. Fluids B **5** (1993) 2215.

[123] Reiter, D., et al., Nucl. Fusion **30** (1990) 2141.

[124] Strachan, J.D., et al., in Plasma Physics and Controlled Nuclear Fusion Research 1988 (Proc. 12th Int. Conf. Nice, 1988), Vol. 1, IAEA, Vienna (1989) 257.

[125] Cheng, C.Z., Chance, M.S., Phys. Fluids **29** (1986) 3695.

[126] Cheng, C.Z., et al., in Plasma Physics and Controlled Nuclear Fusion Research 1992 (Proc. 14th Int. Conf. Würzburg, 1992), Vol. 2, IAEA, Vienna (1993) 51.

[127] Cheng, C.Z., Fu, G.Y., Van Dam, J.W., in Theory of Fusion Plasmas (Proc. Joint Varenna–Lausanne Workshop Lausanne, 1988), CEC, Brussels (1988) 259.

[128] Budny, R.V., et al., Nucl. Fusion **32** 429 (1992).

[129] Zweben, S.J., et al., Nucl. Fusion **36** (1997) 987.

[130] Wong, K.L., et al., Phys. Rev. Lett. **76** (1996) 2286.

[131] Heidbrink, W.W., et al., Nucl. Fusion **36** (1996) 1725.

[132] Batha, S.H., et al., Nucl. Fusion **35** (1995) 1463.

[133] Mett , R., Mahajan, S., Phys. Fluids B **4** (1992) 2885.

[134] Fu, G.Y., et al., Phys. Rev. Lett. **75** (1995) 2336.

[135] Fu, G.Y., Nazikian, R., Budny, R.V., Chang, Z., Phys. Plasmas **5** (1998) 4284.

[136] Spong, D., et al., Nucl. Fusion **35** (1995) 1687.

[137] Spong, D.A., et al., "Alpha-driven Alfvén instabilities and velocity shear effect", paper presented at 5th IAEA Tech. Comm. Mtg on Alpha Particles, Abingdon, 1997.

[138] Nazikian, R., et al., Phys. Rev. Lett. **78** (1997) 2976.

[139] Nazikian, R., et al., Phys. Plasmas **5** (1998) 1703.

[140] Levinton, F.M., et al., Phys. Rev. Lett. **63** (1989) 2060.

[141] Mazzucato, E., et al., Phys. Rev. Lett. **77** (1996) 3145.

[142] Nazikian, R., Mazzucato, E., Rev. Sci. Instrum. **66** (1995) 392.

[143] Sigmar, D.J., Hsu, C.T., White, R.B., Cheng, C.Z., Phys. Fluids B **4** (1992) 1506.

[144] Breizman, B.N., et al., Phys. Plasmas **4** (1997) 1559.

[145] Wu, Y., White, R.B., Chen, Y., Rosenbluth, M.N., Phys. Plasmas **2** (1995) 4555.

[146] Zweben, S.J. et al., Nucl. Fusion **32** (1992) 1823.

[147] Lam, N.T., et al., Nucl. Fusion **34** (1994) 1161.

[148] Darrow, D.S., et al., Nucl. Fusion **36** (1996) 1.

[149] Chang, C.S., Cohen, S., Majeski, D., Redi, M., Zweben, S., Comments Plasma Phys. Control. Fusion **18** (1997) 235.

[150] Cottrell, G.A., et al., Nucl. Fusion **33** (1993) 1365.

[151] Cauffmann, S., Majeski, R., McClements, K.G., Dendy, R.O., Nucl. Fusion **35** (1995) 1597.

[152] Kimura, H., et al., Nucl. Fusion **38** (1998) 1303.

[153] Fisch, N.J., Rax, J.-M., Phys. Rev. Lett. **69** (1992) 612.

[154] Fisch, N.J., et al., Phys. Plasmas **2** (1995) 2375.

[155] Chang, C.S., et al., Phys. Fluids B **3** (1991) 3429.

[156] Chen, L., et al., Nucl. Fusion **28** (1988) 389.

[157] Yamagiwa, M., Phys. Plasmas **1** (1994) 205.

[158] Kusama, Y., et al., J. Nucl. Mater. **220–222** (1995) 438.

[159] Ikeda, Y., et al., Nucl. Fusion **36** (1996) 759.

[160] Doloc, C., Martin, G., in Controlled Fusion and Plasma Physics (Proc. 20th Eur. Conf. Lisbon, 1993), Vol. 17C, Part III, European Physical Society, Geneva (1994) 893.

[161] Finken, K.H., et al., Phys. Rev. Lett. **73** (1994) 436.

[162] McClements, K.G., et al., Phys. Plasmas **3** (1996) 543.

[163] Dendy, R.O., et al., Phys Plasmas **1** (1994) 1918.

[164] Gorelenkov, N.N., Cheng, C.Z., Phys. Plasmas **2** (1995).

[165] Gorelenkov, N.N., Cheng, C.Z., Nucl. Fusion **35** (1995) 1743.

[166] Arunasalam, V., J. Plasma Phys. **57** (1997) 523.

[167] Coppi, B., Phys. Lett. **172A** (1993) 439.

[168] Fisch, N.J., Herrmann, M.C., Plasma Phys. Control. Nucl. Fusion **41** (1999) A221.

[169] Darrow, D.S., et al., Nucl. Fusion **37** (1997) 939.

[170] White, R.B., et al., Phys. Plasmas **2** (1995) 2871.

[171] Herrmann, M.C., PhD Thesis, Princeton Univ., NJ (1998).

[172] Majeski, R., et al., Phys. Rev. Lett. **76** (1996) 764.

[173] Darrow, D.S., et al., Nucl. Fusion **35** (1996) 509.

[174] Barnes, C.W., et al., Nucl. Fusion **38** (1998) 597.

[175] Zhao, Y., White, R.B., Phys. Plasmas **4** (1997) 1103.

[176] Chang, Z., et al., Phys. Rev. Lett. **76** (1996) 1071.

[177] Spong, D., et al., Fusion Technol. **18** (1990) 496.

[178] Rewoldt, G., Nucl. Fusion **31** (1991) 2333.

[179] Korotkov, A.A., Gondhalekar, A., Stuart, A.J., Nucl. Fusion **37** (1997) 35.

[180] Binoslev, H., et al., Phys. Rev. Lett. **83** (1999) 3206.

[181] O'Brien, M.R., Cox, M., Gardner, C.A., Zajtsev, F.S., Nucl. Fusion **35** (1995) 1537.

[182] Park, W., et al., in Fusion Energy 1996 (Proc. 16th Int. Conf. Montreal, 1996), Vol. 2, IAEA, Vienna (1997) 411.

[183] Spong, D., et al., Phys. Plasmas **1** (1994) 1503.

[184] Breizman, B.N., et al., Phys. Plasmas **4** (1997) 1559.

[185] Candy, J., et al., Phys. Plasmas **4** (1997) 2597.

[186] Berk, H.L., et al., Phys. Rev. Lett. **76** (1996) 1256.

[187] Chen, Y., White, R.B., Phys. Plasmas **4** (1997) 3591.

[188] Wong, K.L., et al., Phys. Plasmas **4** (1997) 393.

[189] Heidbrink, W.W., Danielson, J.R., Jr., Phys. Plasmas **1** (1994) 4120.

[190] Bernabei, S., et al., IAEA-CN-69/EXP3/8, paper presented at the IAEA Conf. on Fusion Energy, Yokohama, 1998.

[191] Sharapov, S.E., et al., Nucl. Fusion **39** (1999) 373.